UNIVERSITY OF OSLO
Department of Physics

Sensitivity Analysis of a Two Component Seismic Streamer

Master Thesis
in Electronic

Mohammad Reza
Ghasemi

February 2014

Acknowledgement

I would like to express my deepest gratitude and appreciation to my excellent supervisors, Bent Kjellesvig and Kemal Ozdemir at WesternGeco (Schlumberger), and Andreas Austeng at the Department for Informatics (Ifi), University of Oslo. Without their invaluable contribution this thesis would not have been possible. They have helped me at all stages and in all ways throughout the thesis. Bent and Kemal have always been up for discussions, input and ideas.

A special gratitude I give to Andreas, whose guidance and inspiration has led me into the field of signal processing. He has always been there for me since the beginning of my study. Without his great effort which I will be grateful forever, I would not have been able to work on this interesting topic.

Furthermore I would also like to acknowledge my sincere thanks to WesternGeco for letting me join them for a year. They provided me with an office, the synthetic seismic data which this thesis is based on, and everything else I could have needed throughout the year.

Finally, thanks to my family and friends for all their support and patience during my studies.

Mohammad Reza Ghasemi
Oslo, 12th February 2014

Abstract

Conventional marine seismic streamers use hydrophone sensors to measure the seismic wave field. One well known problem in marine seismic is that up-going waves are reflected with inverted polarity at the sea surface because of the air-water interface. The interference between the up-going and down-going wave fields create nulls or notches in the recorded spectrum.

A two-component streamer includes particle motion sensors in addition to hydrophones to measure the particle velocity of the seismic wave field. By combining the data acquired by pressure and particle motion sensors, the up-going wave field can be computed from the measured total wave field.

In seismic acquisition system, data quality is negatively affected by source, receiver, ambient noise, and other system perturbations. Different types of sensors may be subjected to different types of noise, perturbations and have different transfer function. In this thesis, we have analyzed the impact of several types of perturbations on synthetic marine seismic data. We present the impact of individual perturbations using a sensitivity chart. We demonstrate the relative significance of these perturbations and the need to focus on reducing them. According to our analysis, the most significant errors were due to polarity reversals and sensor sensitivity.

Table of Contents

1 Introduction

Conventional marine seismic acquisition use hydrophone sensors to measure the pressure wave field. Two-component streamer technology includes particle motion sensors in addition to hydrophones to measure the particle velocity wave field of the seismic wave field. By combining these to wave fields, the up-going wave field can be computed from the total wave field. During acquisition, seismic data quality is negatively affected by source, receiver, ambient noise, and other perturbations.

In this thesis, we will analyze the effect of various types of sensor errors and perturbations on the pressure, particle velocity and up-going wave fields. Our approach is to introduce the perturbations and noise associated with the two-component marine seismic acquisition system and receivers (geophones and hydrophones) on synthetic seismic data; simulate a typical acquisition processing flow that includes analog group forming and P-Z combination, and then analyze and quantify the impact of these perturbations on the acquired data.

The following perturbations and errors are chosen to be analyzed:

- **Geophone transfer function**
  There is always variation in the production of the sensors. Therefor the sensors will have different response which results in variation on the acquired data.
- **Self noise**
  Velocity geophone sensor self-noise is limited to two types of noise; the noise due to Brownian motion of the suspended sensor mass, and the thermal noise in electronics and cables.
- **Position error**
  Sensor position error is caused by the assembly technician's inaccuracy when mounting the sensors along the streamer. Sensor position error can have high negative impact on the acquired data quality.
- **Dead channels**
  Sensors with poor or zero response can introduce high amplitude error on the recorded seismic data. Sensors used in marine seismic acquisition are very exposed due to their operation environment, streamer tension etc. Hence it is very important to analyze the impact of dead sensors on the seismic data quality.
- **Polarity reversals**
  Polarity reversals refer to reversed mounting of sensors along the streamer which can result in very high amplitude perturbation.
- **Sensor sensitivity**
  Sensor sensitivity varies from sensor to sensor due to variation in production. We study the impact of sensor sensitivity variation in marine seismic acquisition.
- **Vector fidelity**
  Sensor tilt/inclination can affect the reflection data negatively. Hydrophones are not sensitive to small tilt while geophones are very sensitive to tilt. We will study the impact of tilt on the particle velocity data recorded by geophone sensors.

1.1 Thesis outline

Chapter 2 gives an introduction to seismic acquisition and related terminology with focus on marine exploration.

Chapter 3 describes the receiver ghost problem, and discusses various techniques to mitigate receiver ghost including the two-component streamer technology. It also introduces data processing algorithms used with two-component streamers to remove the receiver ghost.

Chapter 4 describes the synthetic data generated by simulation of the acquisition with two-component streamers, preprocessing and deghosting.

Chapter 5 describes the concept of analog and digital group forming and their advantages in signal-to-noise ratio enhancement.

Chapter 6 introduces different types of perturbations and noise associated with two-component marine seismic acquisition and studies their impact on the synthetic seismic data.

Chapter 7 presents the results and conclusions from the analysis. It also suggests topics for future work.

2 Introduction to marine seismic

In this chapter we are going to get familiar with some basic principles involved in seismic surveys. Our focus is toward exploration and exploitation of hydrocarbon resources.

2.1 Seismic Reflection

Seismic reflection is a method used to explore the underground structure. This method gives high resolution structural images of the subsurface of the earth.

In seismic surveying, energy waves are generated and directed into the earth. Different layers of rock below the earth surface reflect some of the energy back to the surface. The returning waves are then recorded with sensitive measuring sensors. These recordings are then being adjusted and processed by computers and transformed into visual images that give a picture of what the structure and nature of the subsurface of the earth is like beneath the seismic survey area. This is mostly used in the search for hydrocarbon resources, gas and oil (© IAGC, March 2002).

Focusing on the oil and gas exploration, it can be generally divided into two main categories:

- Onshore or Land Exploration
- Offshore or Marine Exploration.

There are several types of sensors used to gather data beneath the surface of the earth.

Hydrophone sensors: These types of sensors are mostly used in marine seismic exploration. They are sensitive to changes in the water pressure. They have a piezoelectric element that converts changes in the water pressure into an electrical signal and record the pressure amplitude.

Geophone sensors: These types of sensors are mostly used in land seismic exploration. They are sensitive to local particle displacements and record displacement amplitude as the wave propagates through the medium.

This thesis will focus on marine seismic exploration.

2.2 Marine seismic acquisition

In a typical marine seismic acquisition system, several receiver arrays referred to as "streamers" deployed and towed behind a giant seismic vessel, together with a source array (Figure 1). A Source array (one or multiple air gun arrays) generates a pulse by releasing highly pressurized air into the water. Hydrophone sensors are used as receivers to measure the seismic wave field.

Employing shallow source and shallow streamers will increase the high-frequency content of the seismic data. However, it will attenuate the low frequencies. On the contrary, deep sources and deep streamers employment enhance the low frequencies, but attenuate the high-frequency content of the data. Furthermore, recording seismic data with a deep streamer results in higher signal-to-noise ratio (S/N) compared to shallow streamer. Hence, in a conventional marine survey design these clashing aspects should be balanced to arrive at a depth for the sources and streamers that enhance the bandwidth and signal-to-noise ratio of the data for a particular target of interest (Kragh and Muyzert, 2010).

Special depth controllers known as birds are attached to the streamers to control the streamer depth and hold it at the desired depth.

In a 2-D marine seismic acquisition only a single streamer consisting of several sensors is being used, while in a 3-D acquisition system multiple streamers are deployed for gathering data.

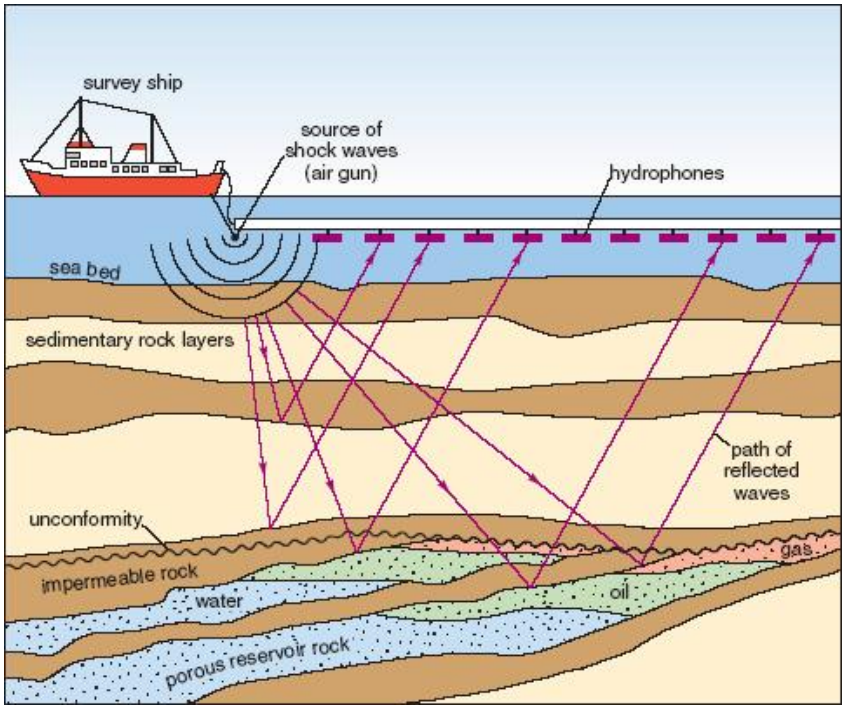

Figure 1: Illustration of towed-streamer marine acquisition.

Picture from (http://openlearn.open.ac.uk/mod/resource/view.php?id=172129).

2.3 Summary of main terminology in seismic

In this section we explain terminology related to seismic briefly and later at other chapters describe those of them related more in detail when it is applicable.

- **Multiples:** Internal reflections of seismic energy at more than one interface before being recorded by the receiver are called multiples. Figure 2 illustrate the multiple events in marine seismic acquisition.

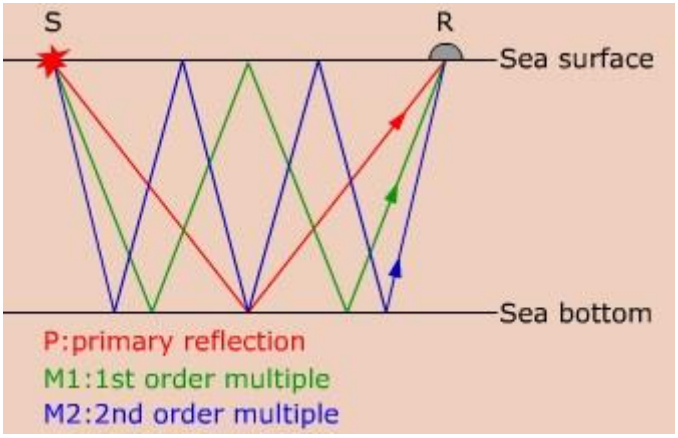

Figure 2: Illustration of multiples in marine seismic acquisition

Picture from (www.unigeo.no; GEOCLASS-Chapter 4, Removal of multiples).

- **Ghost:** is a special case of multiple reflections; reverberation of the seismic energy in the shallow subsurface arriving short time after the primary reflection that results in the double appearance of each event in the gathered data.
  The figure below shows the source and receiver ghosts. The solid white lines illustrate the Ghost-less travel path; the yellow dotted and dashed lines show the travel path of the source and receiver ghost respectively.

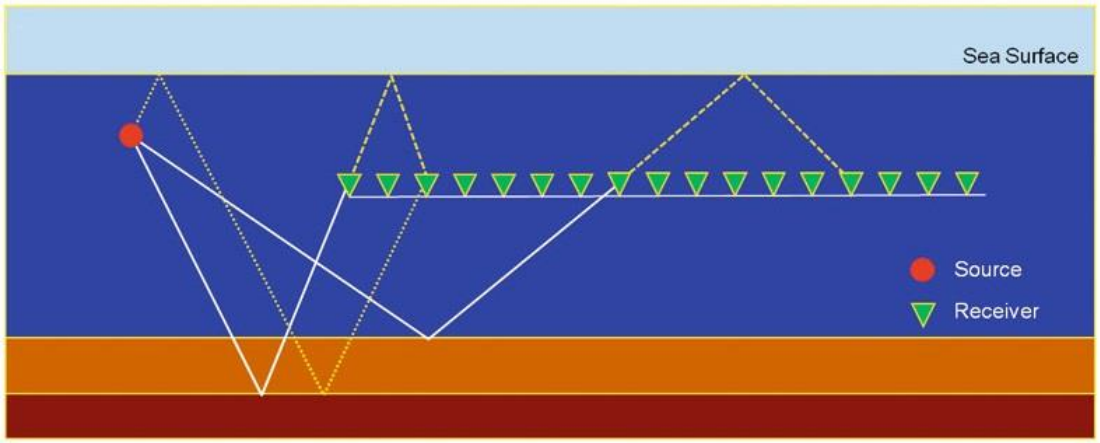

Figure 3: Illustration of source and receiver ghosts.

Picture from (Baldock et al., 2013).

- **Direct Arrivals:** refers to those seismic waves traveling directly from the source toward the receiver.

- **TX Plot:** refers to a time-space plot where the data recorded by all receivers are plotted as an image. In TX plots the horizontal axis denotes the receiver position along the streamer, and the vertical axis denotes the time. The amplitude of the wave field is colour encoded.

- **FK Spectra:** The 2D frequency-wavenumber representation of the wave field, also known as the FK representation in petroleum seismology is the 2D Fourier transformation of signals with one temporal and one spatial variable. The 2D Fourier transform is generally described in (Ikelle and Amundsen, 2005 Chapter 4 & 8).

  FK representation of signal focuses frequency, apparent velocity, and wavenumber. This process expresses that reconstruction of a time-space signal can be performed by adding individual plane waves in the form of a series.

  The 2D Fourier transform of 2D continuous signals can be generated as follow:

$$U(\omega, k) = \iint_{-\infty}^{+\infty} dtdx\, u(t, x) \times e^{[i(\omega t - kx]} \quad ,$$

  where $U(\omega, k)$ is the 2D Fourier representation of the time-space signal $u(t, x)$, and kx is the wavenumber.

- **Deghosting:** refers to separation of the up-going and down-going wave field from the "total pressure" wave field so that it contains no receiver ghosts.

- **Two-Component streamer:** refers to a type of streamer that includes particle motion sensors (geophone) in addition to pressure sensors (hydrophone).

3 Receiver Ghost and its Removal

In this chapter we introduce the receiver ghost problem; and the two-component streamer technology that allows removal of the receiver ghost. We also review the data processing algorithms that are used with two-component streamers to remove the receiver ghost.

3.1 Receiver Ghost

One of the well-known problems in towed-marine acquisition is the "receiver ghost" which is defined as an event whose last reflection was from the sea surface (Ikelle and Amundsen, 2005). The up-going pressure wave field reflected at the air-water interface will create a down-going pressure wave field with inverted polarity. The destructive interference of the down-going pressure wave field with the up-going pressure wave field creates notches in the spectrum of the recorded total pressure wave field. As a result of the spectral notches, the receiver ghost reduces the useful bandwidth and complicates the signature of the seismic wavelet.

Mathematically, any up-going pressure wave field can be described as the superposition of the plane waves which propagate in arbitrary directions in in-line and cross-line axes; and in $-z$ direction in vertical axis:

$$P_U(t,\mathbf{x}) = \int A_U(f,k_x,k_y) e^{j2\pi\left(k_x x + k_y y - k_z z - ft\right)} \mathrm{d}f \, \mathrm{d}k_x \, \mathrm{d}k_y \ , \tag{1}$$

where t represents time; $\mathbf{x} = (x,y,z)$ represents spatial coordinates; $\mathbf{k} = (k_x,k_y,-k_z)$ represent the vector of wavenumbers; and $A_U(f,k_x,k_y)$ represent the complex-valued amplitude. We note that the amplitude $A_U(f,k_x,k_y)$ is a function of only frequency, inline wavenumber and cross-line wavenumber; as the vertical wavenumber is given by

$$k_z = \sqrt{f^2/c^2 - k_x^2 - k_y^2} \ , \tag{2}$$

where c is the phase-velocity of sound in water which is roughly $1500\mathrm{m/s}$. The reflection of this up-going pressure wave field at the air-water interface creates a down-going wave field with opposite polarity and opposite propagation direction in z-axis:

$$P_D(t,\mathbf{x}) = \varepsilon \int A_U(f,k_x,k_y) e^{j2\pi\left(k_x x + k_y y + k_z z - ft\right)} \mathrm{d}f \, \mathrm{d}k_x \, \mathrm{d}k_y \ . \tag{3}$$

When the wavelength of the wave field is large compared to the surface disturbances (wave action), the surface reflectivity can be assumed to be $\varepsilon \cong -1$. In the rest of this thesis we will assume $\varepsilon = -1$. However, it should be noted that for the case of high resolution data this assumption is only valid in very calm sea conditions.

The hydrophone receivers in a towed-streamer will measure the total pressure wave field as the summation of the up-going and down-going wave fields:

$$P_T(t,\mathbf{x}) = P_U(t,\mathbf{x}) + P_D(t,\mathbf{x}) \ . \tag{4}$$

Substituting the expression for up and down-going wave fields into Eq. (4), the expression for the total pressure wave field can be obtained in terms of the up-going wave field:

$$P_T(t,\mathbf{x}) = \int \left(1 - e^{j4\pi k_z z}\right) A_U(f,k_x,k_y) e^{j2\pi\left(k_x x + k_y y - |k_z| z - ft\right)} \mathrm{d}f \, \mathrm{d}k_x \, \mathrm{d}k_y \,, \tag{5}$$

The FFK (frequency - in-line wavenumber – cross-line wavenumber) transform of the total pressure wave field shows the effect of the receiver ghost in spectral domain:

$$\begin{aligned} P_T(f,k_x,k_y;z) &= \int P_T(t,\mathbf{x}) e^{j2\pi(ft - k_x x - k_y y)} \mathrm{d}t \, \mathrm{d}x \, \mathrm{d}y \\ &= G_P(f,k_x,k_y;z) P_U(f,k_x,k_y;z) \end{aligned} \,, \tag{6}$$

where $G_P(f,k_x,k_y;z)$ the pressure ghost operator defined as:

$$G_P(f,k_x,k_y;z) = 1 - e^{j4\pi k_z z} \,. \tag{7}$$

The ghost operator affects both the amplitude and phase spectrum of the received wave field. The phase and the amplitude effect of the ghost operators are given by:

$$\mathrm{Arg}\left[G_P(f,k_x,k_y;z)\right] = -\tan^{-1}\left[\frac{\sin 4\pi k_z z}{1 - \cos 4\pi k_z z}\right] \tag{8}$$

$$\left|G_P(f,k_x,k_y;z)\right| = 2\left|\cos(2\pi f z / c)\right| \,. \tag{9}$$

The magnitude of the ghost filter varies between 0 (destructive interference between the up-going wave field and ghost) and 2 (constructive interference). We can calculate the frequencies where notches occur from the fact that a distance of one wavelength corresponds to the ghost delay (POSTHUMUS, 1993).

3.2 Techniques to Mitigate Receiver Ghost

3.2.1 Single-sensor deghosting

The single-sensor deghosting method uses only pressure sensors to estimate the up-going wave field without boosting noise. This method is dependent on a ghost model in order to estimate the up-going wave field.

$$P_T = G_P * UP + N_P \,, \tag{10}$$

where P_T is the total pressure wave field; G_P is the pressure ghost operator and N_P is the pressure noise. Since G_P is zero for some frequencies and wavenumbers, the inversion of the above equation should be stabilized around ghost notches.

This method has been described in detail in Exploration Seismology (Sheriff and Geldart, 1995).

3.2.2 Over/under acquisition

The Over/Under acquisition method combines the advantages of shallow and deep cable depth to provide the ghost-free, broadband data at all frequencies, known as the up-going wave field. This method uses at least two streamers towed at two different cable depths, with typically 5-10 m separation. The recorded data from the two streamers are combined with a deghosting algorithm to generate the ghost-free up-going wave field. This method has been illustrated in detail in (Özdemir, Caprioli, Özbek, Kragh, and ROBERTSSON, 2008).

3.2.3 Two-component streamer

In this thesis, we will consider only two-component streamers. A two-component streamer uses both the pressure and particle velocity sensors to measure the seismic wave fields reflected from the earth. The particle velocity sensor measures the vertical component of the particle velocity, $V_T(t,\mathbf{x})$ which is related to the gradient of the pressure:

$$\frac{\partial V_T(t,\mathbf{x})}{\partial t} = -\frac{1}{\rho}\frac{\partial P_T(t,\mathbf{x})}{\partial z}\ , \tag{11}$$

where ρ is the density of water. To simplify the later equations, we will assume that the particle velocity measurement is scaled by the acoustic impedance of the water given by ρc:

$$Z(t,\mathbf{x}) = \rho c V_T(t,\mathbf{x})\,. \tag{12}$$

It can be shown from (OZDEMIR et al., 2011) that, the frequency – wavenumber domain relationship between the particle velocity and pressure measurements is as follows:

$$\begin{aligned} Z_T(f,k_x,k_y;z) &= \frac{c|k_z|}{f}\frac{1+e^{j4\pi k_z z}}{1-e^{j4\pi k_z z}}P_T(f,k_x,k_y;z) \\ &= \frac{c|k_z|}{f}G_Z(f,k_x,k_y;z)P_U(f,k_x,k_y;z) \end{aligned}\ , \tag{13}$$

where ρc is the acoustic impedance of water; the dimensionless ratio $c|k_z|/f$ is the obliquity factor; Z represents the cable depth and $G_Z(f,k_x,k_y;z)$ is the dual of the ghost operator for particle velocity measurement:

$$G_Z(f,k_x,k_y;z) = 1+e^{j4\pi k_z z}\,. \tag{14}$$

At vertical incidence, i.e., when $k_z = f/c$, the magnitudes of the ghost operators become:

$$\begin{aligned} \left|G_P(f,k_x,k_y;z)\right| &= 1-e^{j4\pi fz/c} = 2\left|\sin(2\pi fz/c)\right| \\ \left|G_Z(f,k_x,k_y;z)\right| &= 1+e^{j4\pi fz/c} = 2\left|\cos(2\pi fz/c)\right| \end{aligned}\ . \tag{15}$$

The ghost notches in spectra can be derived as a function of frequency from Eq. (15). The presence of ghost notches corresponds to zeroes in the spectra:

$$G_P = 1 - e^{j4\pi K_z z} = 0$$

$$e^{j4\pi K_z z} = 1 = e^{j2\pi n}, \qquad for\ n = 1,2,3..$$

$$j4\pi K_z z = j2\pi n$$

We can substitute the vertical wavenumber K_z with the formula given in Eq. (2) assuming that $k_y = 0$:

$$\sqrt{\frac{f^2}{c^2} - {K_x}^2 z} = n, \qquad for\ n = 1,2,3..$$

The frequencies where the ghost notches may occur for pressure measurement are given by:

$$f = \sqrt{\frac{n^2 c^2}{4z^2} + {K_x}^2 c^2} = \frac{nc}{2z}\sqrt{1 + \frac{4z^2 {K_x}^2}{n^2}}, \qquad for\ n = 1,2,3.. \tag{16}$$

We note that the ghost notches for the particle velocity measurement can be derived by the same procedure. The frequencies where the ghost notches for velocity measurements may occur are given by:

$$f = \sqrt{\frac{n^2 c^2}{4z^2} + \frac{c^2}{16z^2} + {K_x}^2 c^2} = \frac{(n+0.5)c}{2z}\sqrt{1 + \frac{4z^2 {K_x}^2}{(n+0.5)^2}}, \qquad for\ n = 1,2,3.. \tag{17}$$

Figure 4 and Figure 5 show the magnitude of the $k_y = 0$ slice of the ghost responses at a streamer depth of 20 meter below the sea surface with 2D FK plots. The ghost notches are shown with black dashed lines. These lines have been derived by Eq. (16) and (17).

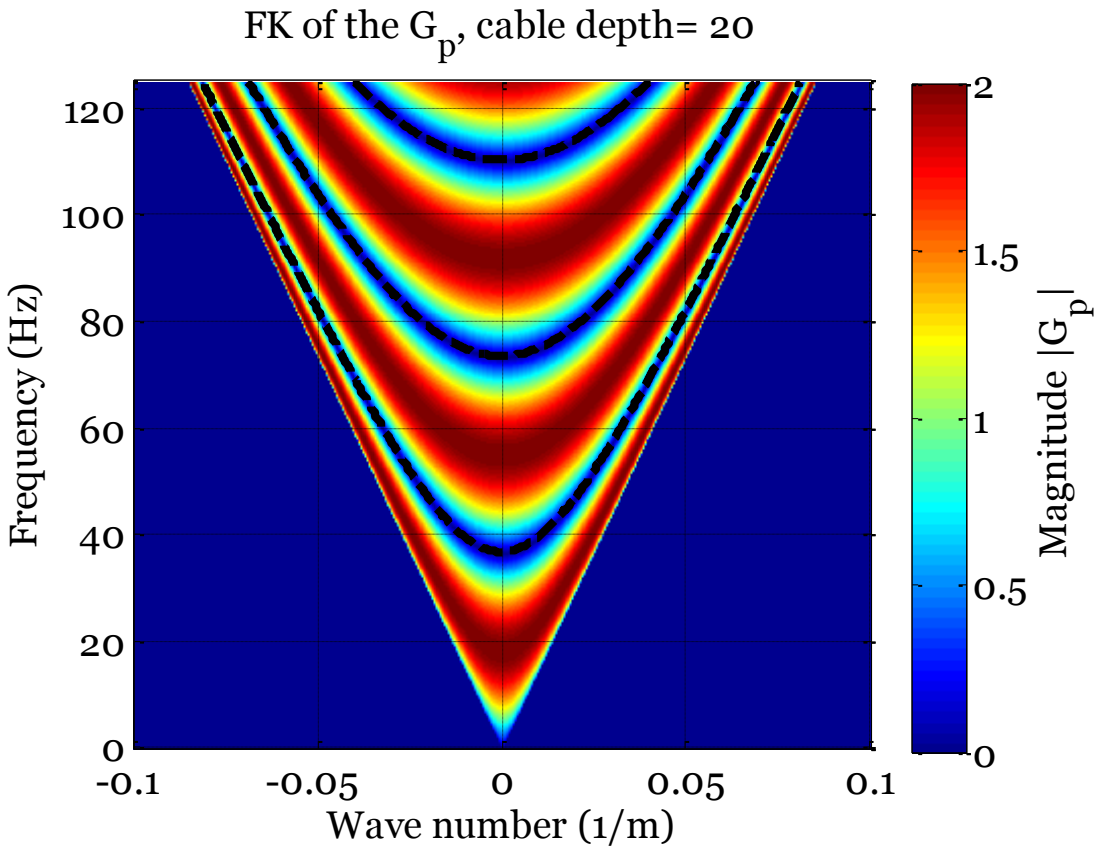

Figure 4: The Frequency-Wavenumber plot of the ghost operator Gp.

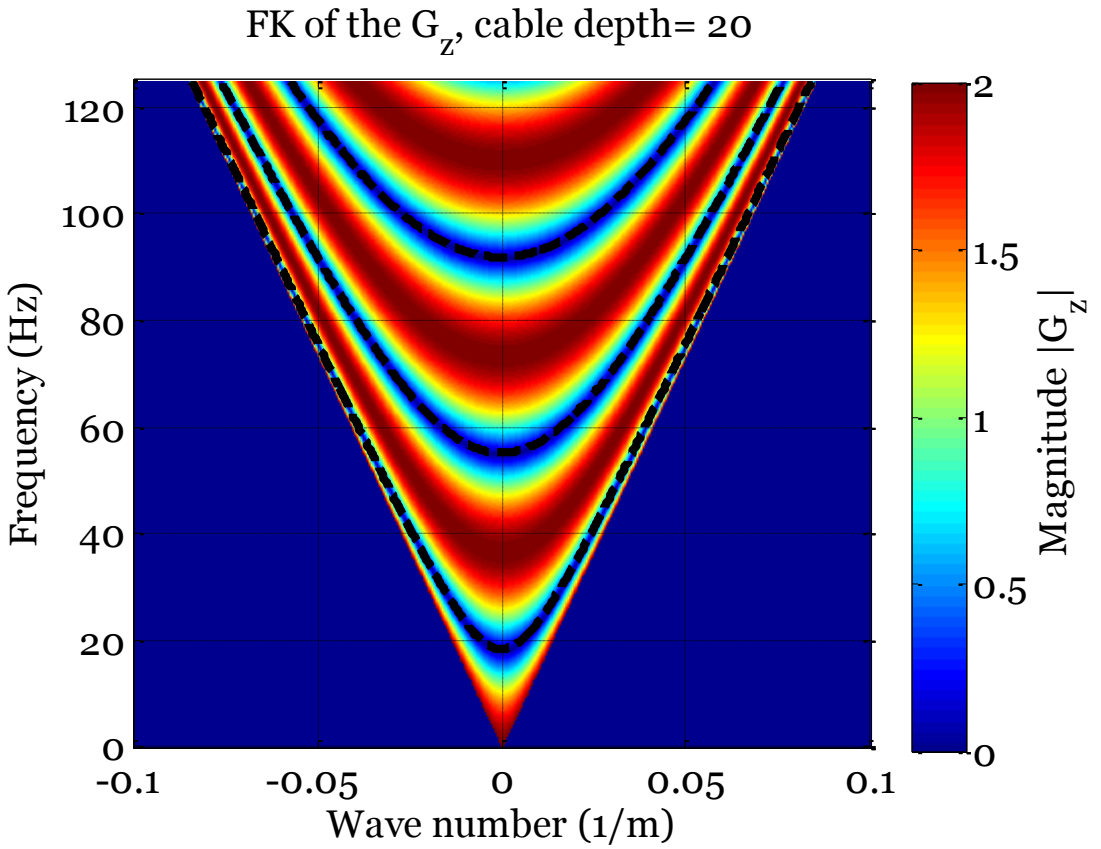

Figure 5: The Frequency-Wavenumber plot of the ghost operator Gz.

Figures below show the magnitude of the ghost operators at vertical incidence.

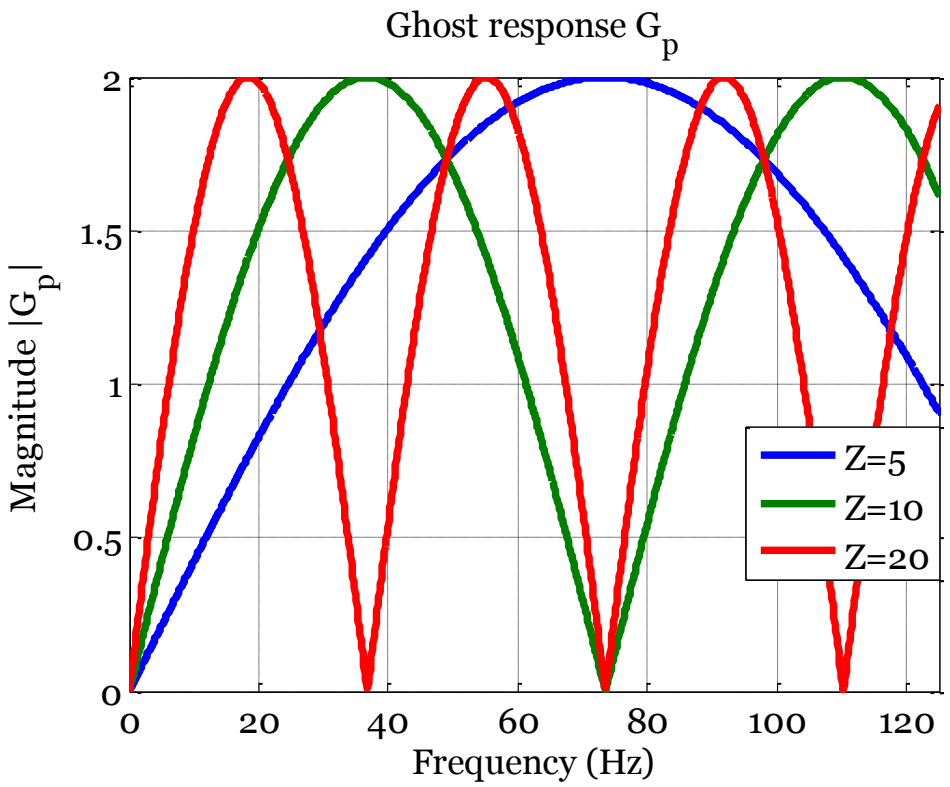

Figure 6: The magnitude response of the ghost operator Gp at vertical incidence.

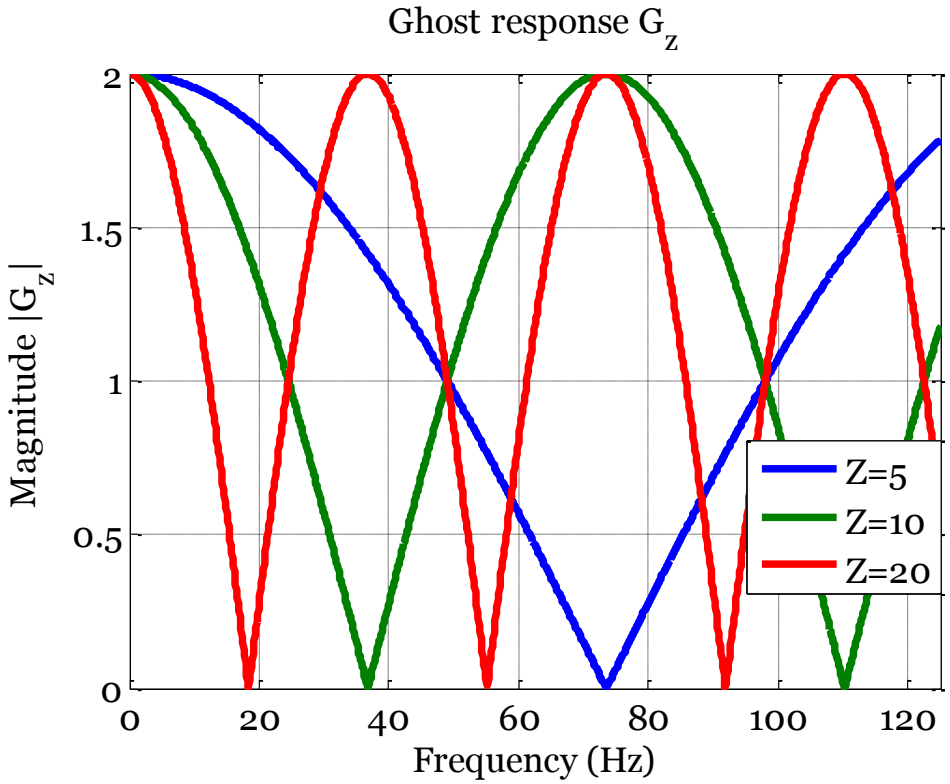

Figure 7: The magnitude response of the ghost operator Gz at vertical incidence.

3.3 Deghosting Algorithms

Deghosting is referred to as separation of the up-going and down-going wave field from the "total pressure" wave field. Since the two-component streamer records two independent wave fields; this allows us to separate the "total pressure" wave field into the "up-going" and "down-going" pressure wave field with data processing.

In this thesis, ware going to discuss two deghosting methods for two-component streamers.

- Pressure-particle velocity summation (PZSUM)
- Phase correction and adding (dephase and sum)

3.3.1 PZSUM

The PZSUM algorithm estimates the up-going wave field as a weighted average of the P and Z measurements:

$$P_U(f,k_x,k_y;z)=\frac{1}{2}\left[P_T(f,k_x,k_y;z)+\frac{\rho f}{k_z}Z(f,k_x,k_y;z)\right]. \tag{18}$$

The pressure-particle velocity summation uses deterministic weights to combine the data measured by hydrophones and geophones. This algorithm depends on knowledge or estimation of only two parameters, namely the acoustic speed of sound in water and the density of the medium. The algorithm is not dependent on the cable depth and hence low sensitivity to rough sea perturbations.

PZSUM algorithm relies on the assumption that the pressure and particle motion measurements have similar noise levels; however this is not always the case. When one of the measurements is noisier than the other measurement the estimate of the PZSUM algorithm will be adversely affected (OZDEMIR et al., 2011).

3.3.2 Dephase and sum:

The dephase and sum algorithm (herein called "DPS" deghosting algorithm) is a ghost model-dependent deghosting algorithm (Posthumus, 1993). This method applies a phase correction for the ghost delay to both the pressure and particle motion measurements, and tries to fill the notches by adding the two signals. This method attempts to fill the notches in the amplitude spectrum as well, by taking the amplitude effect of the ghost into account. To be more precise, the DPS algorithm estimates the up-going wave field by first filtering the pressure and particle motion measurements with the conjugate of the respective ghost operators to remove the phase effect of the ghost, and then sum the dephased data to fill the notches.

As a reason of the fact that the DPS algorithm relies on the ghost model, this algorithm reduces the noise on the deghosted data as compared to PZSUM algorithm (OZDEMIR et al., 2011).

In order to do this deghosting operation, we need to design a filter which corrects both the phase and the amplitude effect of the ghost operator. Having the pressure and Velocity streamer outputs as input to this filter, the desired output of such filter is the up-going wave field.

$$H\left(P_T(f,k_x,k_y;z),Z(f,k_x,k_y;z)\right)=U(f,k_x,k_y;z)\,. \tag{19}$$

For instance, if we multiply the acquired data by the complex conjugate of the respective ghost operators, the phase effect is cancelled and the magnitude of the ghost response is squared:

$$P_T(f,k_x,k_y;z)G_P^*(f,k_x,k_y;z)=4\sin^2(2\pi k_z z)P_U(f,k_x,k_y;z)\,, \tag{20}$$

$$Z_T(f,k_x,k_y;z)G_Z^*(f,k_x,k_y;z)\frac{f}{ck_z}=4\cos^2(2\pi k_z z)P_U(f,k_x,k_y;z)\,. \tag{21}$$

The DPS method sums the dephased measurements to get an estimate of the up-going wave field:

$$P_{U_{DPS}}(f,k_x,k_y;z)=\frac{1}{4}\left[P_T(f,k_x,k_y;z)G_P^*(f,k_x,k_y;z)+G_z^{\,*}Z_T(f,k_x,k_y;z)G_Z^*(f,k_x,k_y;z)\frac{f}{ck_z}\right]. \tag{22}$$

4 Synthetic data

In this thesis we will analyze a synthetic dataset which is generated by simulation of the acquisition with two-component streamer. The data has been provided by "**WesternGeco"**.

This elastic reservoir model is based on the North Sea Gullfaks oil field and also known as Task 1 model. It has 3D-spreading with a realistic 2.5D geology which is invariant in cross-line direction (Figure 8).

A line of source positions (25m increment) at a depth of 5m was computed for each top surface condition for a total of 2*281 shots. Every shot position was shot twice, once with a free surface and once with an absorbing top-boundary condition. Regularly spaced carpets of receivers (12.5m x 12.5m), containing each of one hydrophone (pressure) and one geophone (Vz velocity) were recorded at depth levels of 5m, 10m, 15m and of 200m, where the latter is equivalent to the seafloor. Each carpet has a cross-line extension of 500m and an inline extension of 10000m with 41x801 receiver positions.

A seismic trace itself is characterized by 1000 samples of 6ms sampling interval, where the first sample is set to 6ms.

We have two models for each data set of geophones and hydrophones:

- Absorbing boundary surface
- Free surface

The dataset with the absorbing boundary surface has no ghosting element. This is due to the assumption we have made that there is no difference in the density at the sea surface between the water and the air. The free surface model has notches.

As described, we have 41 streamers in this model. We chose the first streamer with depth level of receiver carpet at 20 meter in our simulations. There are 801 traces on the first line. A seismic trace itself is characterized by 1000 samples of 6ms sampling interval, where the first sample is set to 6ms.

The units of the data are Pa for pressure and m/s for velocity.

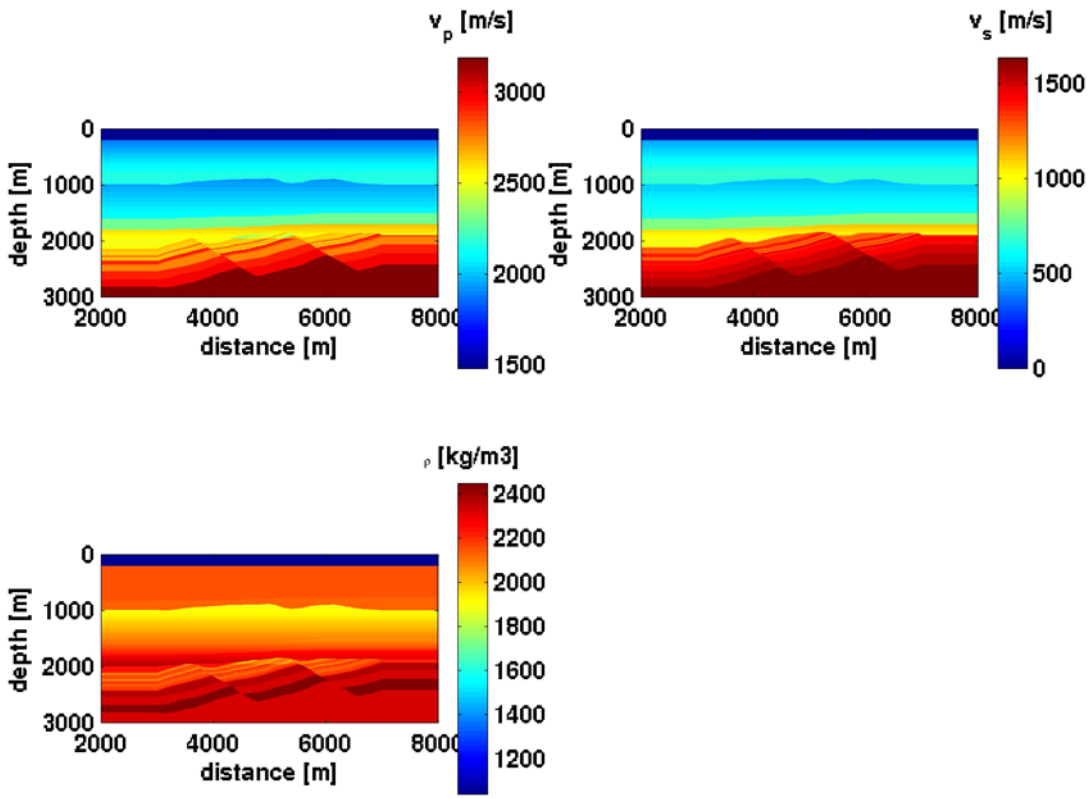

Figure 8: Elastic parameters for the Task1 "slab" model,

Picture from (Task1, WesternGeco).

4.1 Preprocessing

It has been previously observed that there was a 1.5ms time shift between P and Z component. More likely, this shift is originating in a staggered grid effect where the vertical component is extracted one grid point below the seabed – water interface and the pressure (FD cell size = 5m). As a pre-processing step; we corrected this delay of 0.25 samples in time.

The synthetic data had relatively low energy at low and high frequencies. Therefore, we decided to modify the frequency content of the synthetic data in order to get higher energy at low and high frequencies. We have designed a band stop zero-phase filter using a low pass and a high pass filter. We wanted to boost the data at frequencies lower than 20 Hz and 50-70 Hz in order to increase the energy level.

Figure 9 shows the magnitude and phase response of the filter we have designed to boost the up-going wave field. Figure 10 show the spectrum of pressure and particle velocity wave fields before and after modifying the spectrum of the synthetic data. We can see from the plots that the signal at frequencies below 20 Hz has been boosted almost by 20 dB.

We have also removed the direct arrival from the dataset by applying a 2D time-position mask on the data. Direct arrival does not fit to the ghost model as it is not reflected from sea surface.

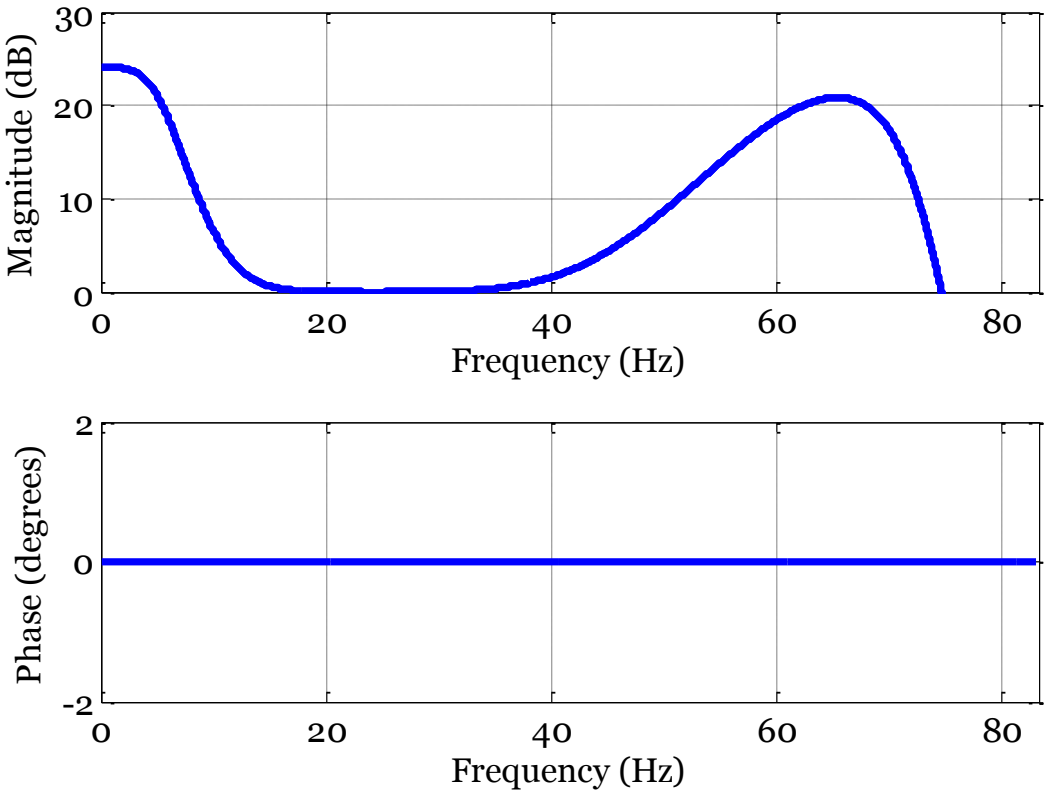

Figure 9: Magnitude and phase response of the boosting filter.

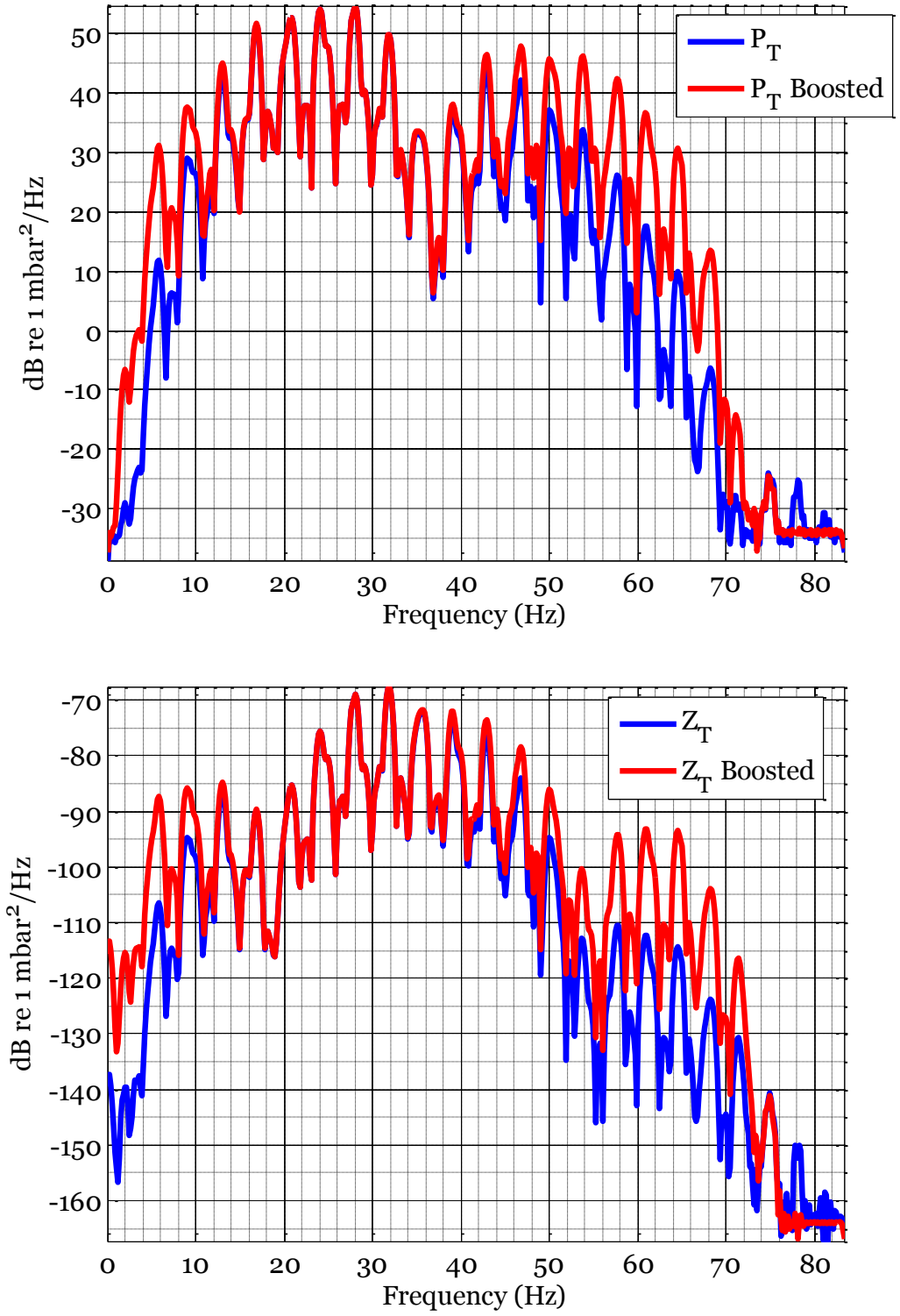

Figure 10: The spectrum of the total pressure (top) and particle velocity (bottom) before and after modifying the spectral content of the synthetic data.

4.2 TX Plots and FK Spectra

Figure 11 shows the TX plots of the total pressure and particle velocity wave field before and after direct arrival has been removed. The horizontal and vertical axis denotes the receiver position and the sample time respectively. The amplitude of the wave field is colour encoded. Direct arrival and sea bottom reflection are marked in the figure.

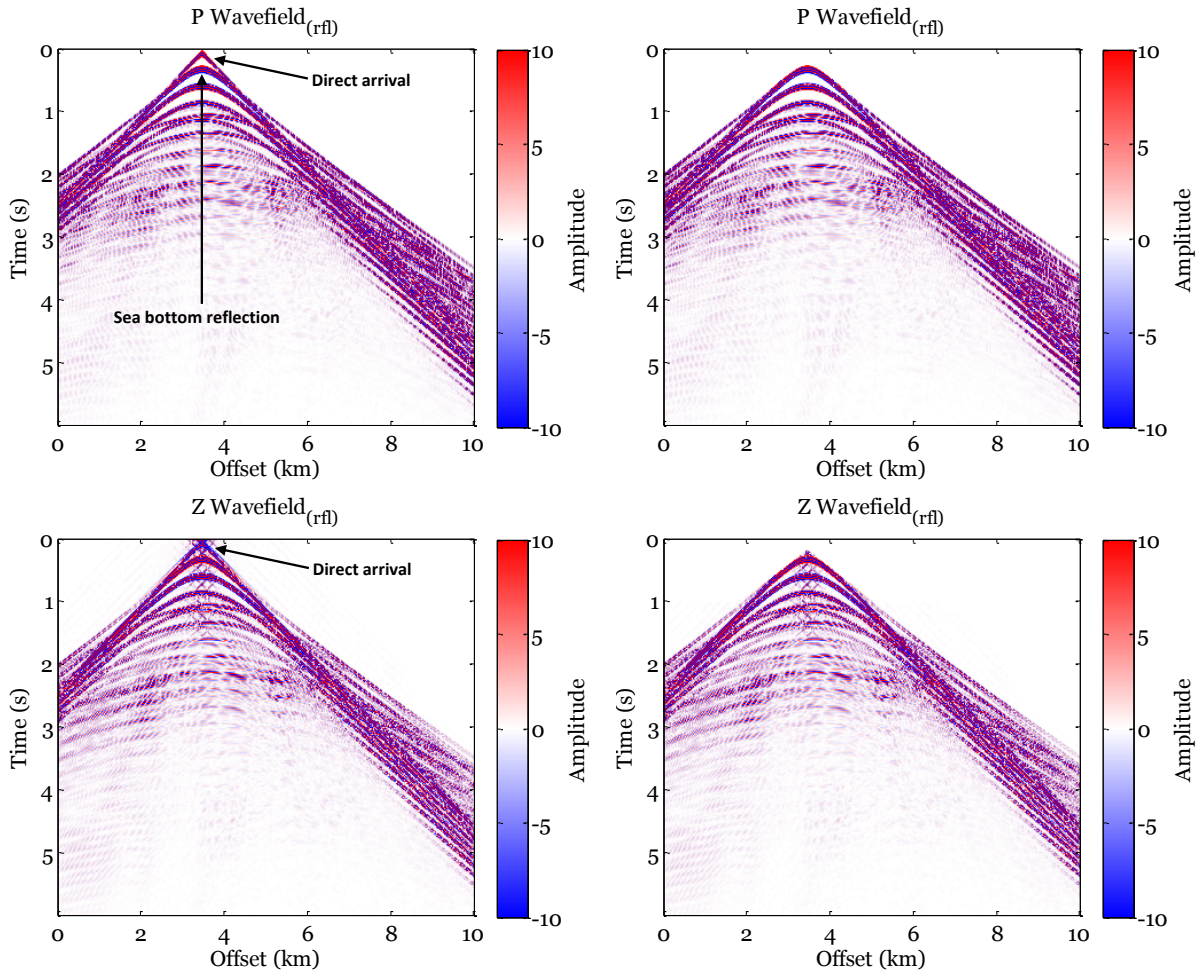

Figure 11: TX plot of the total pressure (top) and particle velocity (bottom) before (right) and after (left) direct arrival removal.

Figure 12 and Figure 13 show the TX plots of the pressure wave field for the absorbing boundary and free surface. The direct arrival and the sea bottom reflection are shown in Figure 12. We note that, the data set with the absorbing boundary surface has no ghost element. This is due to the assumption we have made that there is no difference in the density at the sea surface between the water and the air, while at Figure 13 also the pressure wave field reflected from the free surface is contaminated by both receiver ghost and surface related multiples. Deghosting algorithms such as PZSUM will remove the receiver ghost; however surface-related multiples will remain in the data after deghosting.

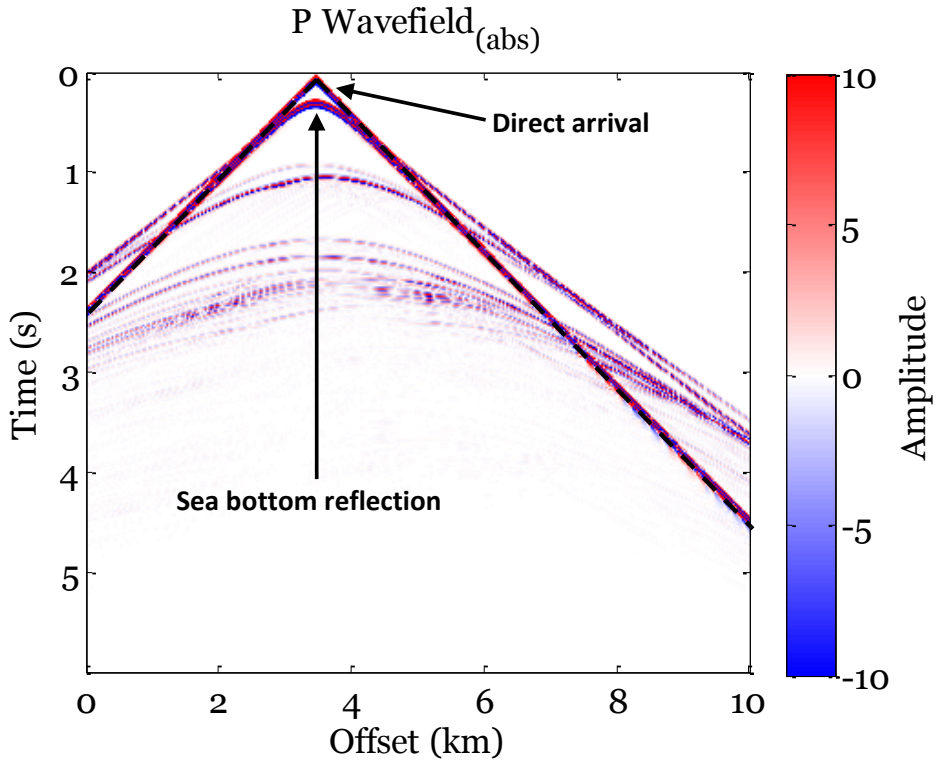

Figure 12: TX plot of the pressure wave field for the absorbing boundary surface.

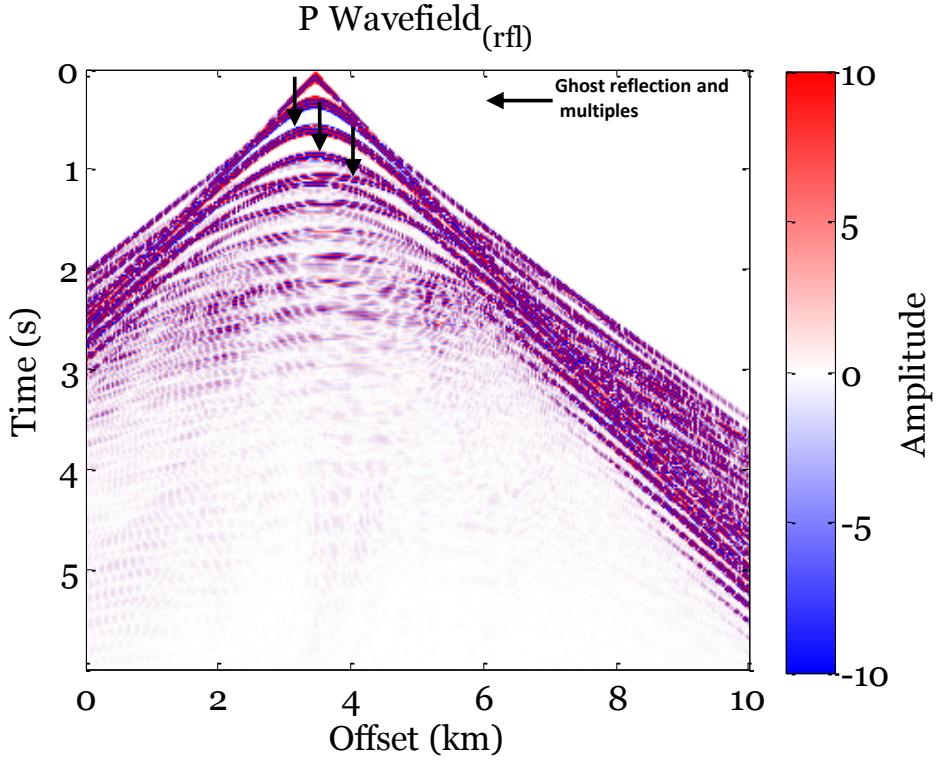

Figure 13: TX plot of the pressure wave field for the free surface.

Figure 14 and Figure 15 show the FK plots; also 2D Fourier Representation of the total pressure and particle velocity wave field with free surface in dB. The horizontal axis shows the wave number (1/m) and the vertical axis the frequency (Hz).The dashed lines indicate the expected location of the ghost notches which has been derived by the Eq. (16) and (17) described in Chapter 3.2.3. We can see from the plots that the location of ghosts in the simulated data does match with the theoretical location in the pressure and particle velocity wave fields.

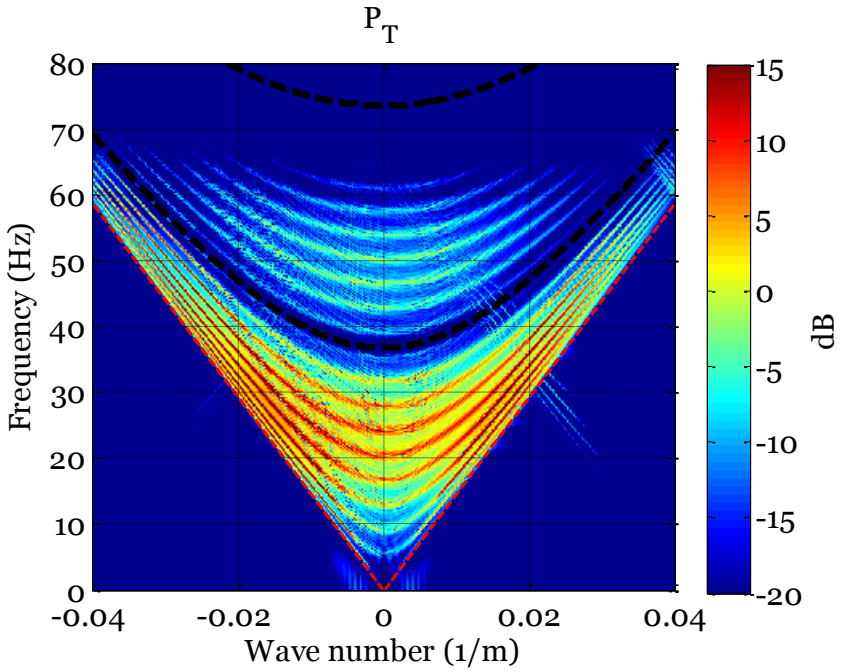

Figure 14: FK plot of the total pressure wave field for the free surface.

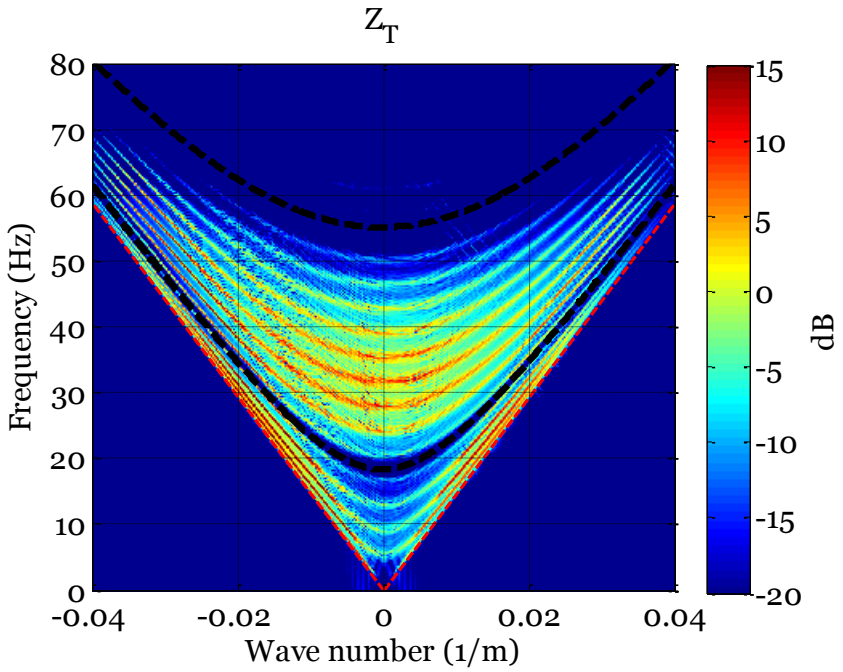

Figure 15: FK plot of the total particle velocity wave field for the free surface.

Figure 16 and Figure 17 show the sea bottom reflection of the pressure and particle velocity wave field for the absorbing boundary (blue) and free surface (green). The dataset in these plots has been up-sampled for display purpose. The original dataset has been marked with circles. Comparing the result for absorbing boundary and free surface in each of the plots, we can see the ghost reflection in green line. As mentioned before, the absorbing boundary surface is ghost free due to the assumption of having zero difference in the density between the sea-water at the sea surface.

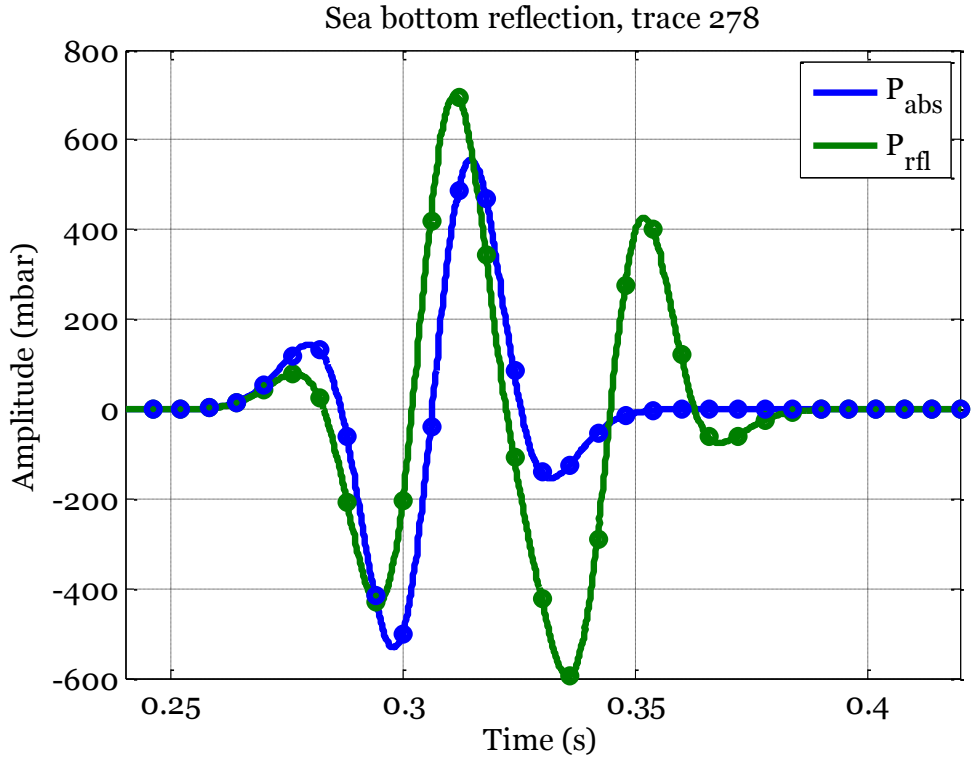

Figure 16: Line plot of the pressure wave field at the sea bottom reflection for both absorbing boundary (blue) and free surface (green).

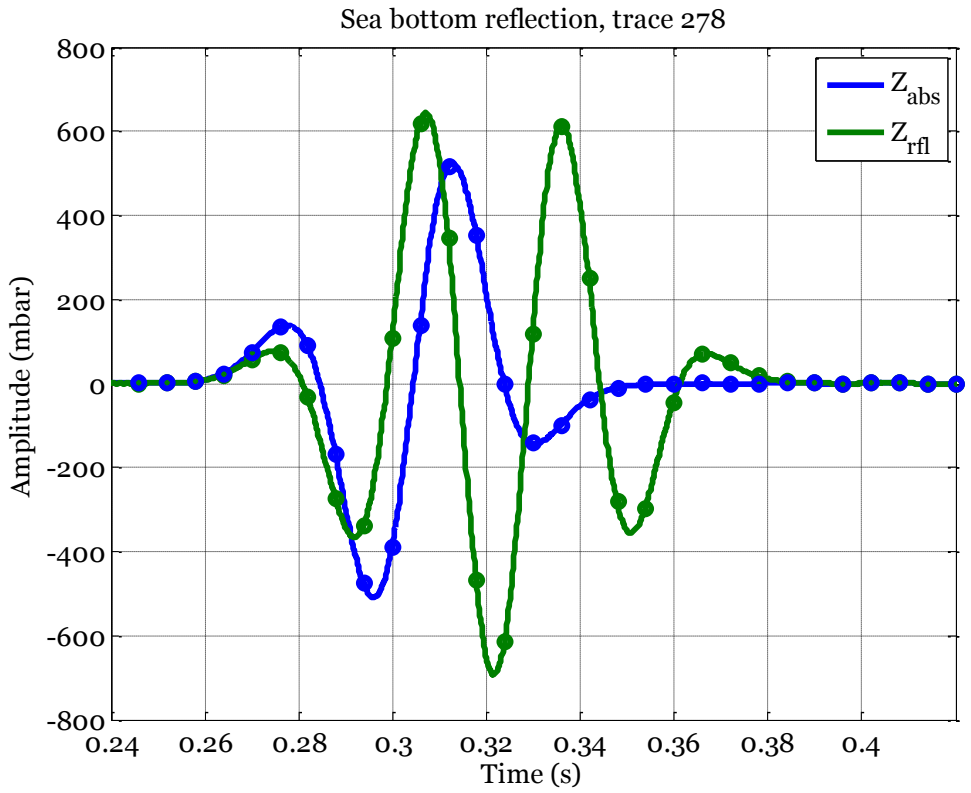

Figure 17: Line plot of the particle velocity wave field at the sea bottom reflection for both absorbing boundary (blue) and free surface (green).

4.3 Deghosting

We have used the PZSUM algorithm to remove the receiver ghost. Figure 18 shows the TX plot of the up-going wave field computed by using the PZSUM method. The plot indicates that by performing PZSUM, we have managed to attenuate the destructive interference of the down-going wave field. The result shows the ghost-free up-going wave field, however surface-related multiples will remain in the data after deghosting.

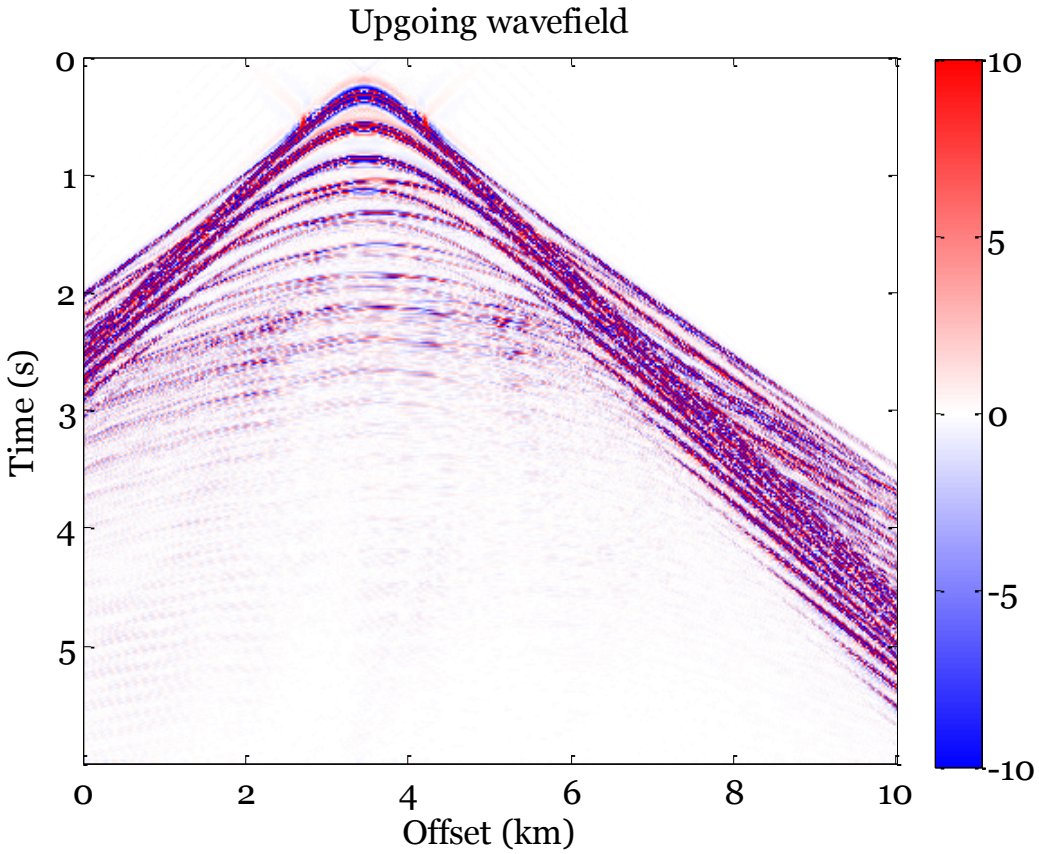

Figure 18: TX plot of the up-going wave field.

Figure 19 shows the FK plot of the up-going wave field. The black dashed lines indicate the place of ghost notches in the wave field before deghosting. We can see from the plot that the place where ghost notches occurred in the pressure and particle velocity data has been filled in the spectrum after deghosting.

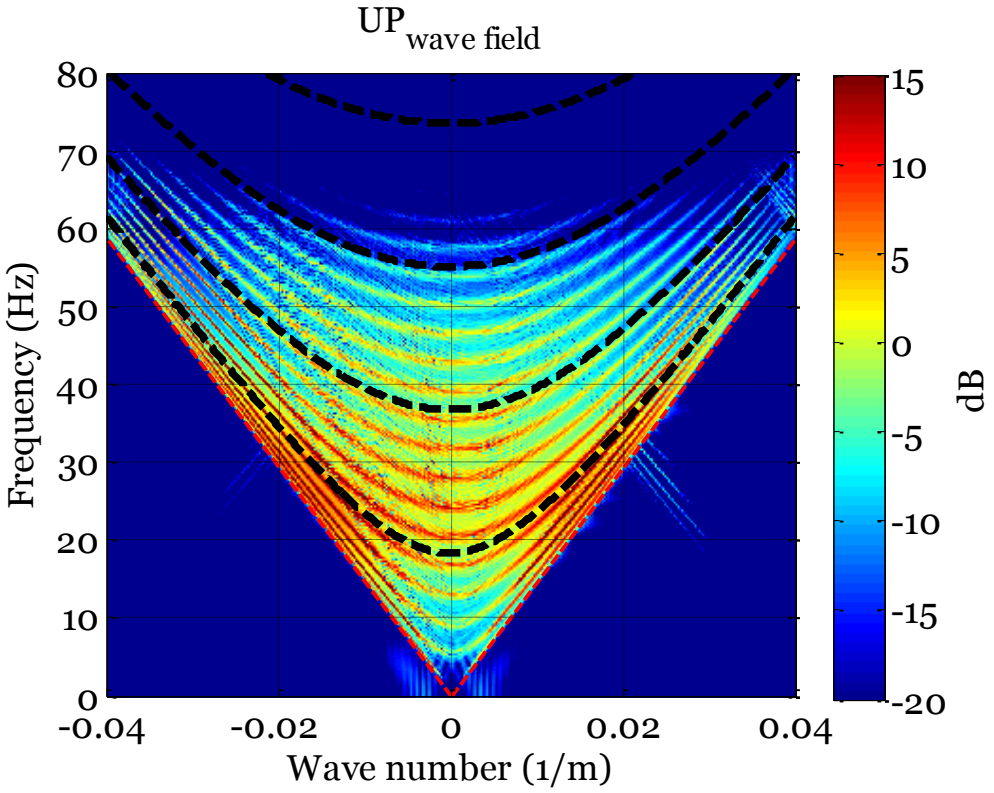

Figure 19: FK plot of the up-going wave field. Black dashed lines define the place of ghost notches.

Figure 20 shows the sea bottom reflection of the pressure (blue), particle velocity (green) and up-going (red) wave field. Red line, also the line plot of the up-going wave field indicates that the ghost reflections are removed after deghosting.

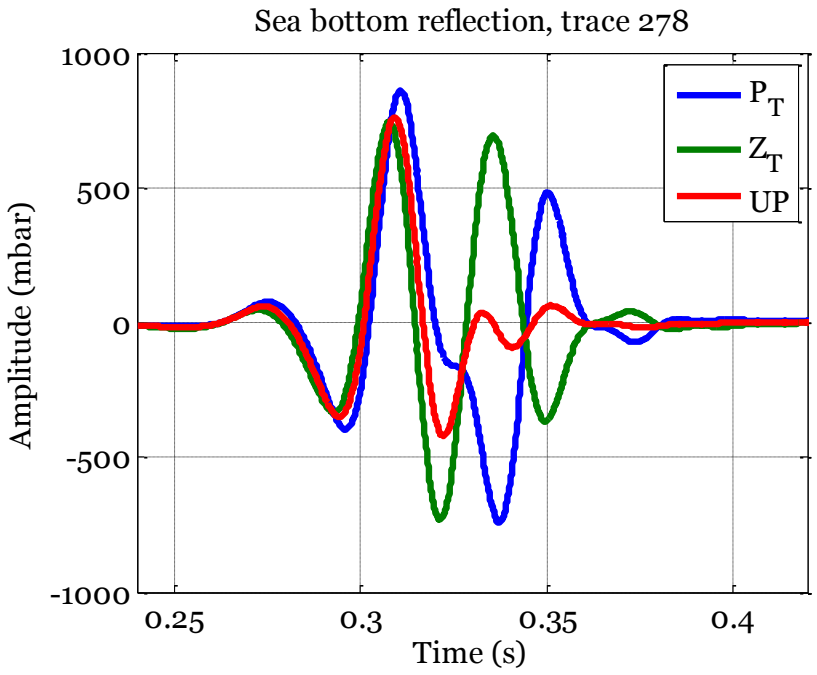

Figure 20: Line plot of the pressure (blue), particle velocity (green) and up-going wave field (red) at the sea bottom reflection.

Figure 21 shows the FK slice of the total pressure (blue), particle velocity (green) and up-going (red) wave field at wavenumber K = 0. The red line shows the ghost-free up-going wave field after deghosting. We observe a ghost notch in the FK slice of the pressure wave field at about 37 Hz and two ghost notches in the FK slice of the particle velocity wave field at 18 and 54 Hz. We can see that the notches are filled after performing PZSUM (red line).

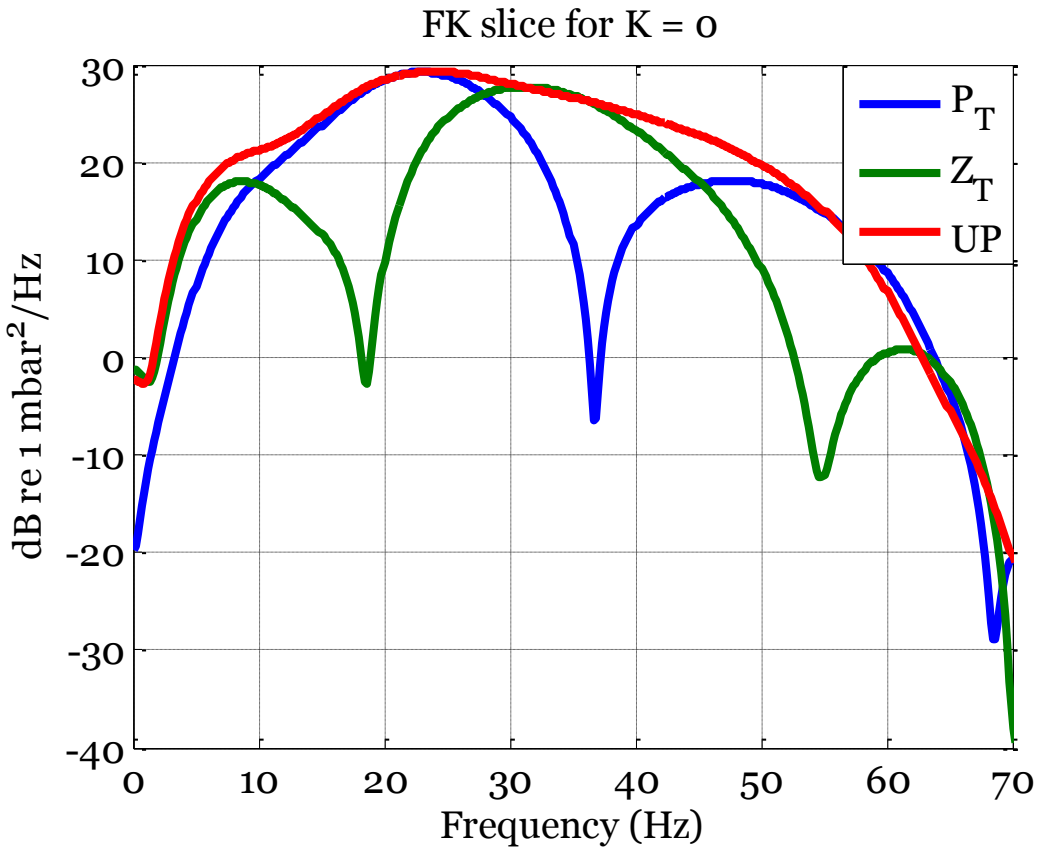

Figure 21: FK slice of the pressure (blue), particle velocity (green) and up-going (red) wave field.

5 Group forming

In order to improve signal to noise ratio seismic acquisition systems, we can sum the response from a large number of individual sensors. This is known as group forming.

Group forming can be done in two ways:

- Analog Sum
- Digital group forming

The Analog Sum method relies on hardwiring the output of individual sensor within an array together to give an analog array response. The array response is then digitized. The individual sensors which are forming the group are often distributed with non-equivalent distance spacing. Mahoney and Newman (1971) shows that the performance of this method is degraded by errors in the positioning and sensitivity of the individual sensor elements.(Martin et al., 2000)

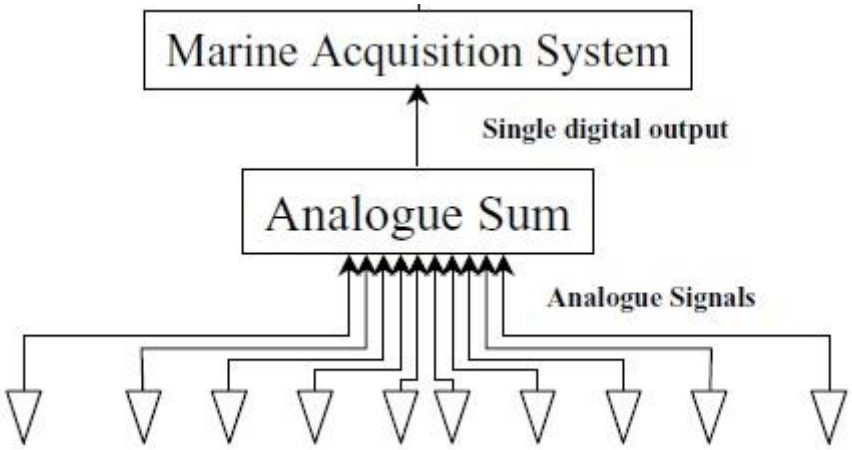

Figure 22: Illustration of Analog group forming.

Picture from "Acquisition of marine point receiver seismic data with a towed streamer", (Martin et al., 2000).

Digital group forming (DGF)

This method involves recording of data from individual point receivers which are distributed along the length of each streamer. The digitized output of large number of these individual sensors then may be summed to a single output.

DGF improves the signal-to-noise ratio and broadens the recorded seismic data spectrum. This can result in clearer image with higher structural resolution. One of the advantages with this method is that the dataset can be up-sampled and we can generate the quantized output at places where there is no receiver as well.

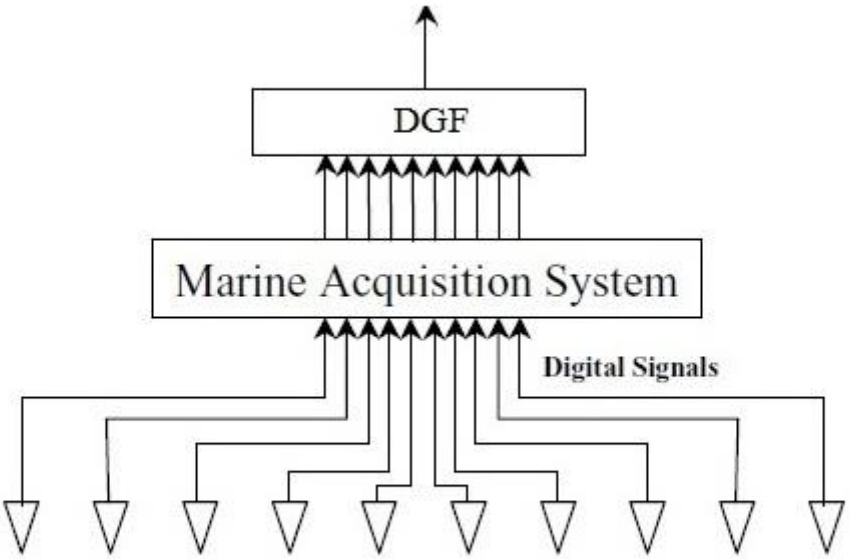

Figure 23: Digital group forming.

Picture from "Acquisition of marine point receiver seismic data with a towed streamer" , (Martin et al., 2000).

There are different layouts of how the sensors should be placed along the streamer based on the expected result. In this thesis we will study the MSX group (Geophysical, 2006) layout and use it for group forming our synthetic data.

5.1 MSX™ Solid Active Streamer

MSX™ is the active cable and hydrophone group layout developed by ION geophysical. This layout benefits use of tapered arrays with receiver-optimized pattern to reduce noise. Each group consists of 14 hardwired hydrophones. Hydrophone groups are center-weighted which means that the output of all the sensors in the group are summed to a single output and positioned at the center of group; with a group spacing of 12.5 m and group length of 17.55 m, groups are overlapped by 29 %.(Geophysical, 2006)

The MSX layout distribution of is as follow:

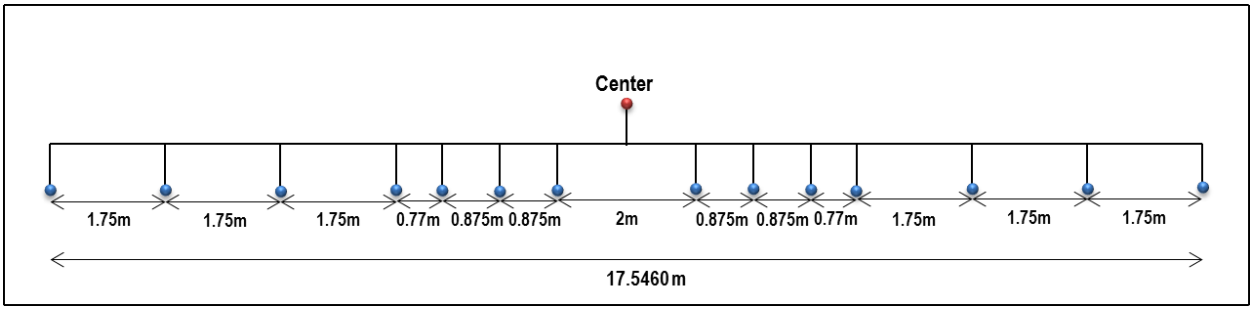

Figure 24: MSX hydrophone group layout with 12.5 m group spacing.

Figure 26 shows the MSX hydrophone locations and the group layout with a group spacing of 12.5 m along the streamer for 8 groups.

The synthetic data we are going to analyze in this thesis has a sensor spacing of 12.5 m along the streamer. Hence we need to up-sample our synthetic data to a denser grid in order to generate output at the locations defined by the MSX group layout, and then sum the output of sensors at these positions into one single output. Although MSX group layout is designed for hydrophone streamers, we decided to apply the same grouping layout on the particle velocity data generated by geophone sensors.

We have decided to use the simplified approximation of MSX layout group forming our data. The quantized MSX layout we decided to use has almost the same filter response as MSX layout. Figure below shows the quantized MSX layout consist of 14 sensors with 12.5 m group spacing.

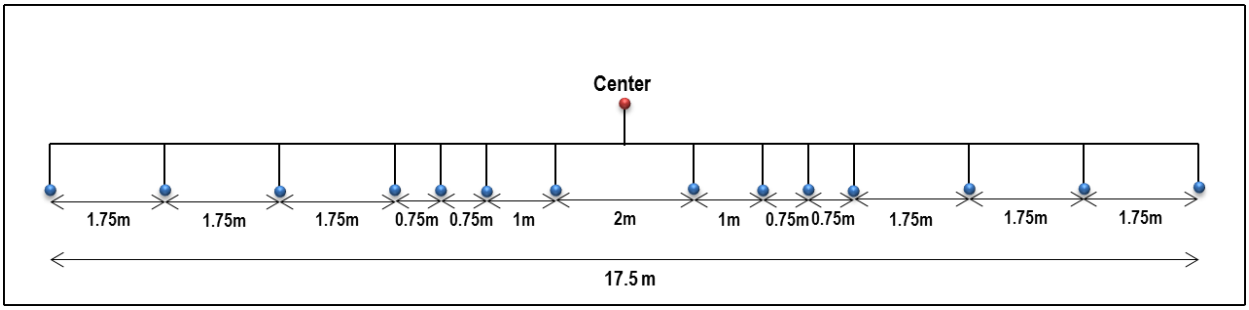

Figure 25: Quantized MSX group layout with 12.5 m group spacing.

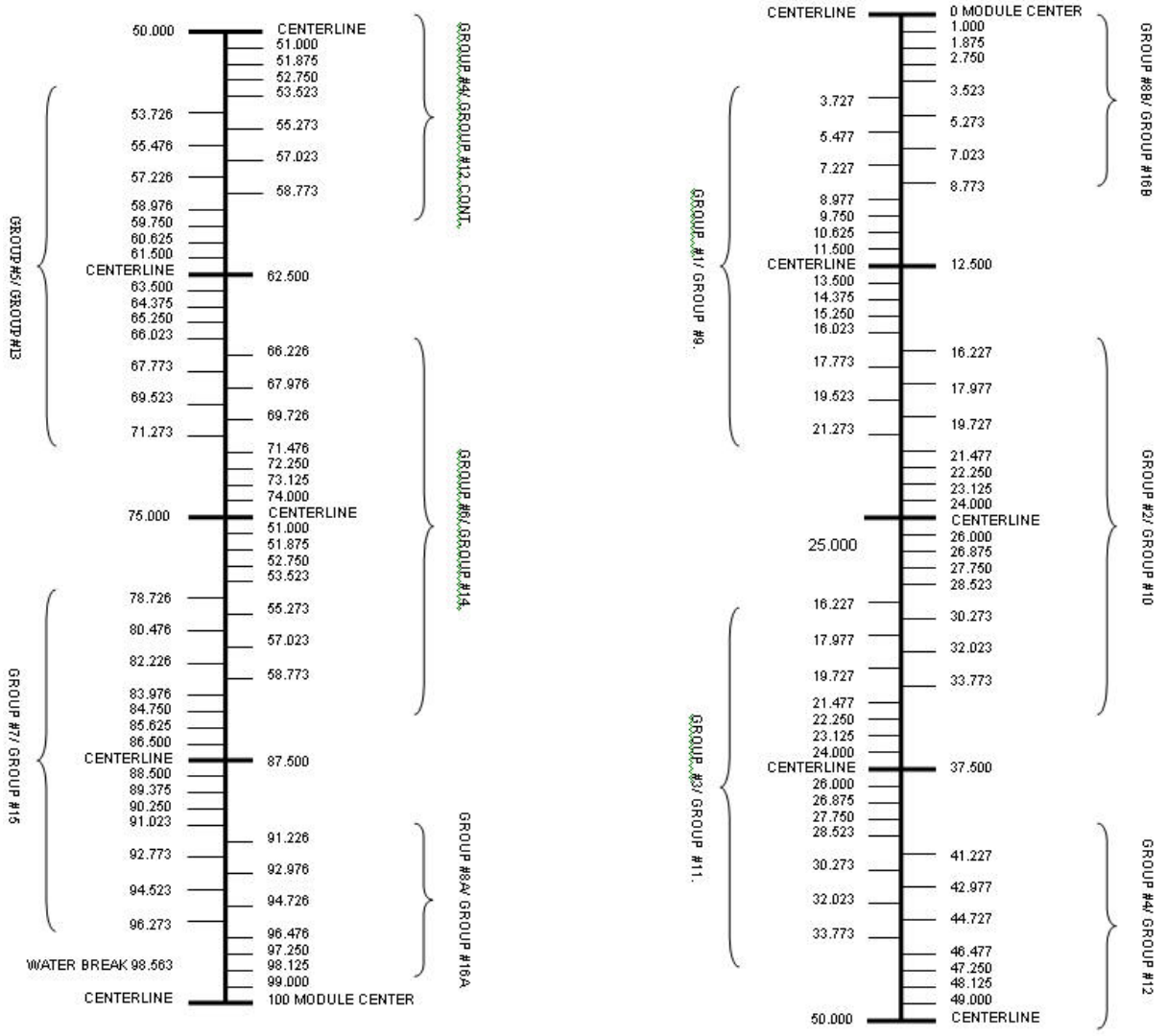

Figure 26: MSX hydrophone group layout with a group spacing of 12.5m. The picture shows hydrophone locations along the streamer for 8 groups.

Picture in Figure 26 has been taken from ”MSX™ Solid Active Streamer Section written by ION geophysical company” (Geophysical, 2006).

Figure 27 and Figure 28 show the filter response of the MSX group layout and the quantized MSX group layout. We can see from Figure 28 that the response of both layouts are equal up to wavenumber K=0.04 [1/m] which spans the wavenumber spectrum of interest in our data.

Having a spatial sampling interval d=12.5 m (sensor spacing), spatial frequency (wavenumber) K should follow Nyquist–Shannon sampling theorem $|K| \leq \frac{1}{2d} = 0.04\ [1/m]$ in order to prevent aliasing.

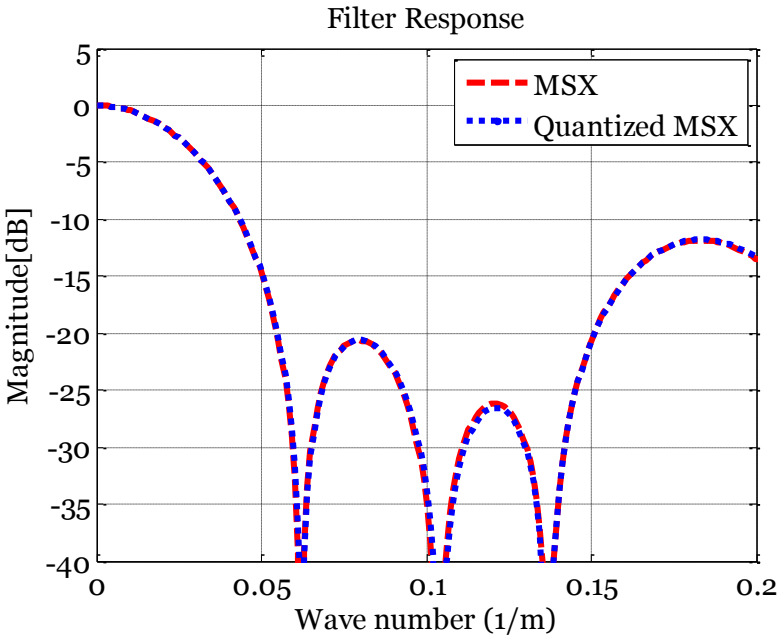

Figure 27: Filter response of the MSX group layout (Red dash line) and quantized MSX group layout (Blue dot line).

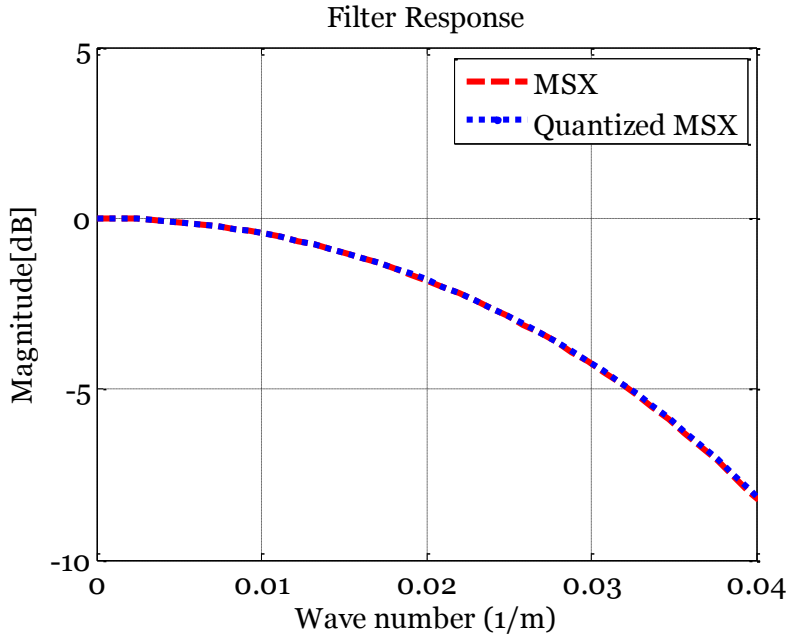

Figure 28: Zoomed filter response of the MSX group layout (Red dash line) and quantized MSX group layout (Blue dot line).

Figures below show the FK plots of the total pressure, particle velocity and up-going wave field after group forming (right plots) and the difference between each named wave field before and after group forming. The plots on the right show that performing group forming attenuate signals arriving at very high apparent velocity (large wavelength). It will suppress signal energy and unwanted noise at side lobes and focus on the signal energy propagating toward main lobe of the array pattern. Group forming data enhanced signal-to-noise ratio about 6dB.

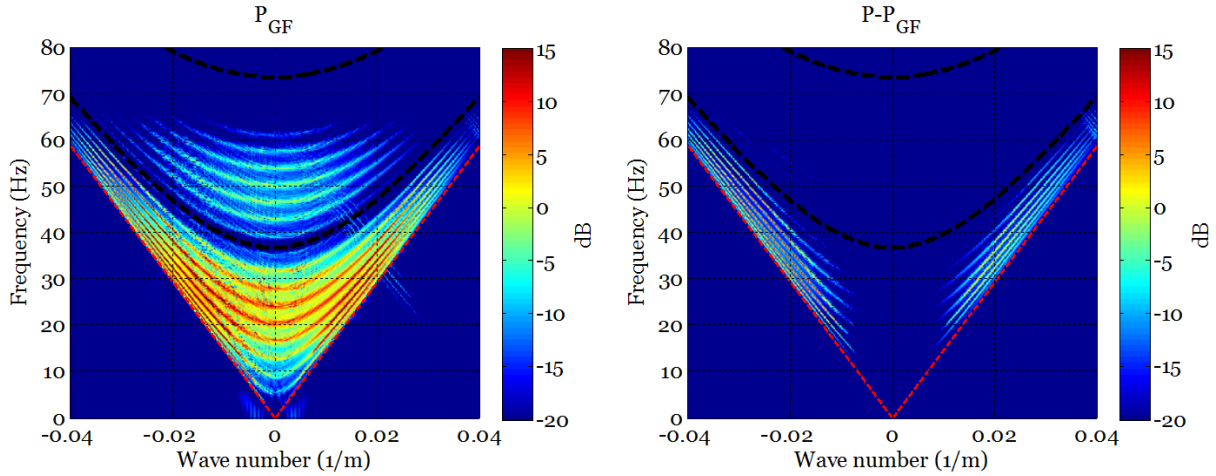

Figure 29: FK plot of the total pressure wave field after group forming (right) and the difference between total pressure wave field before and after group forming (left).

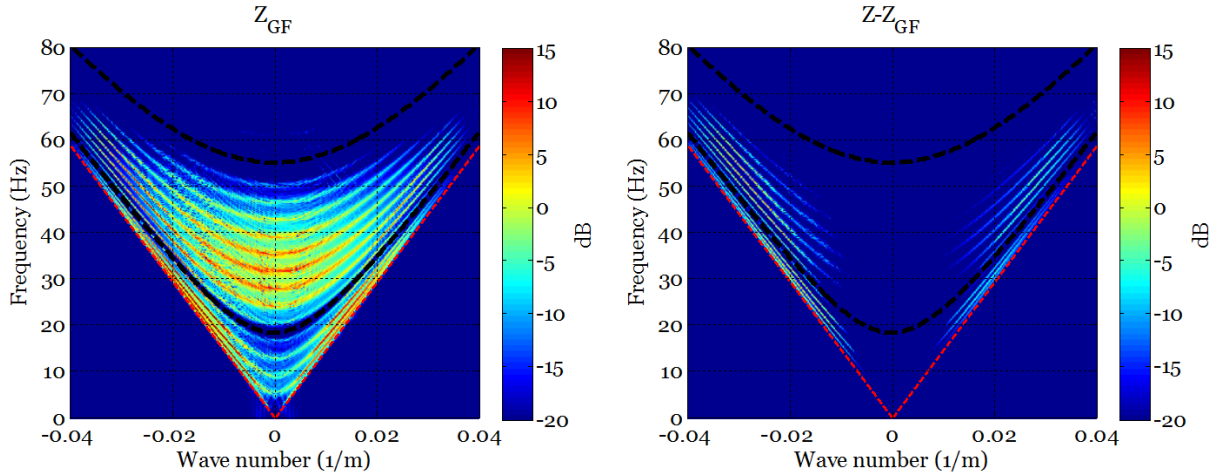

Figure 30: FK plot of the total particle velocity wave field after group forming (right) and the difference between total particle velocity wave field before and after group forming (left).

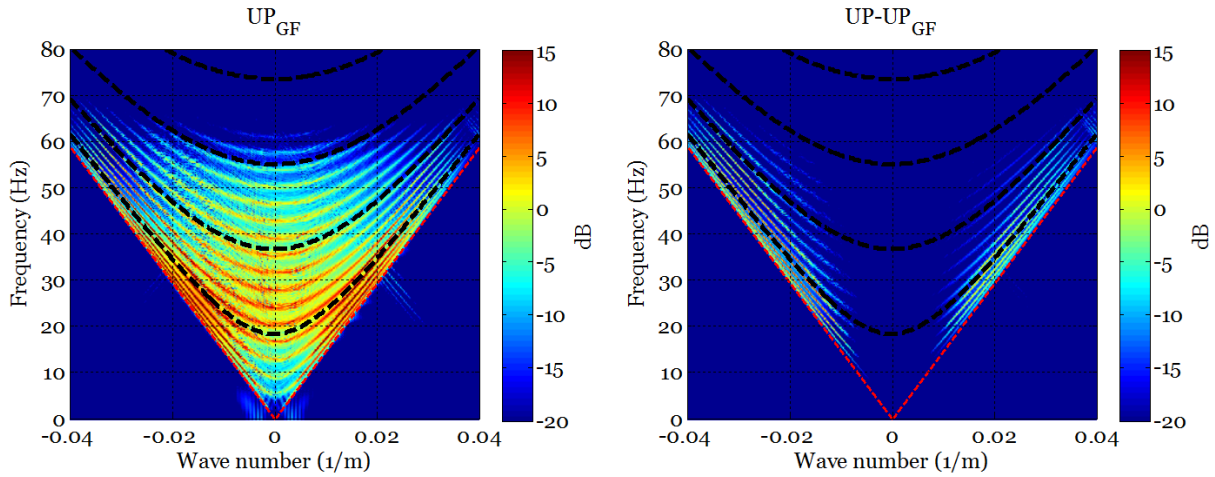

Figure 31: FK plot of the up-going wave field after group forming (right) and the difference between up-going wave field before and after group forming (left).

6 Perturbations

Every system and operation is associated with specific type of noise and interference related to that system or mechanism. Some of them are critical while some unimportant in terms of compromising the quality or the execution of the task. As a part of developing a new technology or product, there will be put a lot of effort to study and identify the possible perturbations associated with that system. The goal is to improve and minimize that impact of the identified perturbations. There would always be a trade-off between quality and cost. Marine seismic acquisition is neither an exempt in this matter. There are a lot of factors and element which can have highly negative impact on the result during an acquisition. It could be a production fail, human error or natural uncontrolled conditions and circumstances resulting in appearance of noise and interference on the result. In this chapter we introduce some of the perturbations and noise associated with the marine seismic acquisition system, and receivers (geophones and hydrophones). Based on our research we have chosen to study and investigate the impact some of the perturbations which can result in significant noise on the data or are easy to be fixed. I will also analyze and quantify the impact of chosen perturbations on the synthetic data provided by WesternGeco. The synthetic data are generated with simulations under controlled and ideal conditions except the sea-surface reflection of signal. Hence we apply each perturbation individually on the data and study its impact.

This thesis does not cover all the perturbations associated with marine seismic acquisition.

6.1 Geophone transfer function

There are several types of geophones such as velocity, acceleration, and digital geophones used in seismic exploration. Velocity geophones are mostly used in high-resolution land seismic exploration, but also in two-component streamers (Guilin, Gao, and Junyi, 2009).

As described in chapter 3.2.3, the synthetic seismic data we want to analyze is generated by two-component streamer that uses both pressure (hydrophones) and particle velocity sensors (geophones) to measure the seismic wave fields reflected from the earth. In this section we will introduce the typical velocity geophone impulse response and study the impact of the perturbations related to geophone transfer function on the seismic data quality.

6.1.1 Transfer function

The transfer function of the geophone depends on the natural frequency, damping, coil resistance and the sensitivity, as follow:

$$G(\omega) = \frac{\mathcal{S}}{1-2i\,\zeta\left(\frac{\omega_n}{\omega}\right)-\left(\frac{\omega_n}{\omega}\right)^2} \quad \text{, [V/m/s],} \tag{23}$$

(Hons and Stewart, 2006)

where $\mathcal{S}$ denotes the sensitivity; ω_n is the natural angular frequency; and ζ is the damping factor.

The sensitivity S and the damping factor ζ are given by:

$$\mathcal{S} = \frac{R_{shunt}}{R_{shunt}+R_{coil}}\mathcal{S}_0 \ , \tag{24}$$

$$\text{and } \zeta = \zeta_0 + \frac{{\mathcal{S}_0}^2}{4\pi\omega_n m(R_{shunt}+R_{coil})} \ , \tag{25}$$

Here R_{coil} is the coil resistance, R_{shunt} is the shunt resistance, S_0 is the (open-loop) sensitivity, ζ_0 is the open-loop damping and m is the moving mass.

We use the SM-24 geophone (I/O Sensor, 2006) element parameter values as the nominal values here.

	$\mathbf{f_n}$	$\boldsymbol{\zeta_0}$	$\boldsymbol{R_{shunt}}$	$\boldsymbol{R_{coil}}$	$\boldsymbol{\mathcal{S}_0}$	**m**
	10 Hz	0.25	1339 Ω	375 Ω	28.8 V/m/s	11 g
Tolerance	±2.5%	+5%	±2.5%	±2.5%	±2.5%	-

Table 1: Specification of the SM-24 geophone (I/O Sensor, 2006).

We assume that the perturbations are independent from each other and from one geophone to others.

The transfer function described above is represented in the continuous-time domain. We should transform it to the discrete-time domain in order to implement a digital filter to perturb our data. We have chosen to use the central difference approximation for S; and the square of the forward difference approximation for S^2 in order to map our filter from s-plane to z-plane as both approximations are valid below half the sampling rate. These approximations are described in (Press, Flannery, Teukolsky, and Vetterling, 1992) "Numerical Recipes in C, Chapter 5.7":

$$S \longrightarrow \frac{Z-Z^{-1}}{2T} \text{ (Central difference approximation),} \tag{26}$$

$$S^2 \longrightarrow \frac{Z-2+Z^{-1}}{T^2} \text{ (Square of forward difference approximation).} \tag{27}$$

Using Laplace transform substituting S with $i\omega$ in Eq. (23) gives the the nominal geophone transfer functions in continuous-time $\mathbf{H_a(s)}$ **.** Substituting S and S^2 in Eq. (28) with the approximations in Eq. (26) and Eq. (27) gives the nominal geophone transfer function in discrete-time domain $\mathbf{H_d(z)}$ as follow:

$$H_a(s) = \frac{\mathcal{S}}{1 + 2\zeta\omega_n\left(\frac{1}{S}\right) + {\omega_n}^2\left(\frac{1}{S}\right)^2} = \frac{\mathcal{S} * S^2}{S^2 + 2\zeta\omega_n S + {\omega_n}^2} \ , \tag{28}$$

$$H_d(z) = H_{nom}(z) = \frac{\mathcal{S} * (1 - 2z^{-1} + z^{-2})}{(1 + \zeta\omega_n T) - z^{-1}(2 - {\omega_n}^2 T^2) + z^{-2}(1 - \zeta\omega_n T)} \ , \tag{29}$$

Figure 32 shows geophone nominal transfer function response in discrete-time and continuous-time domain. We can see from the plot that the geophone responses in both domains are almost equal.

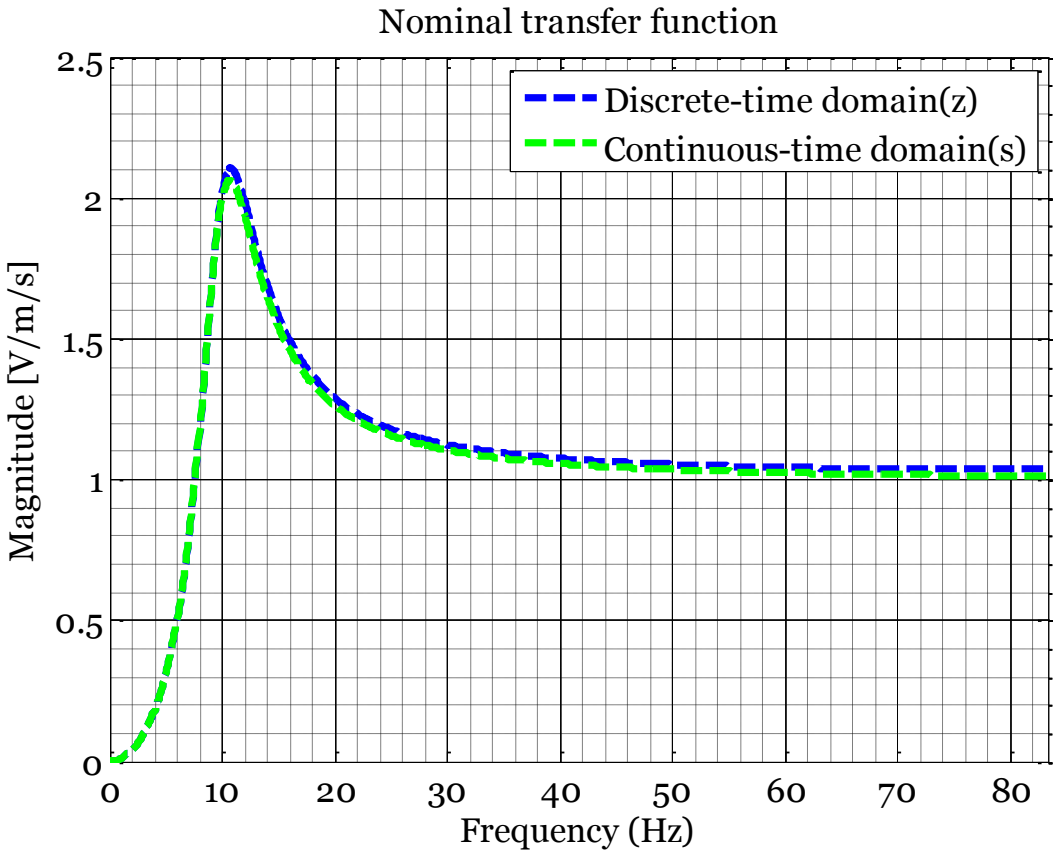

Figure 32: Geophone nominal transfer function response in s-plane and z-plane.

6.1.1.1 Natural frequency and Damping

There is always variation in the production of the sensors; therefore the sensors will have different response. Hence we start our analysis by perturbing the natural frequency and damping factor separately and look at the impact of them on the geophone response.

Figure 33 shows the overall error in the geophone response as a result of change in the natural frequency. We have perturbed the natural frequency by $\pm 2.5\%$. This figure shows that a change of $\pm 2.5\%$ in the natural frequency has high impact at low frequencies and barely any impact at high frequencies. We can see that the overall error at low frequencies goes up to about 5%.

Figure 34 shows the overall error in the geophone response with damping (ξ_0) + 2.5% and +5%. We can see from the plot that the error decreases with frequency increment. The overall error reaches to about 1.2% for 2.5% change and 2.4% for a 5% change in damping.

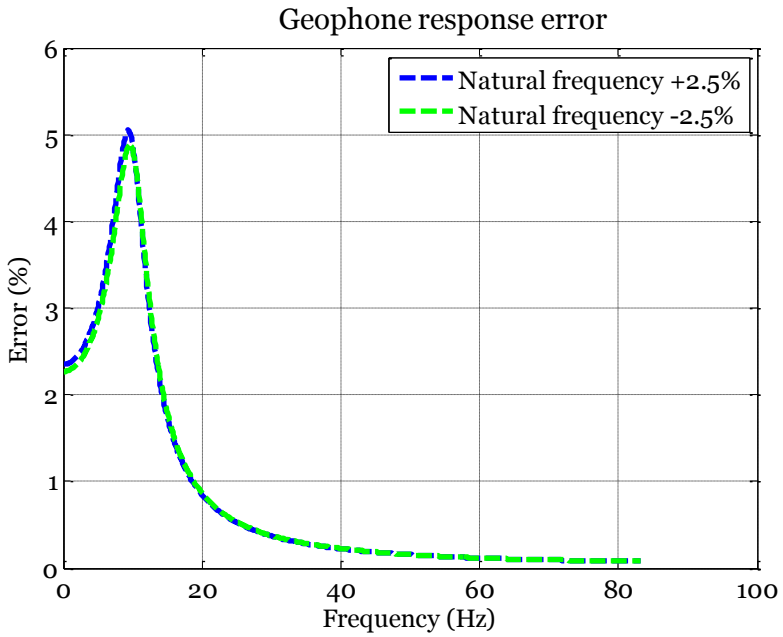

Figure 33: The error in the geophone response resulted by change in the natural frequency (f_n).

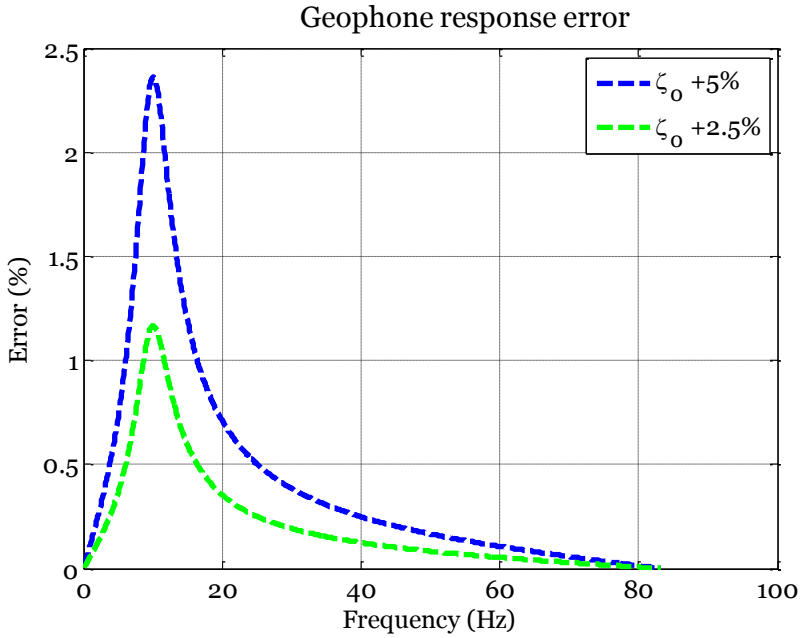

Figure 34: The error in the geophone response resulted by change in the open-loop damping factor (ξ_0)

The result in this section suggests that the tolerances in geophone specifications can be satisfactorily modeled by each perturbation independent from geophone to geophone.

We take one step further and study the impact of these perturbations on the synthetic seismic data gathered by geophones streamers and the acquired up-going wave field.

The synthetic seismic data acquired by the particle motion sensors in this thesis is the ideal unperturbed data. In order to perturb our data we need to perform the following filtering steps:

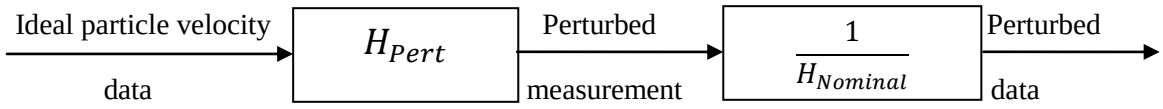

H_{Pert} denotes the perturbed geophone transfer function; and $H_{Nominal}$ the nominal geophone transfer function.

We first need to perturb our data by the perturbed geophone transfer function and afterward correct the effect on geophone response by the inverse of the nominal geophone transfer function. We have combined these two steps in a matching filter as follow:

$$\text{Matching Filter}(Z) = \frac{H_{Pert}}{H_{Nominal}} = \frac{\tilde{H}(z)}{H_{Nom}(z)} = \frac{\tilde{\mathcal{S}} * \left((1 + \zeta\omega_n T) - z^{-1}\left(2 - {\omega_n}^2 T^2\right) + z^{-2}(1 - \zeta\omega_n T)\right)}{\mathcal{S} * \left((1 + \zeta\widetilde{\omega_n} T) - z^{-1}\left(2 - \widetilde{\omega_n}^2 T^2\right) + z^{-2}(1 - \zeta\widetilde{\omega_n} T)\right)}, \quad (30)$$

where $\tilde{\mathcal{S}}$ and $\widetilde{\omega_n}$ are perturbed sensitivity and natural angular frequency. We assume that sensitivity factor is equal $\mathcal{S} = \tilde{\mathcal{S}} = 1$ in this section. We will analyze the sensitivity perturbation in a separate section.

Our approach is to perturb the natural frequency and damping factor both separately and together and afterward add these perturbations to the particle velocity data by the matching filter described above and simulate and quantify the impact of these perturbations on synthetic data. Our simulations include the following steps:

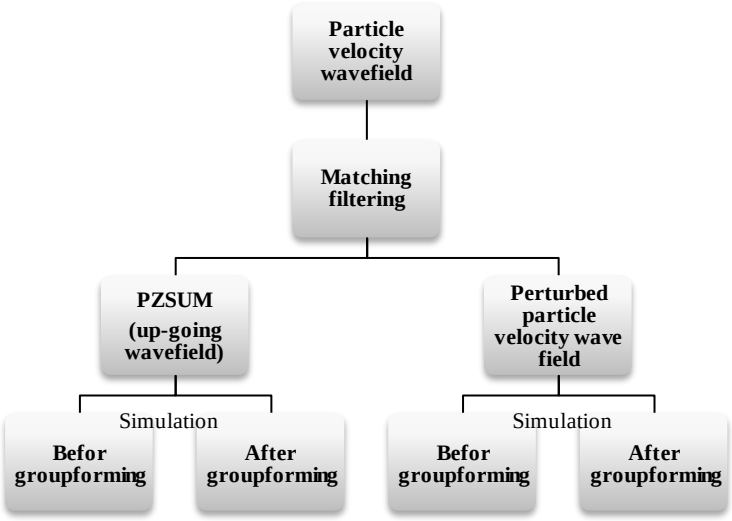

We have chosen three different tolerance levels of natural frequency and damping and perturbed the particle velocity wave field by the matching filter described above. These tolerance levels are in percentage and listed below:

$$f_n \text{ tolerence levels} = \begin{cases} 0.625\% \\ 1.25\% \\ 2.5\% \end{cases}$$

$$\xi_0 \text{ tolerence levels} = \begin{cases} 1.25\% \\ 2.5\% \\ 5.0\% \end{cases}$$

We used normalized RMS, power spectral density, and frequency-wavenumber analysis to quantify these errors.

Figure 35 shows the FK plot of the particle velocity wave field error at different tolerance levels. It is obvious that the error increases at higher tolerance levels. The error is not constant with frequency. Perturbing the natural frequency and damping has high impact at low frequencies and the error decreases at higher frequencies. The highest error occurs at 10 Hz. This validates the result at Figure 33 and Figure 34. We can see that error reaches top at 10 Hz in those simulations as well.

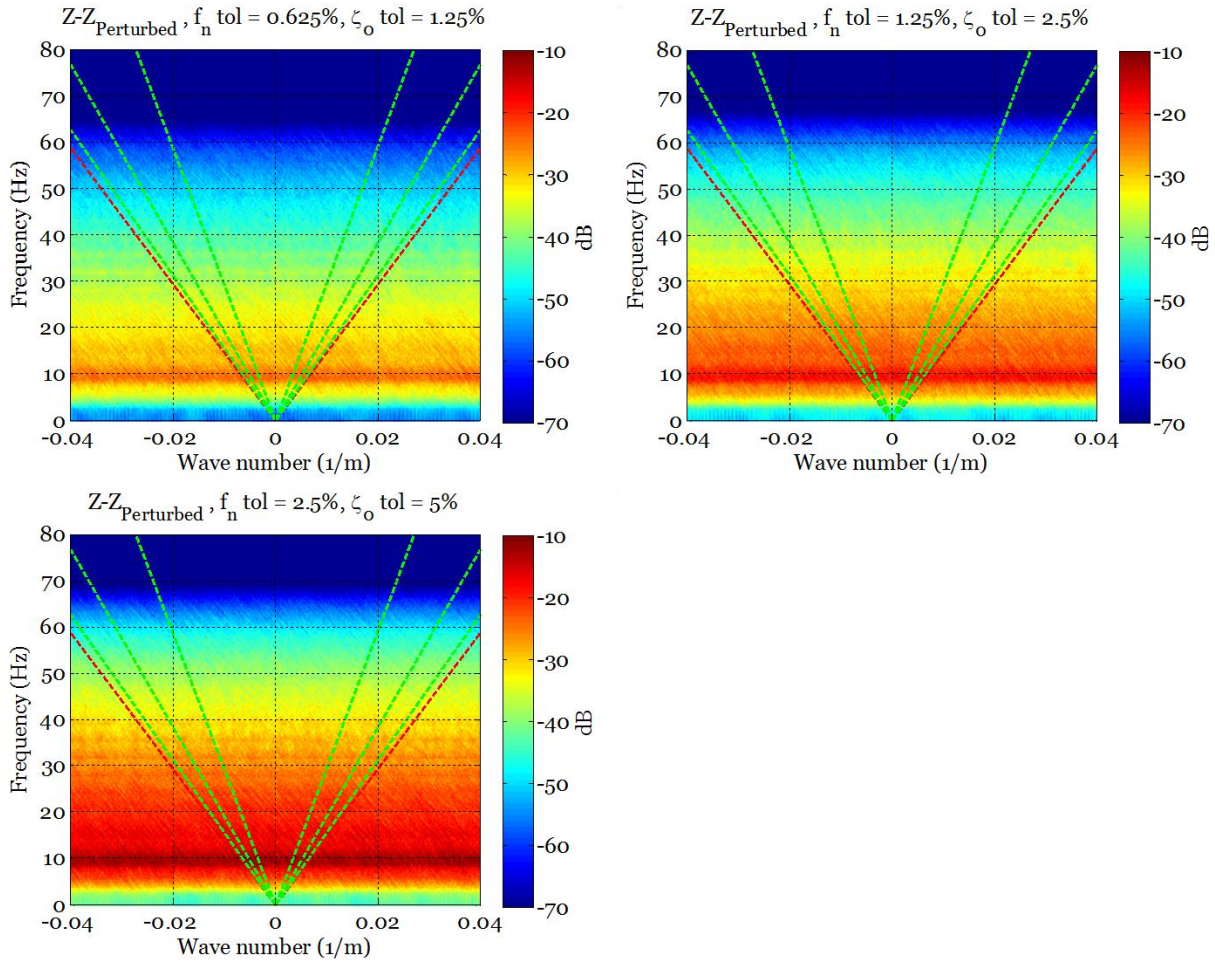

Figure 35: FK Plot of the particle velocity wave field error as a result of change in the natural frequency and damping factor.

In order to compare the signal and noise strength we have looked at the power spectral density of the signal and error. Figures below show the power spectral density of the particle velocity wave field and the error as a result of change in the natural frequency and the damping. We can see from the plots that the error increases with perturbations level increment. There is a narrow gap between the error and the particle velocity wave field at lower frequencies up to around 20-30 Hz at Figure 36. This gap gets bigger at higher frequencies over 30 Hz. This phenomenon can explain the reason why geophones are mostly operated at frequencies higher than 30 Hz.

In Figure 37 we can see that the error is higher due to higher tolerance level of natural frequency and damping factor. The error at frequencies between 10-20 Hz is very close to the particle velocity signal.

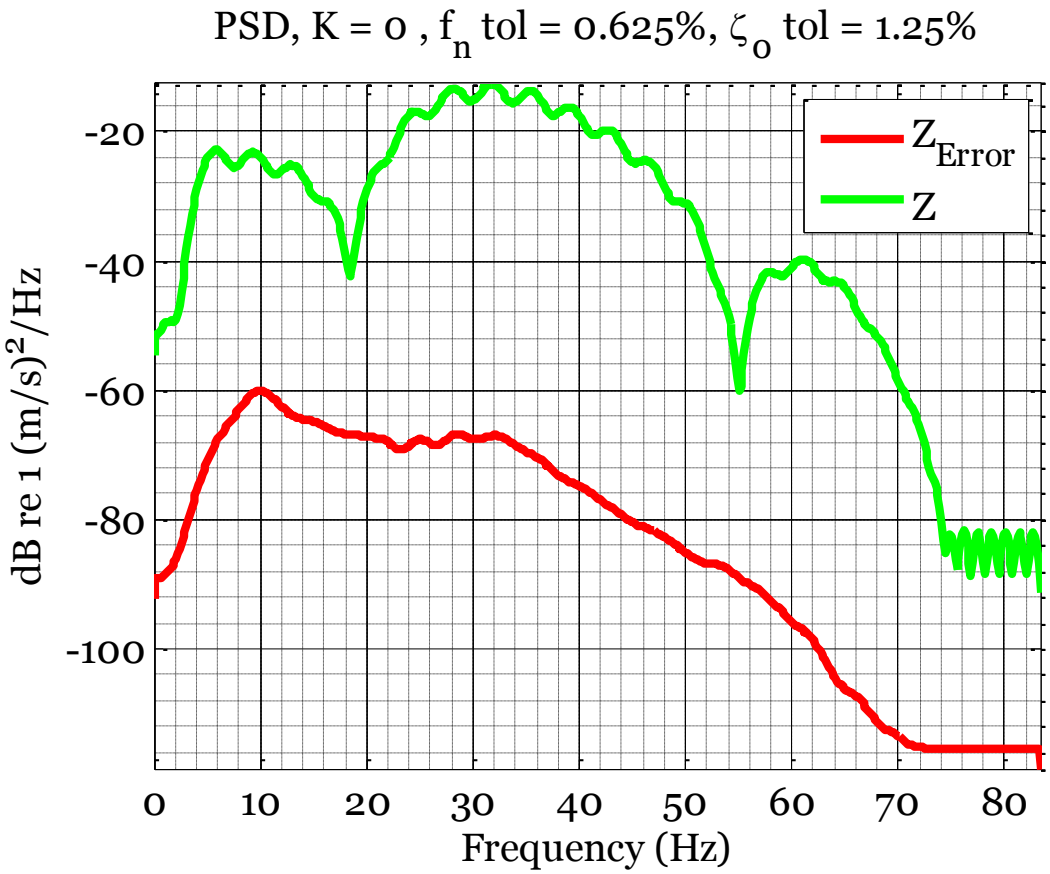

Figure 36: Power spectral density of the particle velocity wave field and the error as a result of change in the natural frequency by 0.625% and damping by 1.25%.

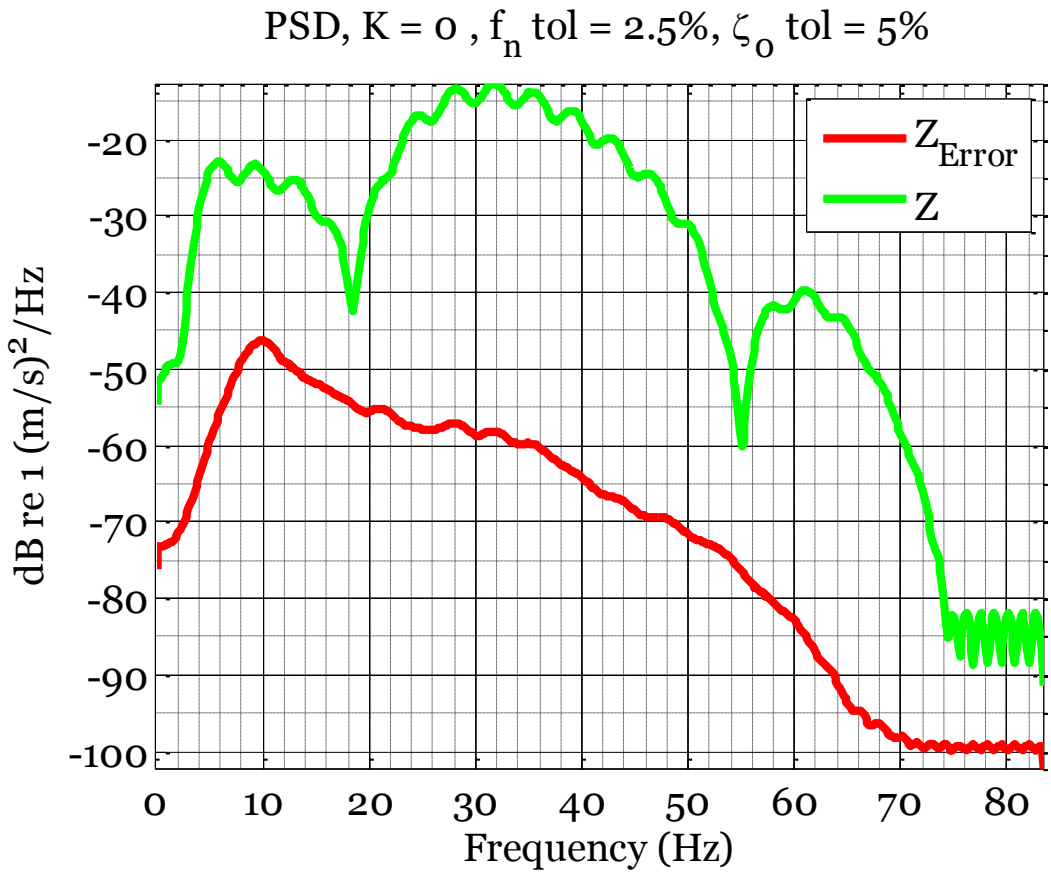

Figure 37: Power spectral density of the particle velocity wave field and the error as a result of change in the natural frequency by 2.5% and damping by 5%.

We have performed group forming on the perturbed particle velocity data in order to analyze the effect of group forming on the error. It is expected that the error degrades since group forming truncates error and enhances the signal to noise ratio.

Figure 38 shows the FK plot of the particle velocity wave field error at different tolerance levels after group forming. The simulations satisfy our expectations and shows that the error reduced after group forming. Comparing the FK plots before (Figure 35) and after group forming (Figure 38), we can see that the error appears in an arch shape (curved) after group forming. It is because the error wave field has been affected by the group forming layout filter. It is evident that the error level has been decreased after group forming.

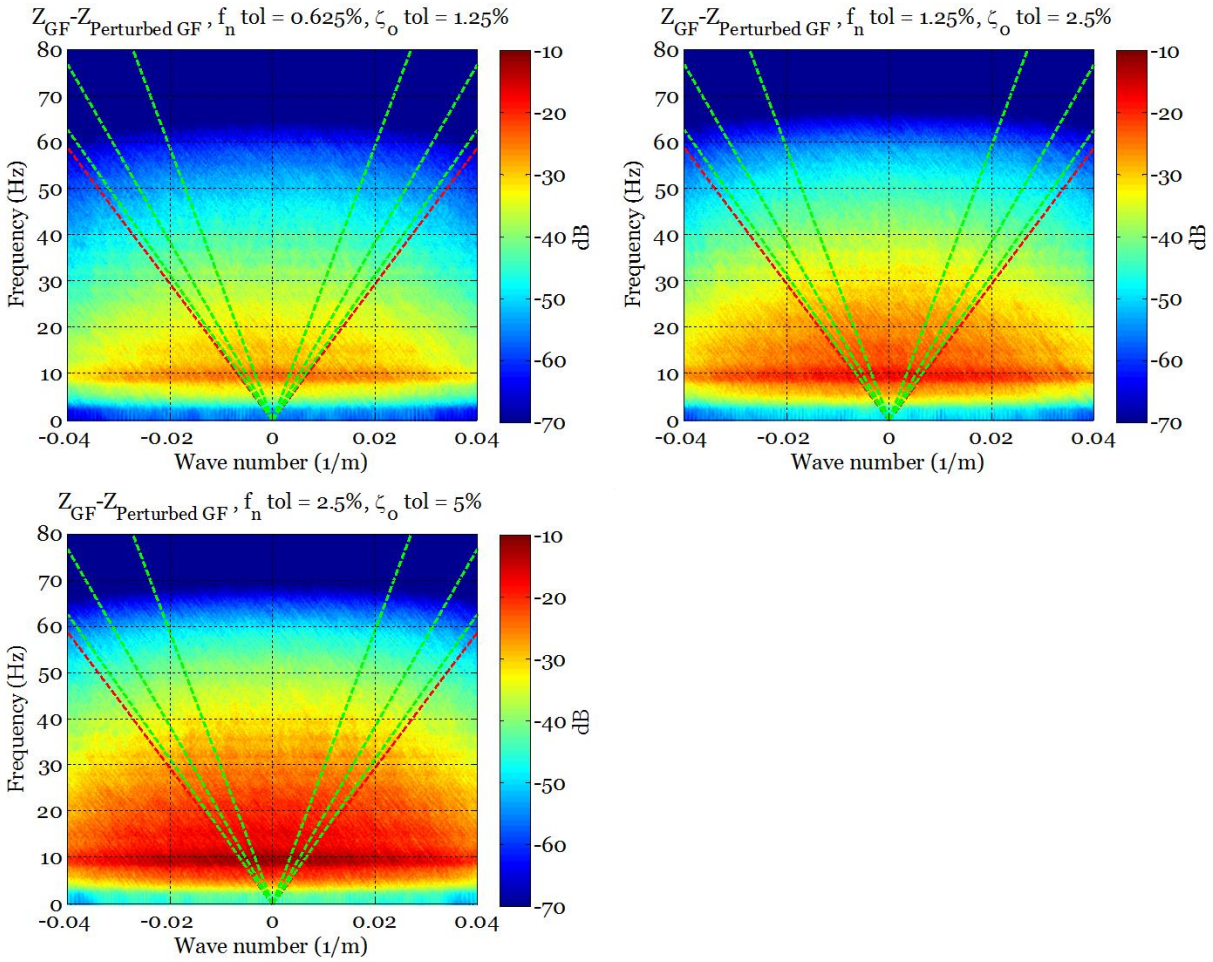

Figure 38: FK Plot of the particle velocity wave field error as a result of change in the natural frequency and damping after group forming.

As described in chapter 3 (Receiver Ghost and its Removal), the acquired up-going wave field data are a much better platform for interpretation of the reservoir characterization. Hence we took one step further and studied the effect of geophone transfer function perturbations on the up-going wave field. We used the perturbed particle velocity data described in chapter 6.1.1.1 to generate the perturbed up-going wave field. The same analysis as for the particle velocity wave field has been done to quantify the error.

Figure 39 shows the FK plot of the up-going wave field error resulted by the perturbed particle velocity wave field at different tolerance levels. We can see from the plots that the error level has been significantly decreased after performing deghosting (PZSUM) on our data compared to the particle velocity wave field level shown in Figure 35.

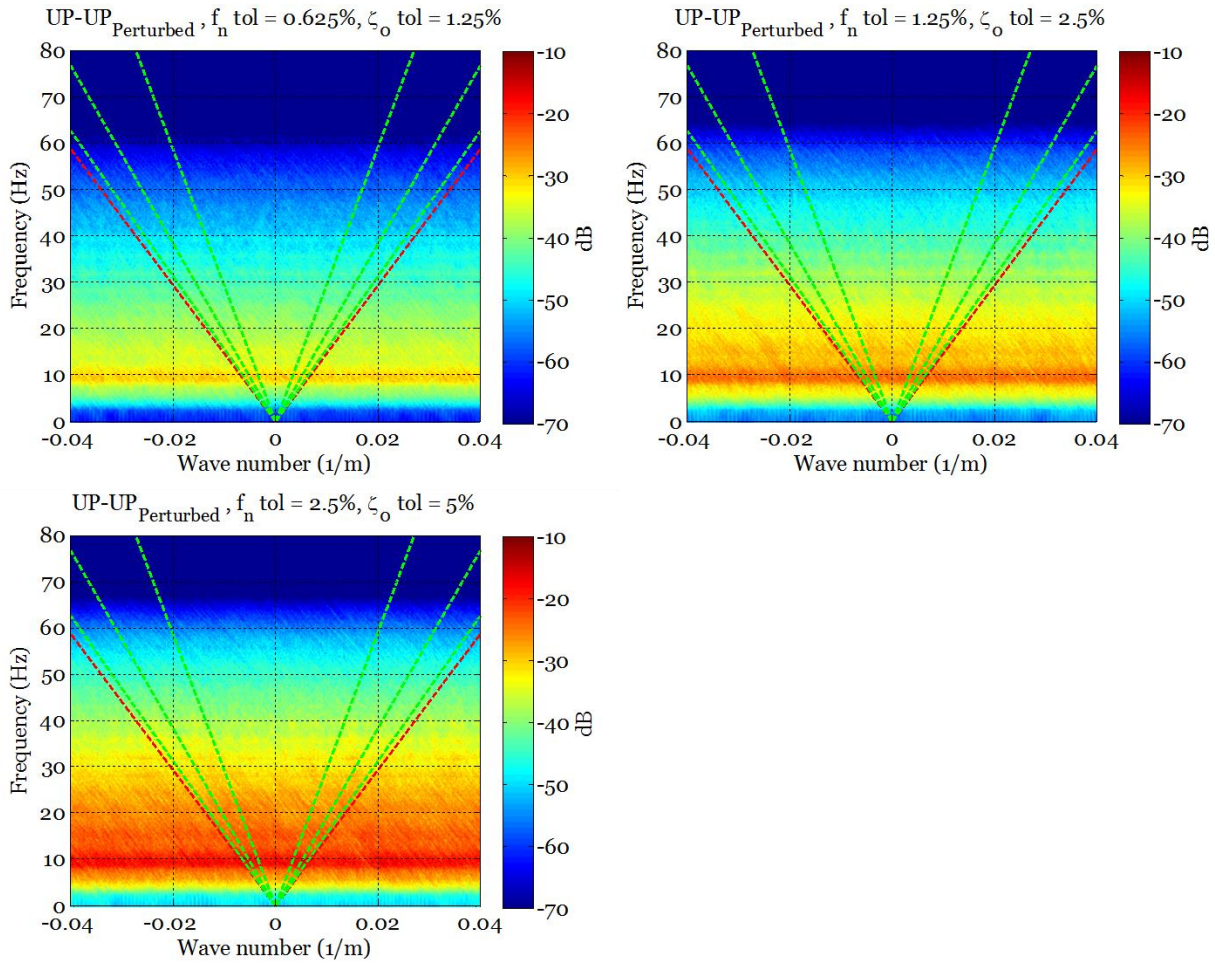

Figure 39: FK Plots of the up-going wave field error resulted by the perturbed particle velocity wave field at different tolerance levels. The perturbation has been made by change in the natural frequency and damping factor level.

Figure 40 shows the power spectral density of the up-going wave field and the error as a result of changes in the natural frequency and the damping factor by 2.5% and 5% respectively. At Figure 37, we have seen that the error level was very close to the particle velocity signal level at the same tolerance levels as here, but we can see from the plot below that error has decreased after performing deghosting such that the gap between the error level and the up-going wave field signal level increased. The error at highest level (≈10 Hz) has been decreased by almost 10 dB compared to the result with the same tolerance level before deghosting.

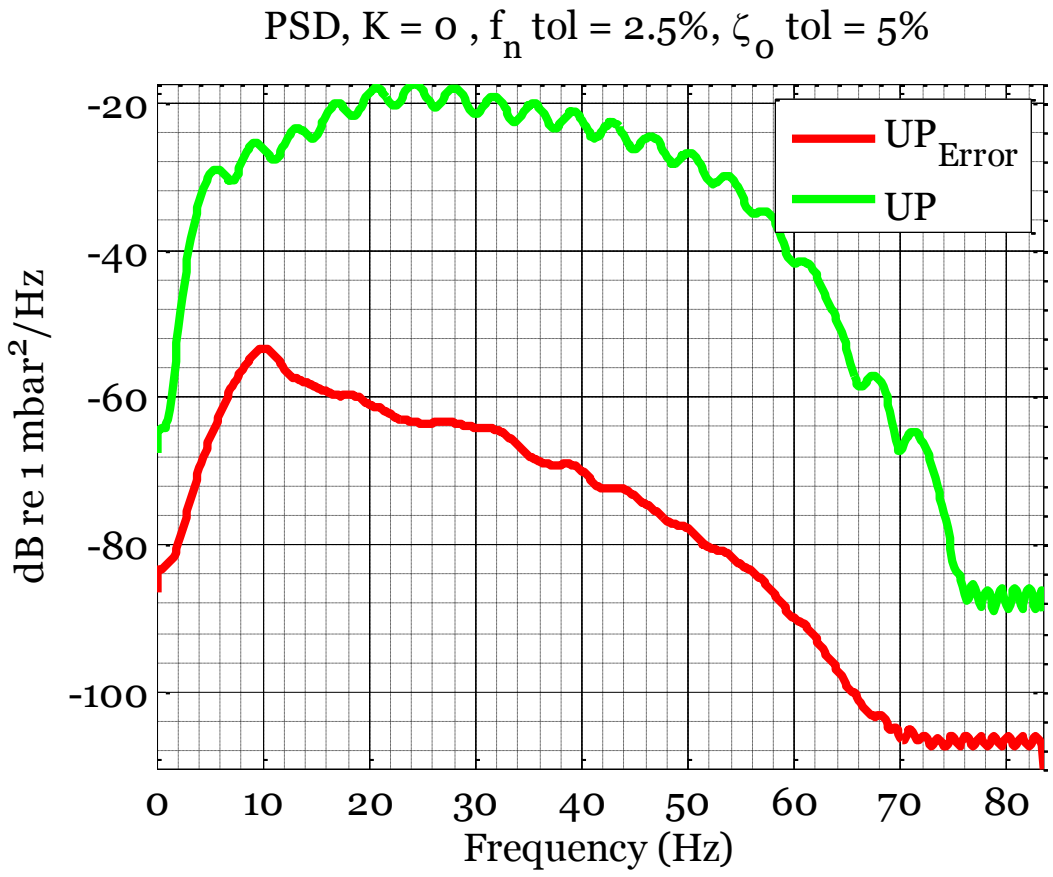

Figure 40: Power spectral density of the up-going wave field and the error resulted by perturbing particle velocity wave field by changing the natural frequency level by 2.5% and damping factor level by 5%.

The next step in our simulation is to perform group forming on the perturbed up-going wave field data in order to analyze how much the error will be reduced and compare the up-going wave field error strength before and after group forming. The approach is the same as before where we have performed group forming on the perturbed particle velocity wave field data. The simulations in this part confirm the fact that group forming attenuates error and increases the signal to noise ratio. We can see a slight decrease in the error level after group forming.

Figures below show the FK plot of the error in the particle velocity and up-going wave field as a result of change in the natural frequency by +2.5% and damping by +5% before and after group forming. Figures on top show the particle velocity wave field error before (left) and after (right) group forming. Figures on bottom show the up-going wave field error before (left) and after (right) group forming. We can see a significant reduction in the error level after deghosting.

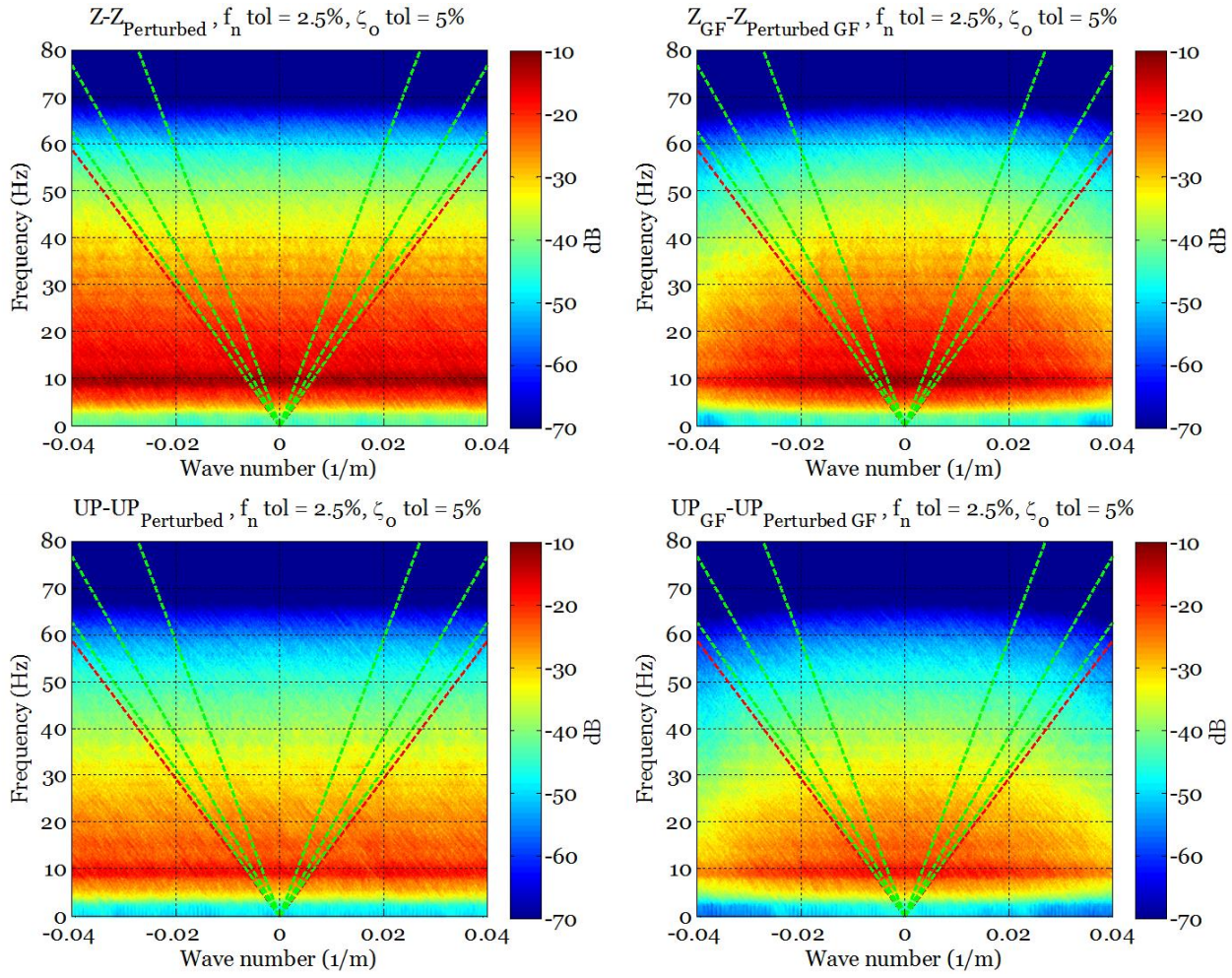

Figure 41: FK plot of the error in the particle velocity (Top) and up-going (Bottom) wave field before (Left) and after (Right) group forming. The error has been generated perturbing the particle velocity wave field by a change in the natural frequency of 2.5% and damping of 5%.

Figure 42 Show the FK-Slice of the error in the particle velocity (top) and up-going (bottom) wave field before (left) and after (right) group forming at different angles. FK-Slice plot of the particle velocity wave field error (top left) shows that error level does not change at different angles since it has the same error value for the same frequency at different angles (different apparent velocity). We can see the same event in the FK-Slice plot of the up-going wave field error (bottom left) that error does not differentiate at different angles. Looking at the figures after performing group forming (right plots); we can see that the error changes at different steering angles. It is higher at higher steering angles (higher velocities).

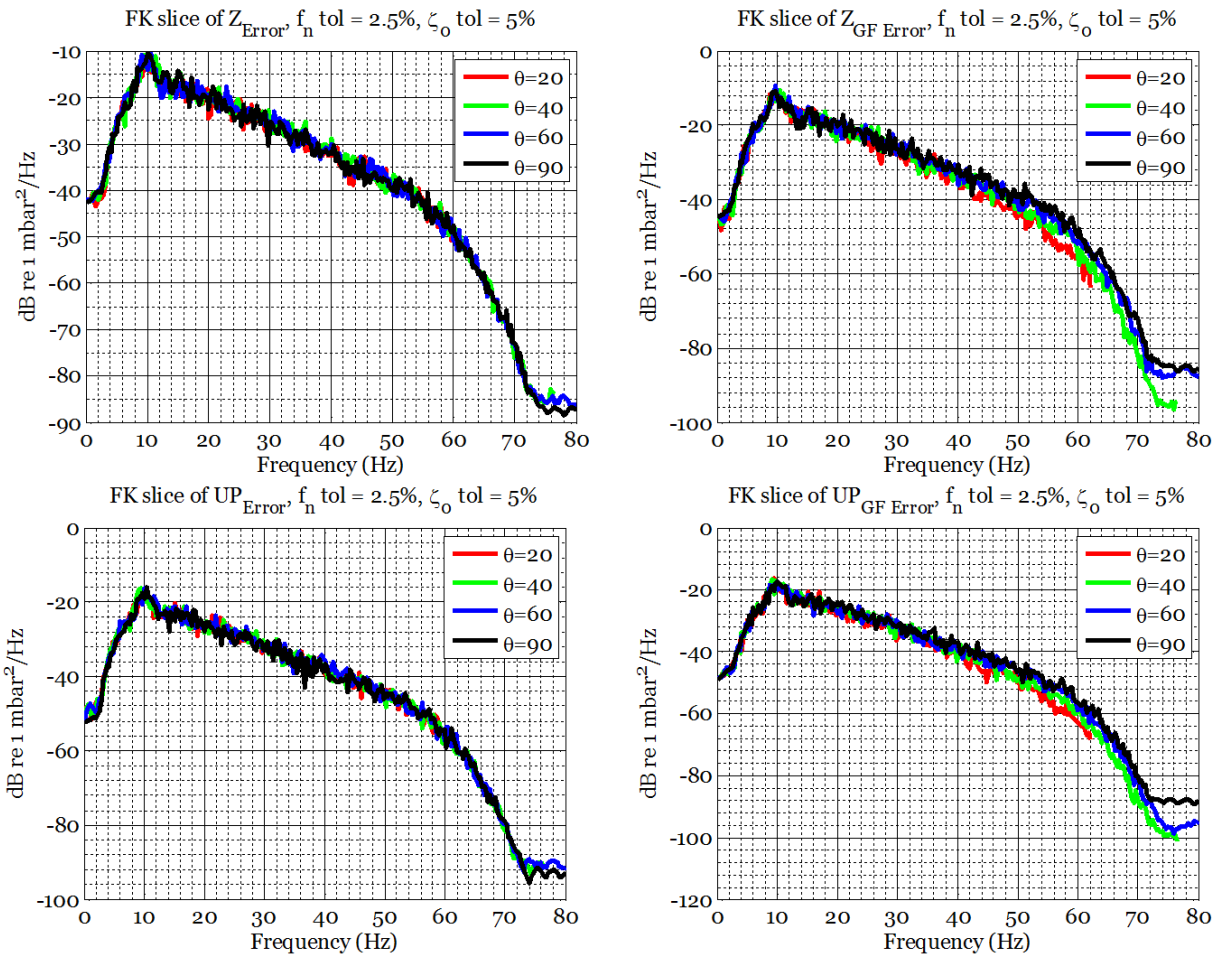

Figure 42: FK-Slice plot of the error in the particle velocity (top) and up-going (bottom) wave field before (left) and after (right) group forming at different angles.

In order to quantify the impact of changes in the natural frequency and damping factor and to be able to compare impact of one perturbation relative to another perturbation, we have looked at the normalized RMS of the error resulted by these perturbations in 2D plots.

Figures below show the averaged normalized RMS of the error in 2D plots at different natural frequency and damping factor tolerance levels along the vertical and horizontal axis respectively. The plots on top show the NRMS of the error in the particle velocity wave field before (left) and after (right) group forming. The NRMS of the error in the up-going wave field has been shown in the bottom. We can see from the NRMS plots that the error increases by the natural frequency and damping tolerance level increment. The error is dominated by the natural frequency error. There is a slight reduction in error level after group forming, whereas the reduction in the error level is more significant after deghosting.

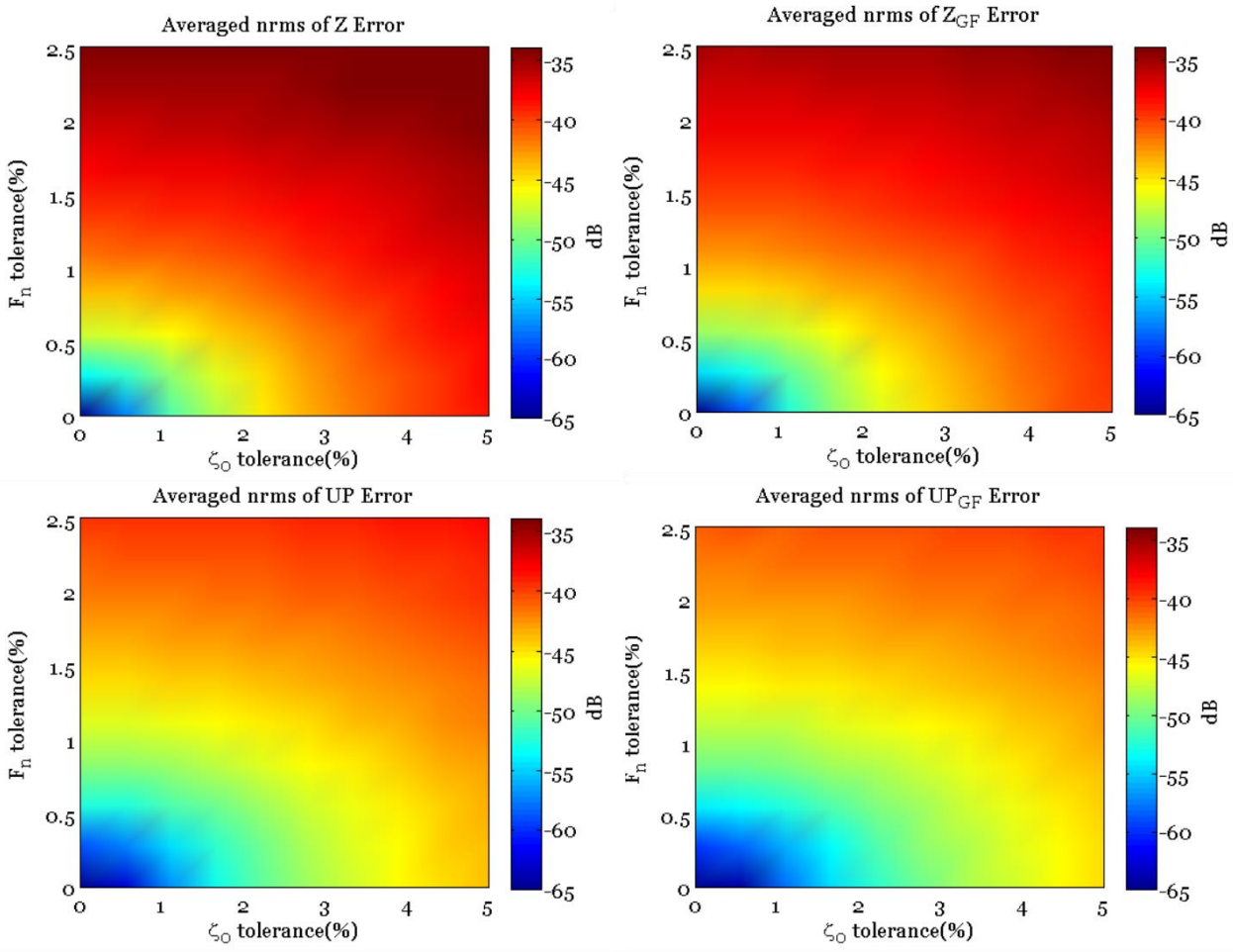

Figure 43: 2D plot of the averaged normalized RMS of the error in the particle velocity (top) and up-going (bottom) wave field before (left) and after (right) group forming. The natural frequency and damping factor tolerance levels vary along the vertical and horizontal axis. The tolerance levels are in percentage.

6.2 Self noise

In this section we will introduce the two types of noise associated with geophone velocity sensors: The Johnson thermal noise (Barry, Lee, and Messerschmitt, 2004) in the circuitry and the noise due to Brownian motion of the suspended mass (Stienstra, Badger, and Maxwell, 1993). We have decided to analyze the seismic data and these noises after the sensor.

6.2.1 Brownian motion

Brownian motion is the random motion of the particles when a small mass is suspended in a fluid or gas (Brownian motion. (2014, February 10), http://en.wikipedia.org/wiki/Brownian_motion).

(Stienstra et al., 1993) gives expression for noise due to Brownian motion of the suspended Geophone velocity sensors. They have derived that the Brownian motion of the mass results in noise in the velocity domain with power spectral density given by:

$$H(\omega) = \frac{1}{\omega^2}\left(4KT\frac{2\zeta_0\omega_n}{m}\right), \tag{31}$$

where ζ_0 is the damping factor; ω_n is the natural angular frequency; K Boltzmann's constant and m is the mass of the sensor.

The power spectral density of the resulted noise upon output of the velocity geophone sensor is given by:

$$H_G(\omega) = \frac{1}{\omega^2}\left(4KT\frac{2\zeta_0\omega_n}{m}\right)|G(\omega)|^2, \tag{32}$$

Figure 44 shows the power spectra of the noise due to the Brownian motion for a SM24 geophone. We can see from the plot that the highest noise level occurs at 10 Hz which complies with the geophone response shown in Figure 32.

6.2.2 Thermal noise

Johnson noise or thermal noise is the unavoidable electronic noise which is generated by random thermal motion of charge carriers in a conductor. We have an efficient resistance of R inside all electronic devices including the velocity geophone. The resistor inside a geophone might be a combination of the coil and shunt resistance. The RMS voltage due to thermal noise of a resistor R is given by:

$$v_{n} = \sqrt{4K_BTR_{coil}\Delta f}, \tag{33}$$

where K_B is the Boltzmann's constant; T is the temperature in Kelvin and R_{coil} is the coil resistance.

(Stienstra et al., 1993) has given the power spectral density of the thermal noise the following expression:

$$H_G(\omega) = 4K_BTR_{coil}, \tag{34}$$

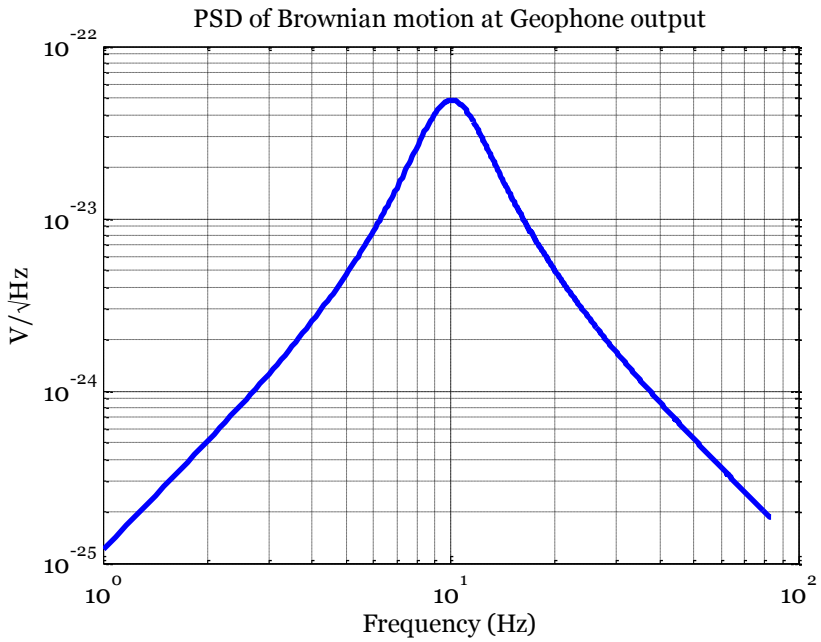

Figure 44: Power Spectral density of the noise due to Brownian motion at the geophone output for a shunted SM24 at 25° C.

As described above, we have decided to study and quantize the effect of these two types of noise on the seismic data after the geophone output. Hence we applied the same matching filter defined in chapter 6.1.1.1 on the noise due to the Brownian motion. We have varied the natural frequency level and damping factor by 2.5% and 5% respectively and studied the effect of it on the resulting noise due to Brownian motion. Thermal noise is not frequency dependent, thus we have not performed any filtering on the thermal noise. These noises have been added to the synthetic particle velocity data the way described in chapter 4 in order to quantify the error level. Since the synthetic data has been well sampled, we have interpolated the data 50 (i.e. data has been up-sampled to 25 cm from 12.5 m) before adding the perturbations. The perturbed data has been groupformed afterward. We then have studied the perturbed data both before and after deghosting.

Figure 45 shows the FK plot of the particle velocity wave field error due to the Brownian motion and thermal noise. The natural frequency and damping factor has been varied by 2.5% and 5% respectively while matching filtering the noise generated by the Brownian motion. This is because we have chosen to look at the result after the geophone output. We can see from the plot that the error has a random shape decreasing with frequency increment. The error does not differentiate at different angles.

Figure 46 shows the power spectral density of the particle velocity wave field and the error due to the Brownian motion and thermal noise. The plot shows that the error has higher level at frequencies below 8 Hz and decreases continuously. The error level remains almost constant at around -230 dB at frequencies higher than 10 Hz. As the result shows, we can conclude that the error resulted by self-noise has very low impact on the data.

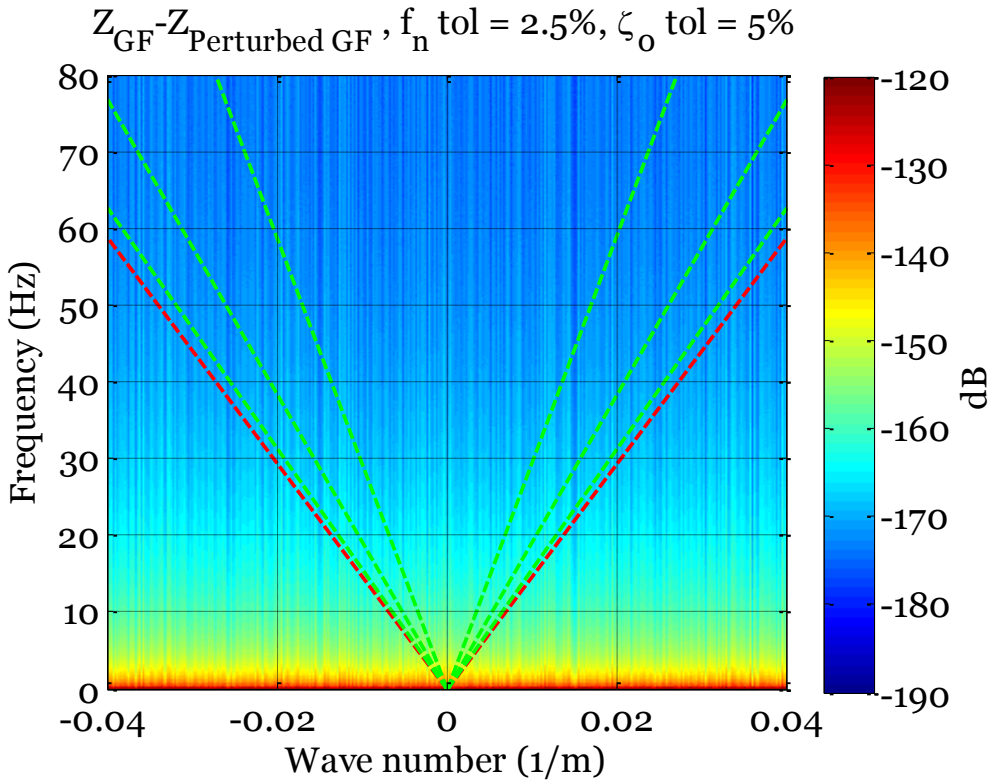

Figure 45: FK Plot of the particle velocity wave field error due to the Brownian motion and thermal noise. The natural frequency and damping factor tolerance levels are 2.5% and 5% respectively.

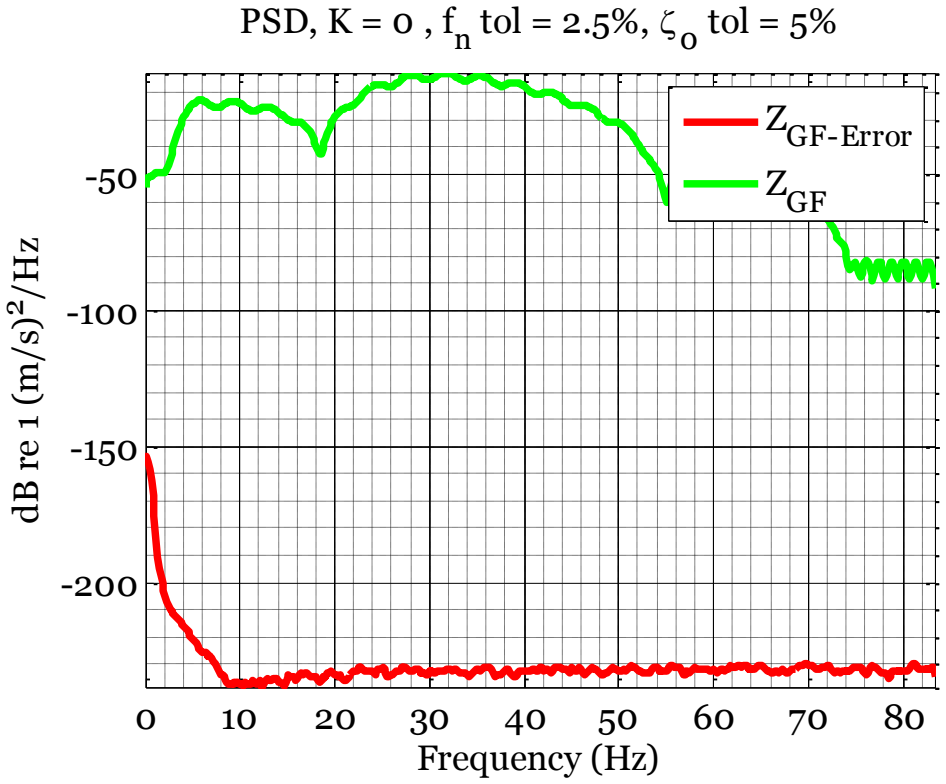

Figure 46: Power spectral density of the particle velocity wave field and the error due to the Brownian motion and thermal noise. The natural frequency and damping factor tolerance levels are 2.5% and 5% respectively.

Figure 47 shows the FK plot of the up-going wave field error due to the Brownian motion and thermal noise. The natural frequency and damping factor has been varied by 2.5% and 5% respectively while matching filtering the noise generated by the Brownian motion. We can see that the error level has been decreased slightly after performing deghosting on our data (PZSUM) compared to the particle velocity wave field error shown in Figure 45.

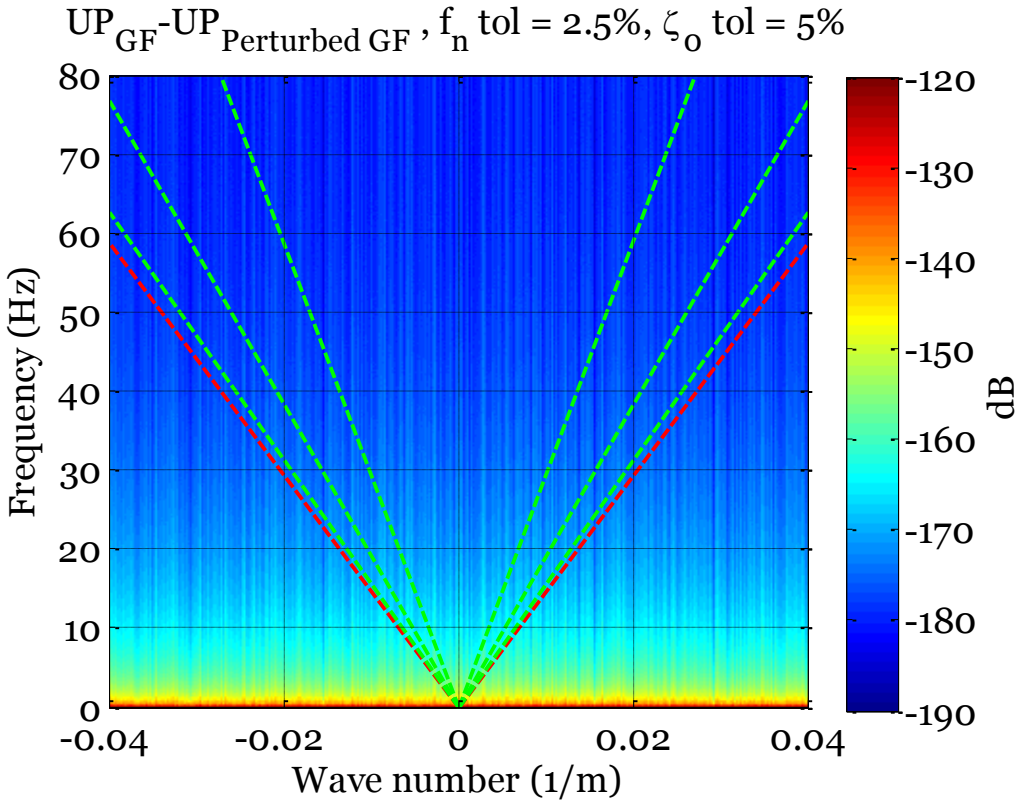

Figure 47: FK Plot of the up-going wave field error due to the Brownian motion and thermal noise. The natural frequency and damping factor tolerance levels are 2.5% and 5% respectively.

Figure 48 shows the power spectral density of up-going wave field and the error due to the Brownian motion and thermal noise. We can see that the error level has been decreased by almost 10 dB at all frequencies compared to the error level of the particle velocity wave field before performing deghosting (shown in Figure 46).

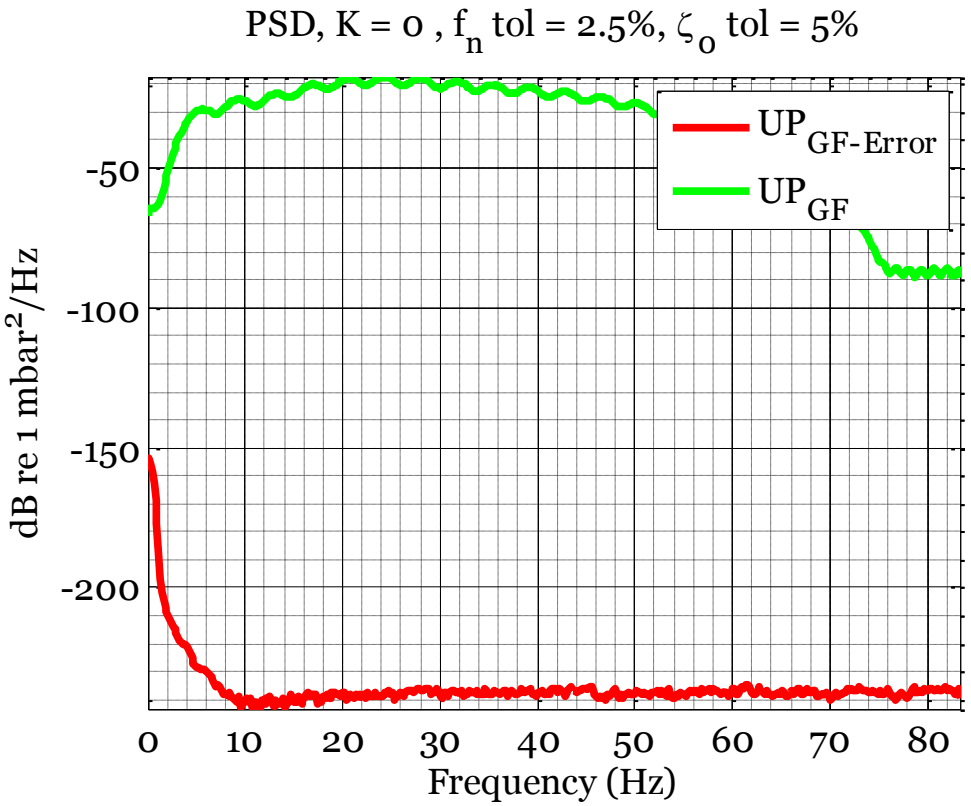

Figure 48: Power spectral density of the up-going wave field and the error due to the Brownian motion and thermal noise. The natural frequency and damping factor tolerance levels are 2.5% and 5% respectively.

In order to study the impact of the change in the natural frequency and damping factor tolerance level on the self-noise, we have plotted the averaged normalized RMS of the error in a 2D plot. Figure 49 shows the averaged normalized RMS of the groupformed particle velocity data error at different natural frequency and damping tolerance levels along the horizontal and vertical axis. The plot shows that the error has a very small variation and is about -143 dB. The natural frequency and damping factor increment does not uniformly affect the error level. We can conclude that self-noise level does not depend on these two factors. The self-noise level is well below the seismic signal level gathered by geophone sensors that it does not have any effect on data quality.

Figure 50 shows the averaged normalized RMS of the groupformed up-going wave field error due to self-noise applied to particle velocity wave field. The error level has decreased by almost 5 dB after performing deghosting.

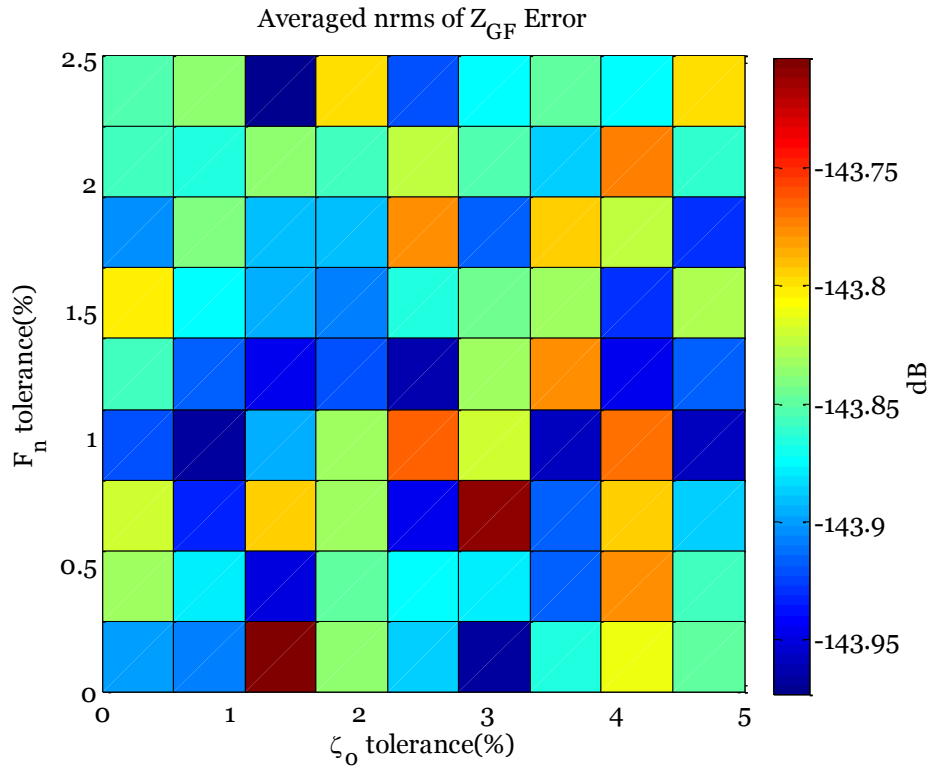

Figure 49: 2D plot of the averaged normalized RMS of the error in the particle velocity wave field after group forming. The natural frequency and damping tolerance level vary along the vertical and horizontal axis in percentage.

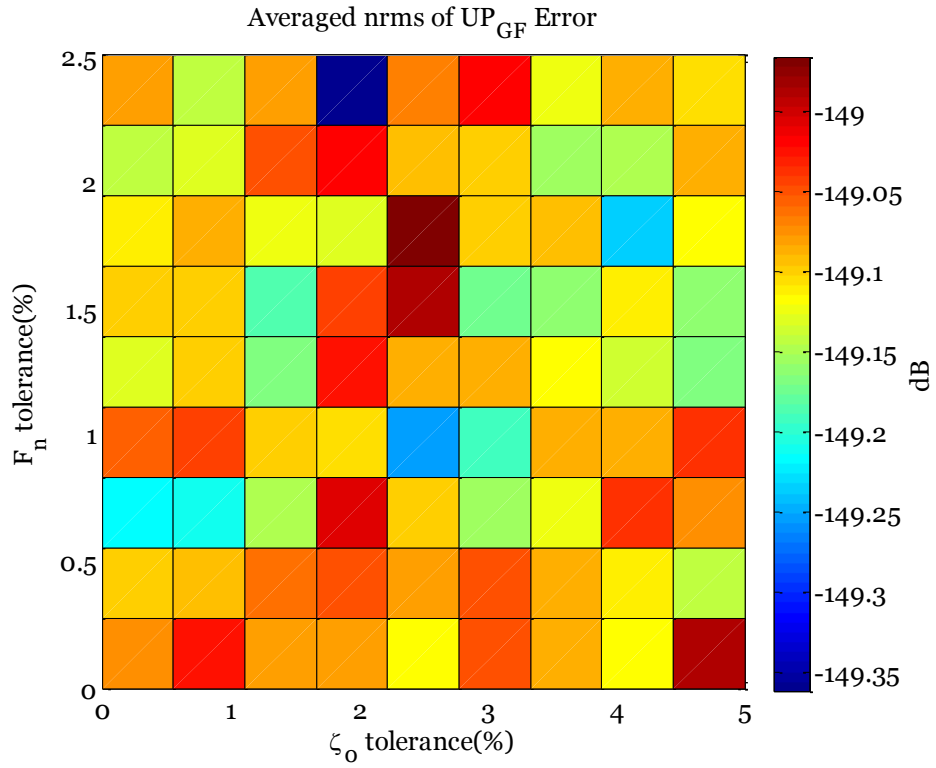

Figure 50: 2D plot of the averaged normalized RMS of the error in the up-going wave field after group forming. The natural frequency and damping tolerance level vary along the vertical and horizontal axis in percentage.

6.3 Position error

6.3.1 Horizontal positions

As mentioned in Chapter 5, the response from a group of individual sensors is summed to a single output for the purpose of higher signal to noise ratio. The group centers are normally surveyed with sub-cm accuracy. The error in position is solely caused by human error. Sensor positions along the streamer are not normally inspected. Sensor position error is caused by the layout crew's inaccuracy when manual mounting sensors along the streamer.

In this chapter we will first evaluate the impact of position errors on the array response using theoretical model. Later we will study the impact of position errors on the synthetic seismic data.

We assume a 1 dimensional array consisting of 25 sensors uniformly located on the x-axis with a sensor spacing of 1m. We also assume that the position errors are uncorrelated from sensor to sensor with an RMS of 33cm. Figure 51 shows the response for this array (in red) and the response of the position perturbed array with an RMS of 33 cm (in blue). We can see from the plot that the array loses some of its coherent noise suppression abilities for higher wavenumbers, but the array response is largely unaltered around the first side lobe.

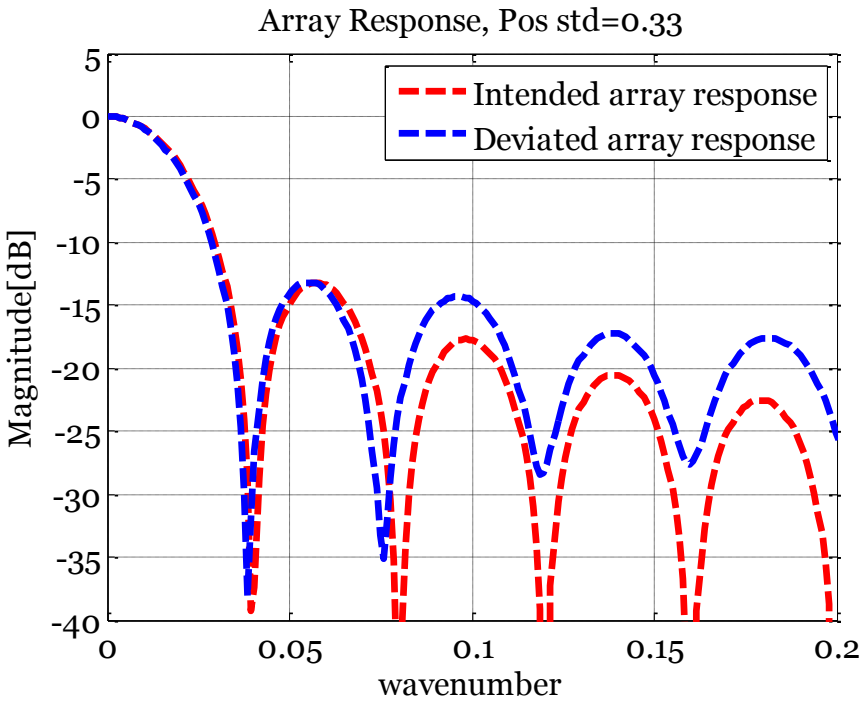

Figure 51: Response for an array with 25 sensors located on the x-axis with 1m spacing. The position errors are random with an RMS of 33cm. The intended, and deviated or perturbed array response are shown in red and blue respectively.

Now we are going to analyze the impact of position error on the synthetic seismic data. We apply uncorrelated position error on the pressure and particle velocity data and study its impact on these wave fields and generated up-going wave field. We use normalized RMS, power spectral density, and frequency-wavenumber analysis to quantify these errors.

6.3.1.1 Position error and its impact on pressure data

In this section we will look at the impact of position error on the pressure wave field. We have perturbed the pressure wave field by first resampling it to a denser grid and then interpolating to perturbed hydrophone sensor positions along the streamer. We have chosen five levels of position standard deviations which are as follow:

$$\text{Position error std} = \begin{cases} 0.01\% \\ 0.025\% \\ 0.05\% \\ 0.10\% \\ 0.20\% \end{cases}$$

Or in RMS [cm]:

$$\text{Position error RMS} = \begin{cases} 1.0cm \\ 2.5cm \\ 5.0cm \\ 10cm \\ 20cm \end{cases}$$

Position errors are assumed uncorrelated from hydrophone to hydrophone. The perturbed data was then groupformed and down-sampled to the initial grid.

Figure 52 shows the FK plot of the pressure wave field error due to position error at different standard deviation levels after group forming. As we can see from the plots, the error increases together with perturbation level increment. The error varies at different frequencies, highest between 30-40 Hz.

Figure 53 shows the FK-slice of the error in the pressure wave field generated by applying position error with an RMS of 20 cm at different steering angles after group forming. The plot shows that error does not differentiate at different steering angles.

Figure 54 shows the power spectral density of the pressure wave field and the error resulted by applying position error with an RMS of 20 cm. The error attains its maximum, i.e. -60 dB at 30 Hz.

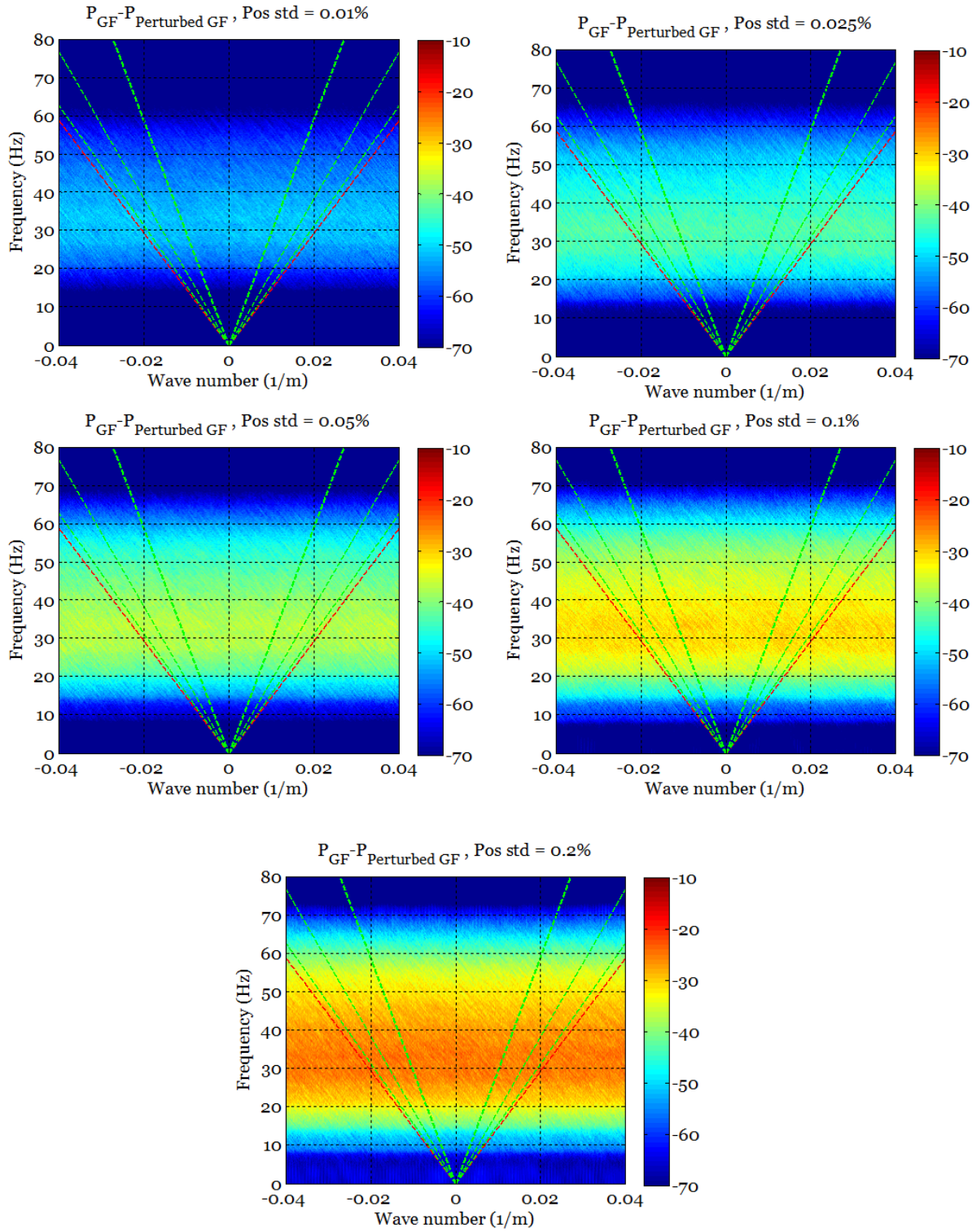

Figure 52: FK plot of the pressure wave field error after group forming resulted by applying position error at different standard deviation levels.

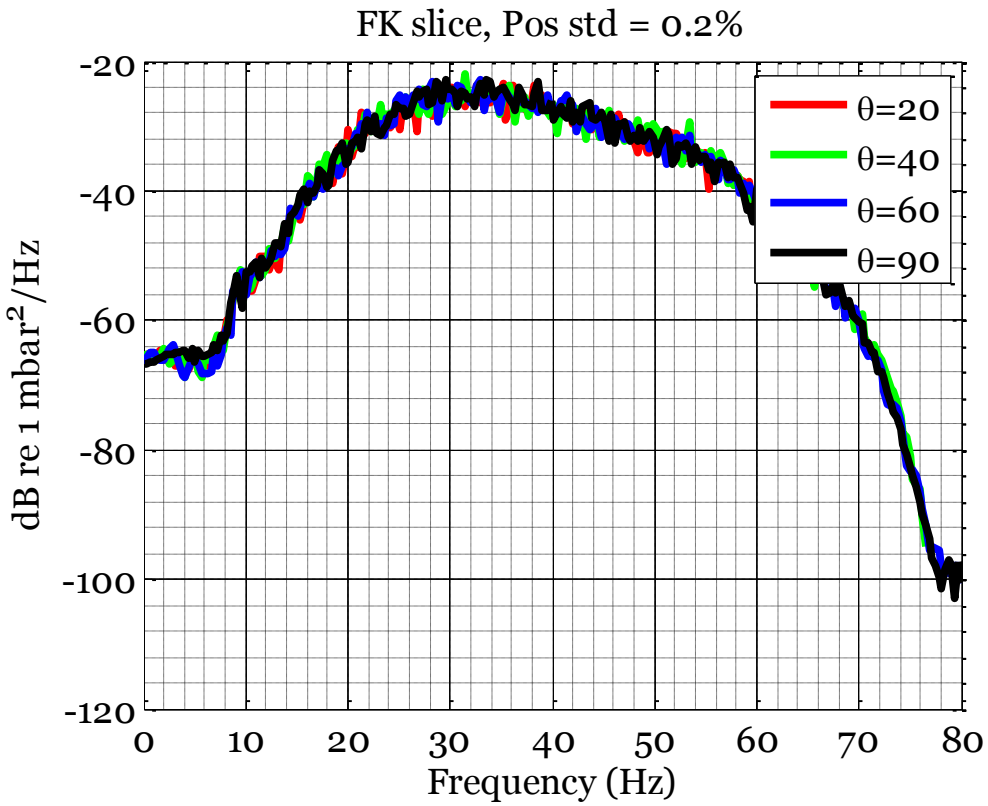

Figure 53: FK slice of the error in the pressure wave field resulted by applying position error with an RMS of 20cm after group forming at different steering angles.

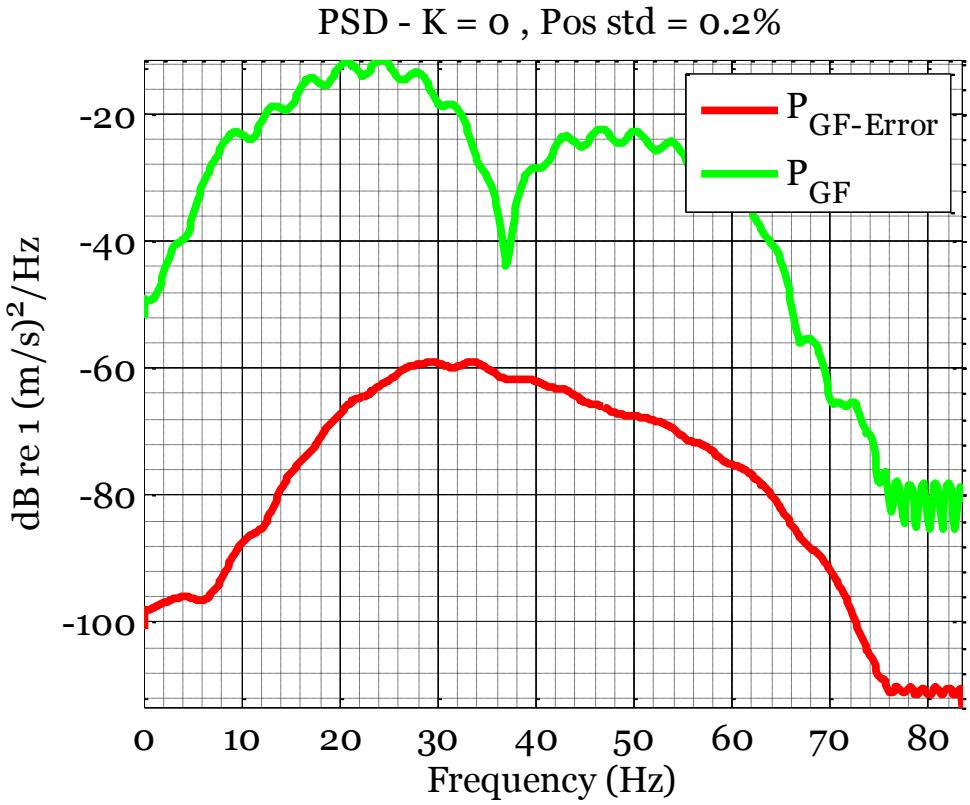

Figure 54: Power spectral density of the pressure wave field and the error resulted by applying position error with an RMS of 20cm.

6.3.1.2 Position error and its impact on particle velocity data

In this section we will look at the impact of position error on the particle velocity wave field. Here we have performed the same study on particle velocity wave field as for pressure wave field. Geophone sensor positions were perturbed with the same position standard deviations and data was then interpolated at these positions.

Figure 55 shows the FK plot of the particle velocity wave field error due to position error at different standard deviation levels after group forming. Comparing these plots with the results shown at Figure 52, it is obvious that the same level of position error perturbation has higher impact on the pressure data. The error level in pressure wave field is about 10 dB higher for all perturbation levels compared with particle velocity wave field.

Figure 56 shows the power spectral density of the particle velocity wave field and the error resulted by applying position error with an RMS of 20 cm. The error attains maximum of approximately -70 dB at frequencies between 30-50 Hz

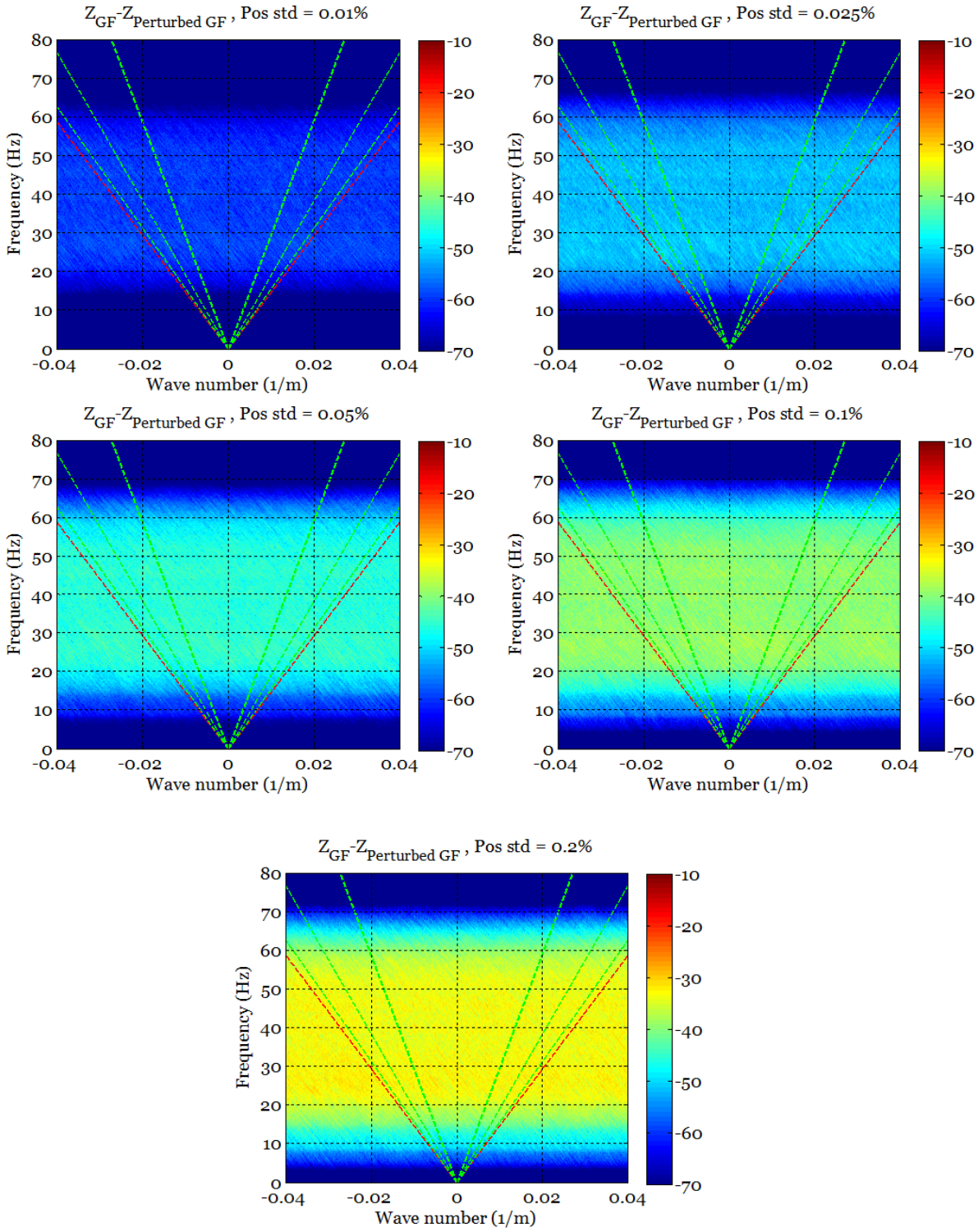

Figure 55: FK plot of the particle velocity wave field error after group forming resulted by applying position error at different standard deviation levels.

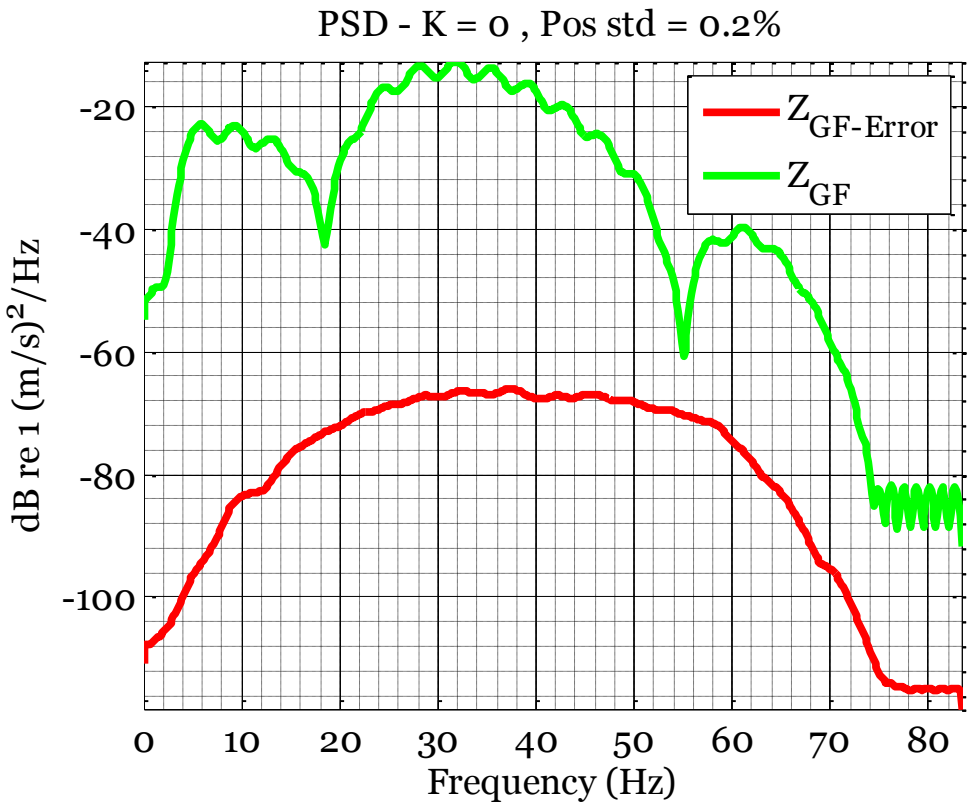

Figure 56: Power spectral density of the particle velocity wave field and the error resulted by applying position error with an RMS of 20 cm.

6.3.1.3 Position error and up-going wave field

In this section we will study the impact of position error on the up-going wave field generated using PZSUM algorithm.

Our analysis included the following three cases:

A. Perturbed up-going wave field resulted by just perturbing the pressure wave field.
B. Perturbed up-going wave field resulted by just perturbing the particle velocity wave field.
C. Perturbed up-going wave field resulted by both perturbing the pressure and particle velocity wave field.

All the cases mentioned above are performed on the groupformed data.

Figure 57, Figure 58 and Figure 59 show the FK plot of the up-going wave field error due to position error for the three cases defined above. Both the pressure and particle velocity sensor positions are perturbed with an RMS of 10 cm (left) and 20 cm (right). The plots show that same level of position error has higher impact on the pressure wave field and the error in up-going wave field is dominated by the error in pressure wave field.

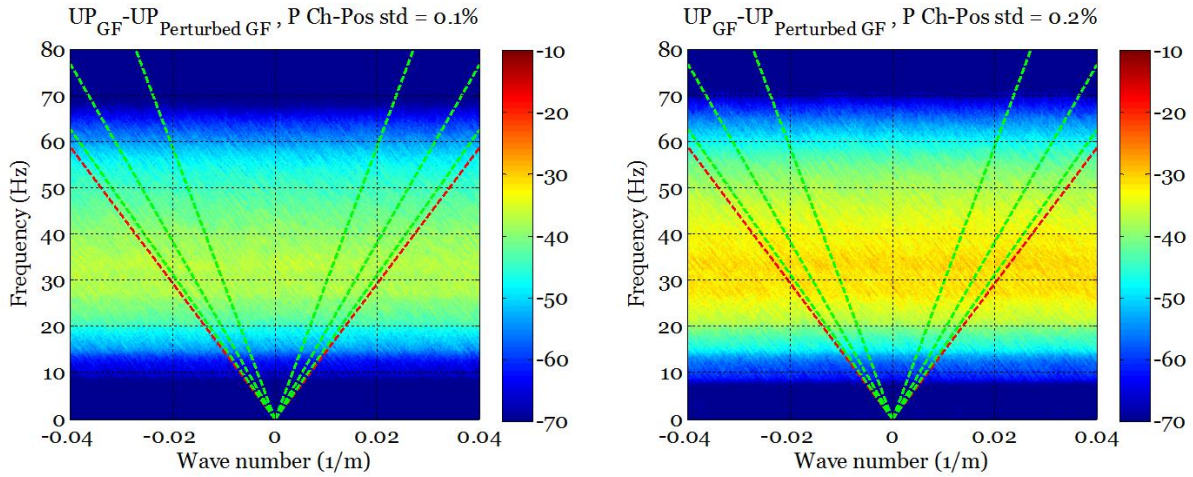

Figure 57: FK plot of the up-going wave field error resulted by applying position error on pressure wave field with an RMS of 10 cm and 20 cm (left and right).

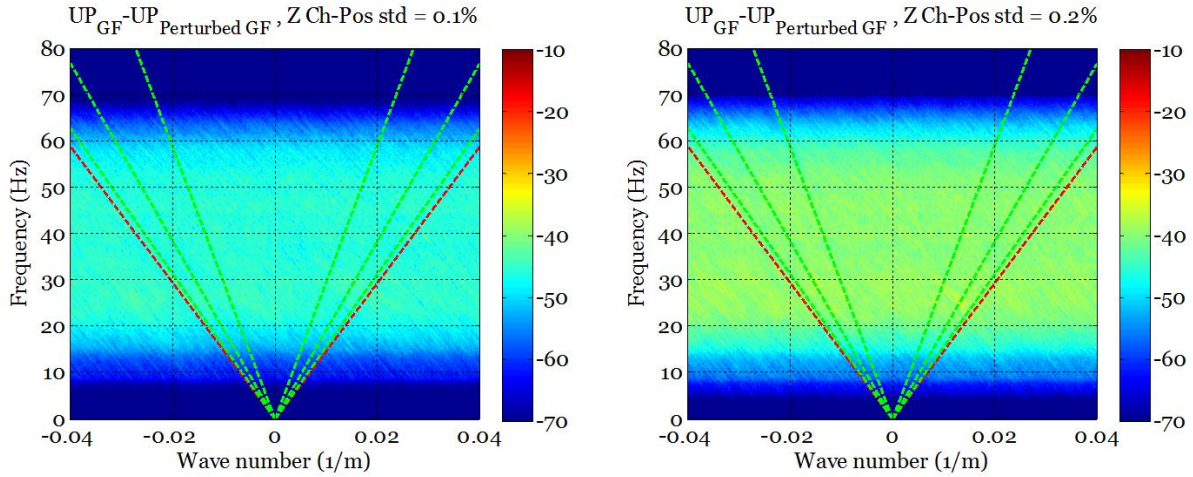

Figure 58: FK plot of the up-going wave field error resulted by applying position error on particle velocity wave field with an RMS of 10 cm and 20 cm (left and right).

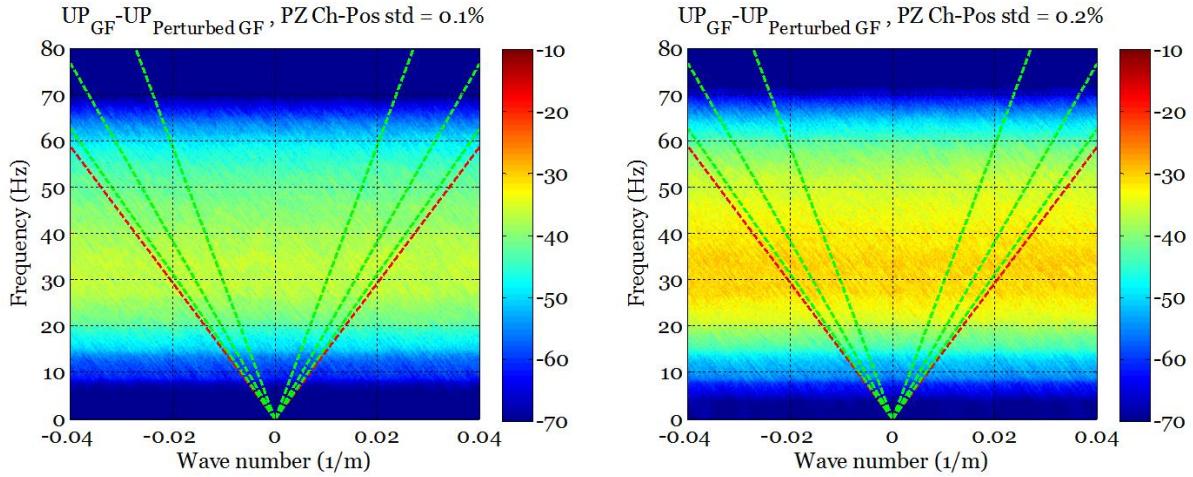

Figure 59: FK plot of the up-going wave field error resulted by applying position error on both pressure and particle velocity wave field with an RMS of 10 cm and 20 cm (left and right).

Figure 60 shows the power spectral density of the up-going wave field and the error due to position error applied on the following wave fields:

A. Pressure wave field (top left).
B. Particle velocity wave field (top right)
C. Both pressure and particle velocity wave field (bottom left).

All position errors has been performed with an RMS of 20 cm. Comparing the result from case A. and C. shows that the total error in up-going wave field is dominated by error in the pressure wave field.

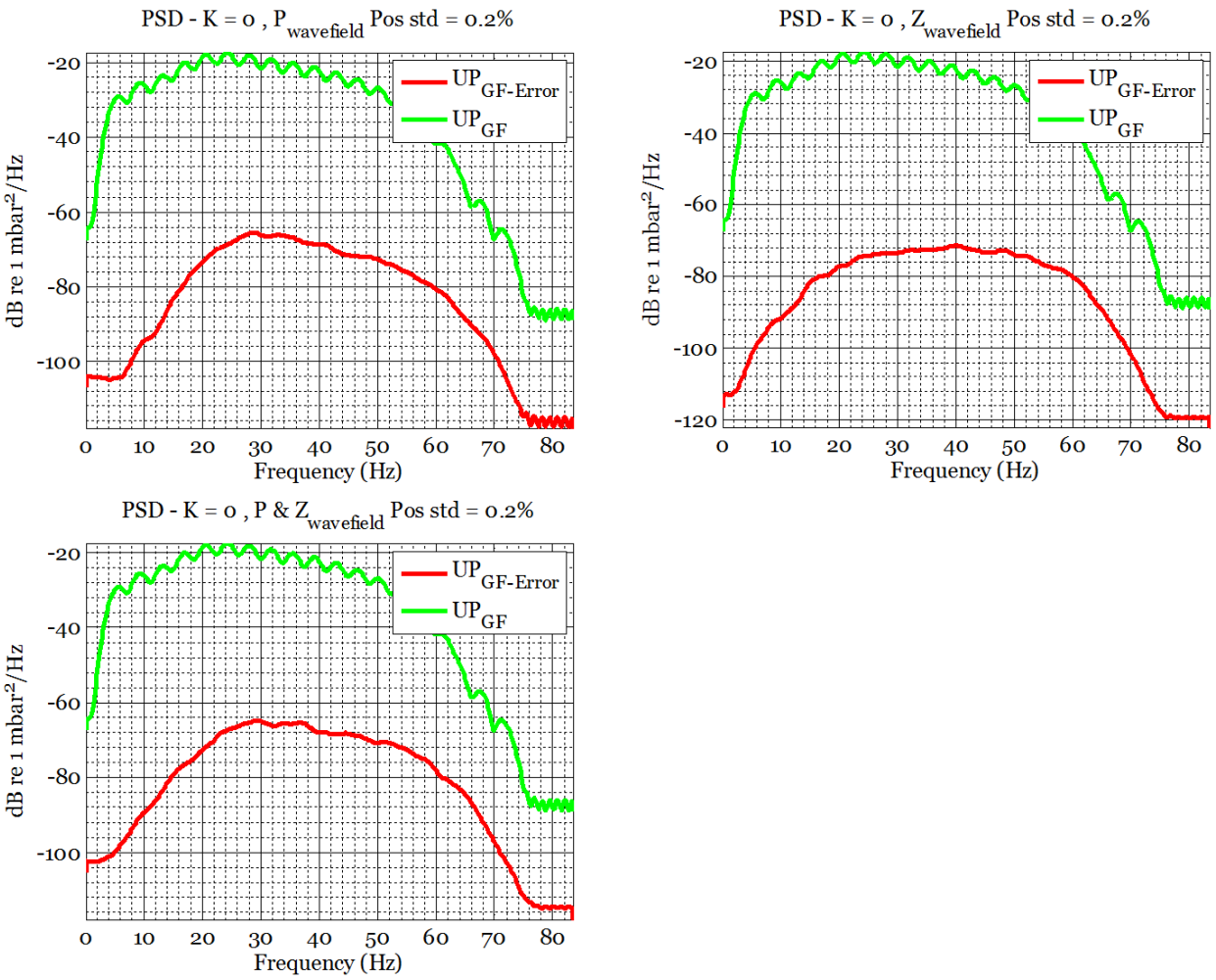

Figure 60: Power spectral density of the up-going wave field and the error resulted by applying position error with an RMS of 20cm on pressure wave field (top left), particle velocity wave field (top right) and both pressure and particle velocity wave field (bottom left).

Figure 61 shows the averaged normalized RMS of the up-going wave field error in a 2D plot at different levels of position error for pressure and particle velocity wave field along the vertical and horizontal axis.

Table 2 lists normalized RMS of the up-going wave field error for the most position perturbed cases shown in the 2D plot below.

$P_{wavefield}$ Pos std (cm)	$Z_{wavefield}$ Pos − std (cm)	$UPGoing_{wavefield}$ error nrms(dB)
0	**20**	**-51.2**
20	**0**	**-46.5**
20	**20**	**-45.2**

Table 2: Normalized RMS of up-going wave field error in [dB] at different levels of position error for pressure and particle velocity wave field.

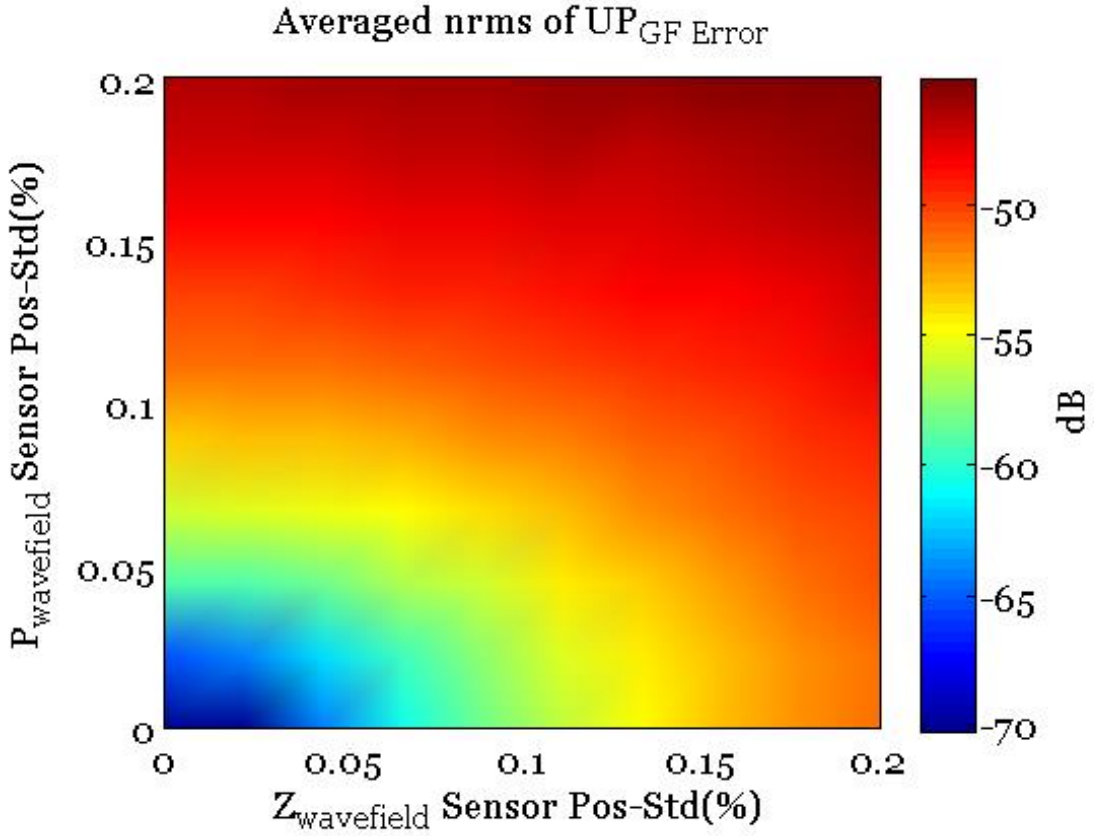

Figure 61: 2D plot of the averaged normalizes RMS of the error in the up-going wave field after group forming. The pressure and particle velocity wave fields are perturbed along vertical and horizontal axis. Position error RMS has been varied from 0-20 cm along each axis.

6.4 Dead channels and polarity reversals

Dead channels and polarity reversal are two kinds of amplitude perturbations. They can take on two values $(0,1)$, respectively $(-1,1)$. Hence, the amplitude perturbations introduced by dead channels and polarity reversal are very large if they enter data processing undetected. In single sensor acquisition (digital group forming) polarity reversals are easy to be fixed once they are detected. This does not apply to analog group forming since the outputs of a group of sensors are combined to a single output. The impact of dead channels on the data can be reduced by removing them or interpolation from neighboring traces in the processing. An example spec may be a maximum of 3% dead channels.

In this chapter we are going to analyze the impact of dead channels and polarity reversals perturbations on the synthetic seismic data. These perturbations are associated with both geophone and hydrophones; hence we apply them on the pressure and particle velocity data and study the impact of these perturbations on the synthetic data before and after PZSUM.

We use normalized RMS, power spectral density, and frequency-wavenumber analysis to quantify these errors.

6.4.1 Dead channels, Polarity reversals and their impact on pressure data

Here we have individually applied dead channels and polarity reversals perturbation to the pressure wave field by killing/reversing the output of random hydrophone channels along the streamer. We have chosen the following three levels of dead/polarity reversed channels:

$$\text{Dead/Polarity rev. channel levels} = \begin{cases} 0.25\% \\ 0.5\% \\ 1.0\% \end{cases}$$

The pressure data was interpolated first, and then dead/polarity reversed channels were chosen randomly in a way they are part of the layout being used in group forming the data. The interpolated perturbed pressure data was then groupformed and down-sampled to the initial grid.

Figure 62 shows the FK plot of the pressure wave field error due to dead channels (left plots) and polarity reversal (right plots) perturbation at different levels after group forming. We observe that the error increases together with perturbation level increment. The error varies at different frequencies. Results indicated that error due to polarity reversal has higher impact on the pressure wave field than the dead channel perturbation.

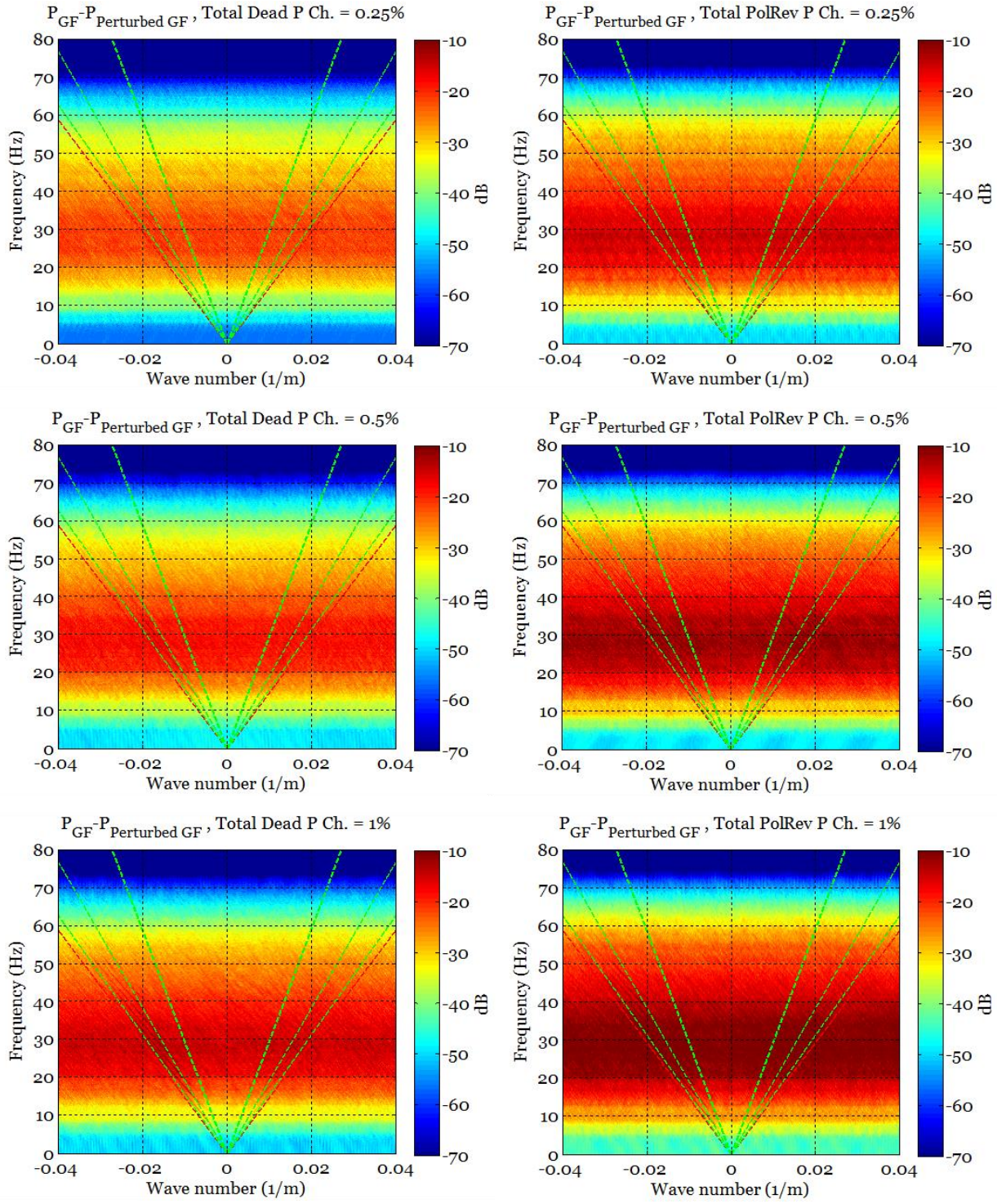

Figure 62: FK plot of the pressure wave field error after group forming resulted by applying dead channel (left) and polarity reversal (right) perturbations at different percentage levels.

Figure 63 shows the FK-slice of the error in pressure wave field due to dead channels (left) and polarity reversals (right) at different steering angles after performing group forming. The error is highest at frequencies between 20-40 Hz. We can see from the plots that the error does not differentiate at different steering angles.

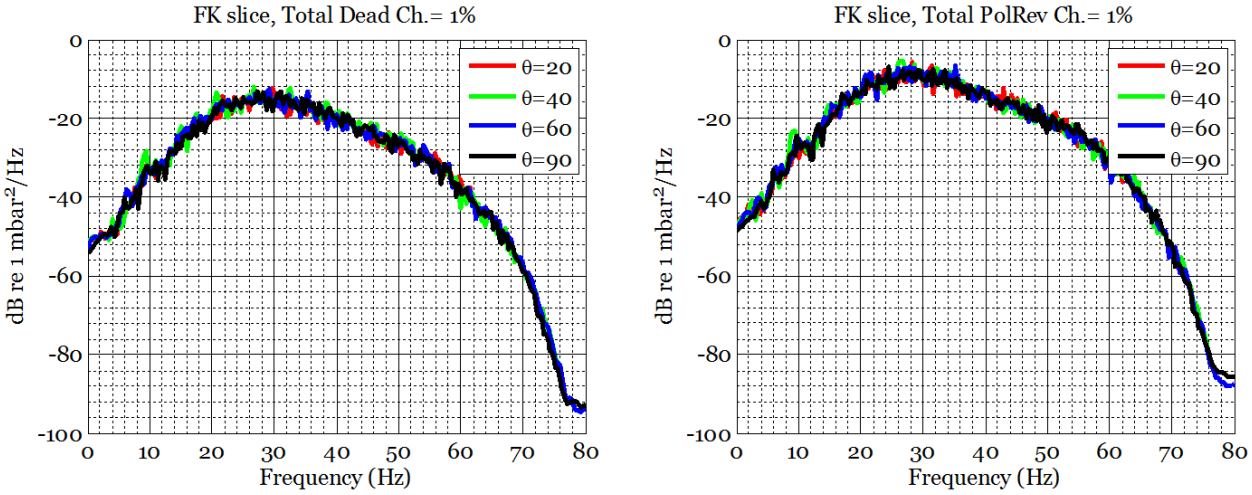

Figure 63: FK slice of the pressure wave field error due to dead channels (left) and polarity reversal (right) at different steering angles. Standard deviation of the error is 1%.

Figure 64 shows the power spectral density of the pressure wave field and the error due to dead channels (left) and polarity reversal (right) perturbation at level of 1%. The plots show that error resulted by dead channels reach -50 dB, while the error resulted by same level of polarity reversal is almost 10 dB higher, i.e. -40 dB.

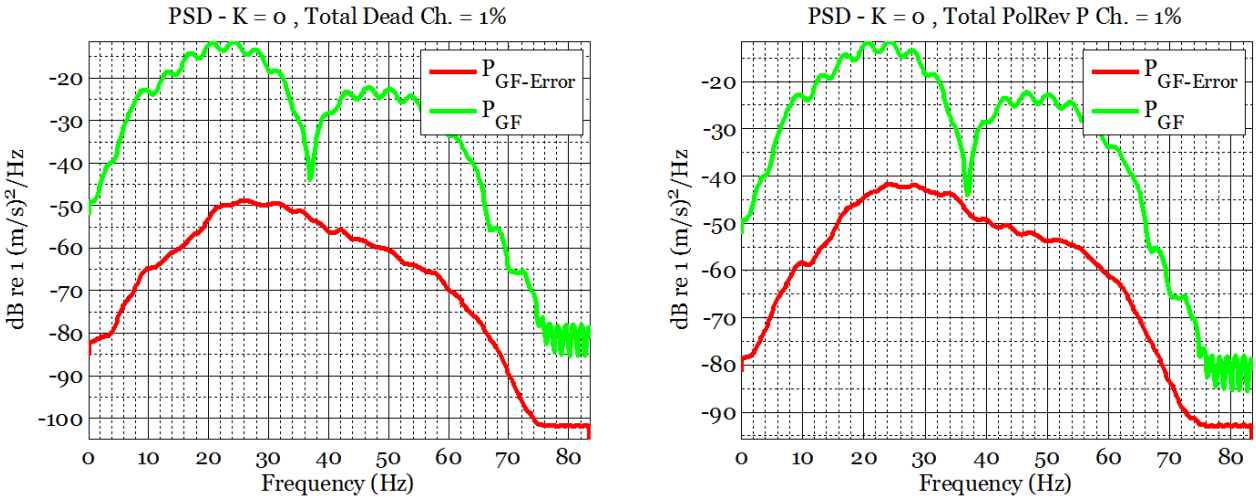

Figure 64: Power spectral density of the pressure wave field and the error due to dead channels (left) and polarity reversal (right). Standard deviation of the error is 1%.

6.4.2 Dead channels, Polarity reversals and their impact on particle velocity data

Here we have individually applied dead channels and polarity reversals perturbation to the particle velocity wave field by killing/reversing the output of random geophone channels along the streamer. We used the same levels of dead/polarity reversed channels for geophones as hydrophones:

$$\text{Dead/Polarity rev. channel levels} = \begin{cases} 0.25\% \\ 0.5\% \\ 1.0\% \end{cases}$$

The same approach of applying perturbation was used for particle velocity data. The data was first interpolated to a denser grid, then dead/polarity reversed channels were chosen randomly from the interpolated data so that they were part of the layout used for group forming. The interpolated perturbed data was then groupformed and down-sampled to the initial grid.

Figure 65 shows the FK plot of the particle velocity wave field error due to dead channels (left plots) and polarity reversal (right plots) perturbation at different levels after group forming. Here also the error increases with perturbation level increment. The error varies at different frequencies. The plots also indicate that error due to polarity reversal has higher impact on the particle velocity wave field than the dead channel perturbation. This is reasonable since polarity reversal results in reversed amplitude (-1) recorded by a channel which obviously has higher impact than dead channels resulting in zero amplitude. Comparing the particle velocity wave field error with the results at previous section, we can conclude that same level of dead channels and polarity reversals perturbation has higher impact on the pressure wave field than the particle velocity wave field.

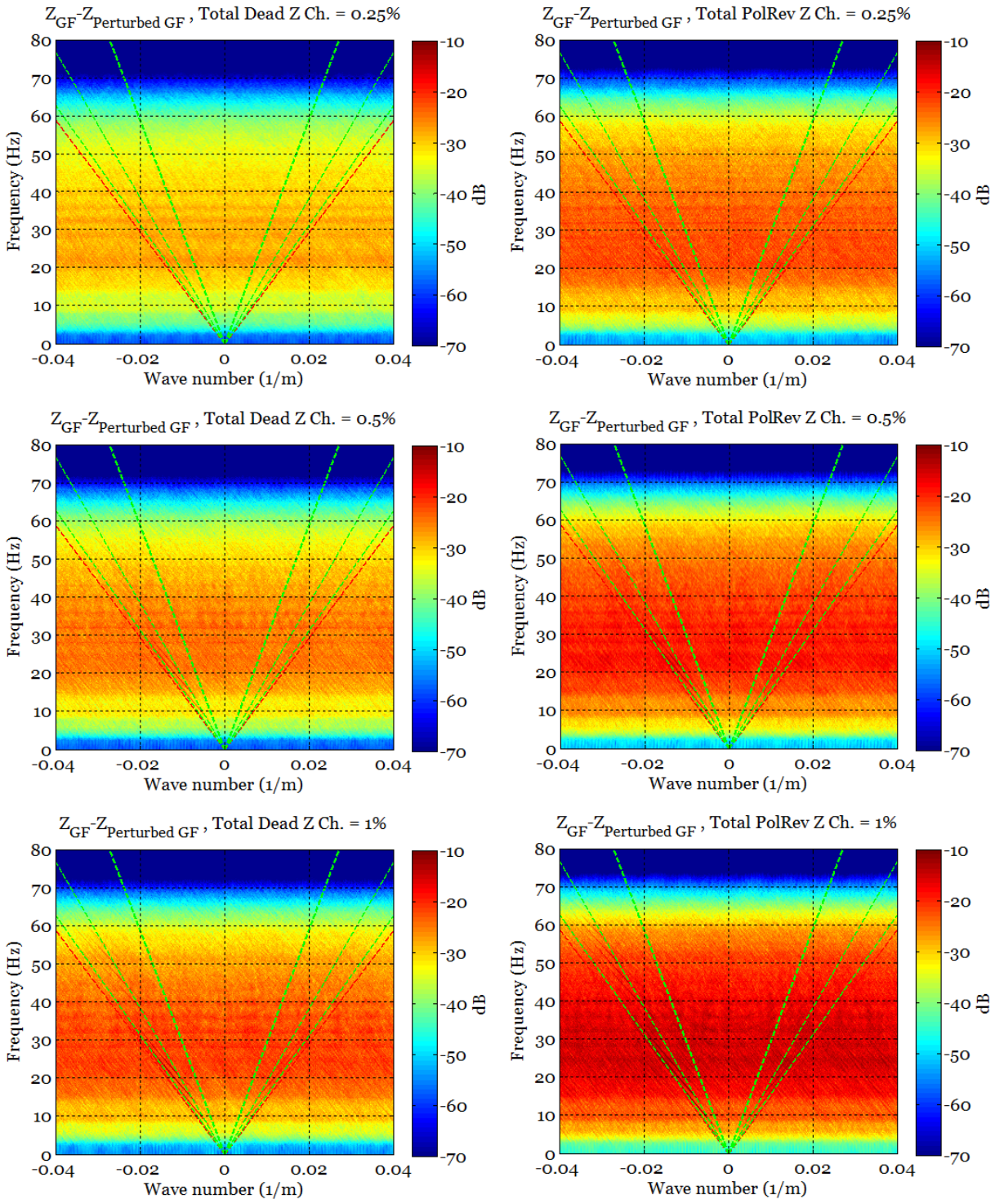

Figure 65: FK plot of the particle velocity wave field error after group forming resulted by applying dead channel (left) and polarity reversal (right) perturbations at different percentage levels.

The FK-slice plots of the error in the particle velocity wave field did not indicate any differentiation of error at different steering angles.

Figure 66 shows the power spectral density of the particle velocity wave field and the error due to dead channels (left) and polarity reversal (right) perturbation at level of 1%. Comparing it with results from perturbing the pressure wave field shown at Figure 64, we can see that error due to the same level of dead channels and polarity reversals perturbation is slightly lower in the particle velocity wave field than the error in pressure wave field.

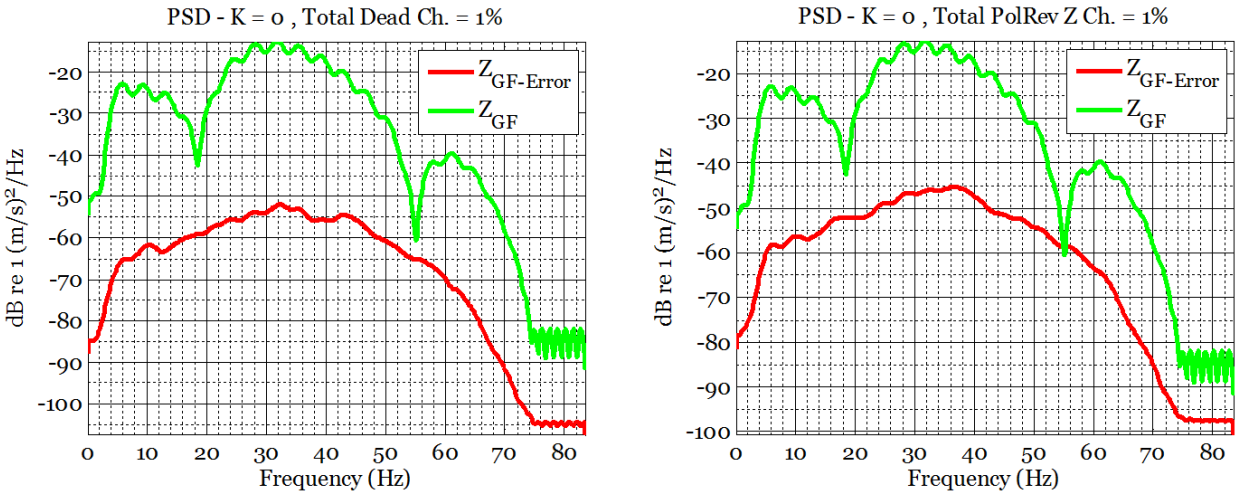

Figure 66: Power spectral density of the particle velocity wave field and the error due to dead channels (left) and polarity reversal (right). Standard deviation of the error is 1%.

6.4.3 Dead channels, Polarity reversals and up-going wave field

In this section we will study the impact of the dead channels and polarity reversal perturbation on the up-going wave field generated using PZSUM algorithm.

Our analysis included the following cases:

A. Perturbed up-going wave field resulted by just perturbing the pressure wave field.
B. Perturbed up-going wave field resulted by just perturbing the particle velocity wave field.
C. Perturbed up-going wave field resulted by both perturbing the pressure and particle velocity wave field.

All the cases mentioned above are performed on the groupformed data.

Figure 67 shows the FK plot of the up-going wave field error due to perturbing pressure wave field by dead channels (Left) and polarity reversal (Right) at perturbation level of 1% (Case A).

Figure 68 shows the FK plot of the up-going wave field error due to perturbing particle velocity wave field by dead channels (Left) and polarity reversal (Right) at perturbation level of 1% (Case B).

Figure 69 shows the FK plot of the up-going wave field error due to perturbing both pressure and particle velocity wave field by dead channels (Left) and polarity reversal (Right) at perturbation levels of 1% (Case C).

Comparing the results shown at Figure 67 and Figure 68, we can conclude that the error in the up-going wave field is dominated by the error in the pressure wave field both for dead channels and polarity reversals perturbations.

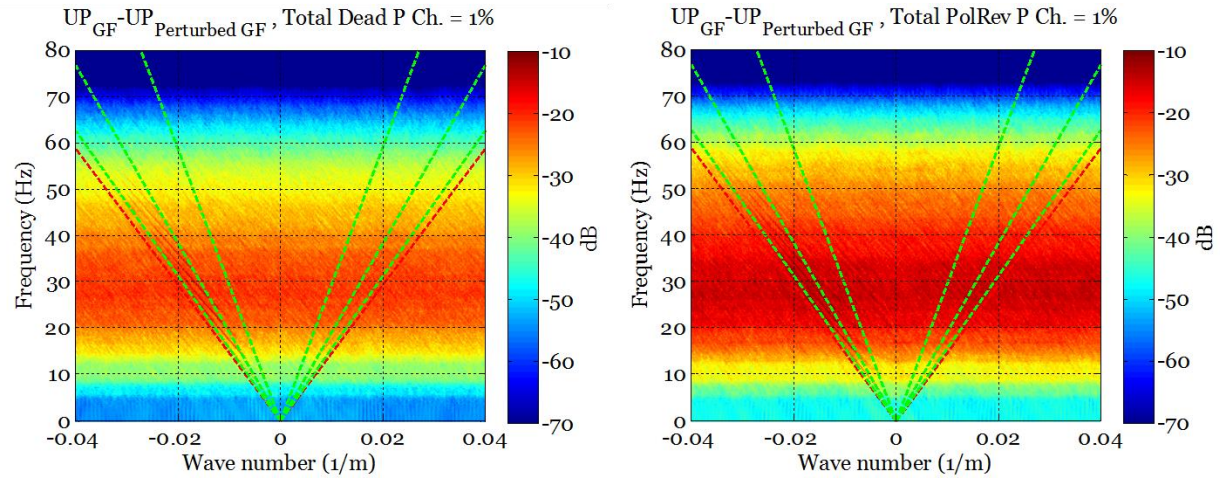

Figure 67: FK plot of the up-going wave field error resulted by applying dead channel (Left) and polarity reversal (Right) perturbation on pressure wave field (Case A). Standard deviation of error is 1%.

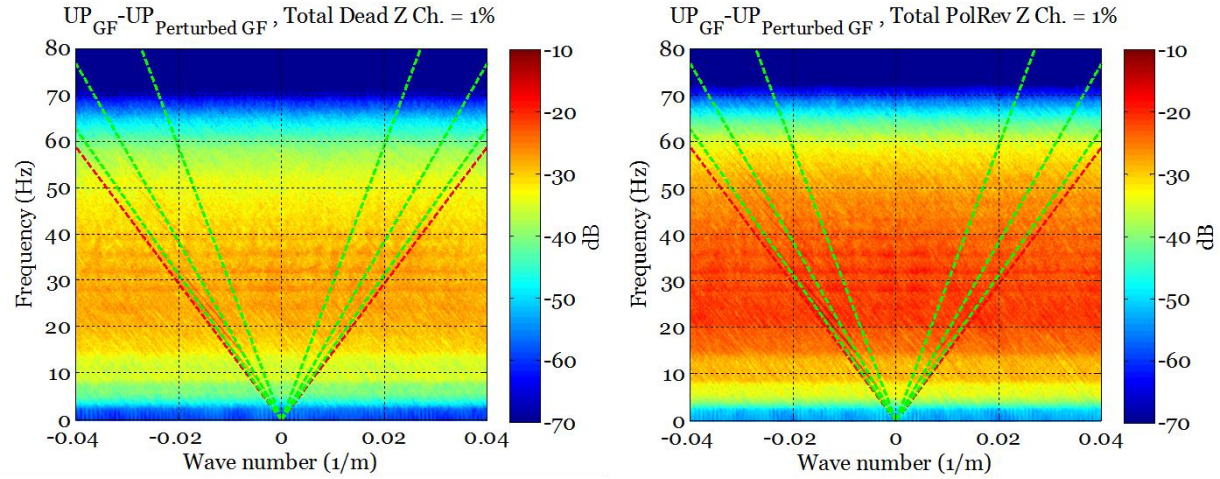

Figure 68: FK plot of the up-going wave field error resulted by applying dead channel (Left) and polarity reversal (Right) perturbation on particle velocity wave field (Case B). Standard deviation of error is 1%.

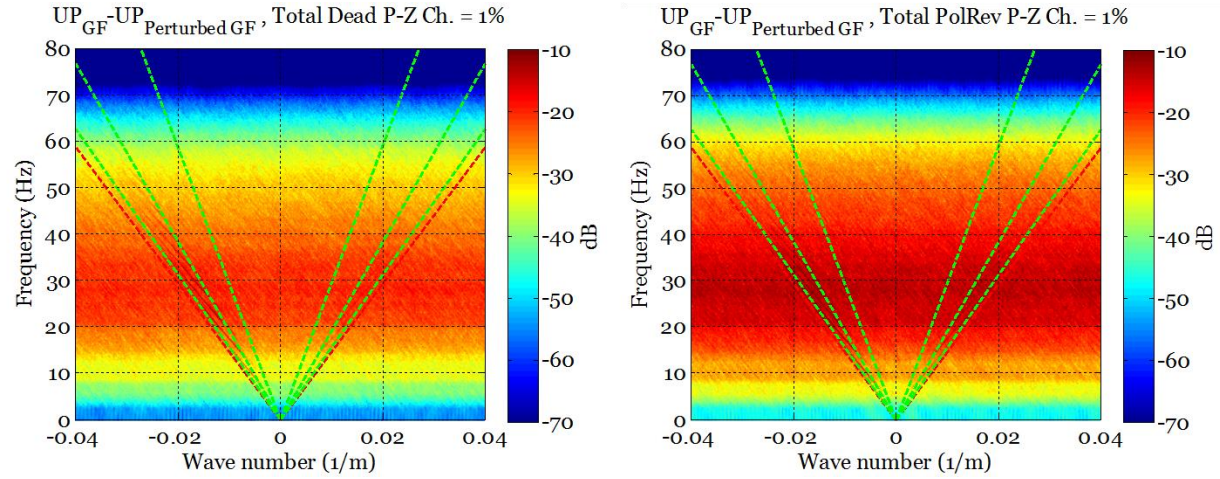

Figure 69: FK plot of the up-going wave field error resulted by applying dead channel (Left) and polarity reversal (Right) perturbation on both pressure and particle velocity wave field (Case c). Standard deviation of error is 1%.

Figures below shows the power spectral density of the up-going wave field and the error due to perturbing the following wave fields by dead channels and polarity reversals individually:

A. Pressure wave field (Figure 70).
B. Particle velocity wave field (Figure 71).
C. Both pressure and particle velocity wave field (Figure 72).

Comparing the result from case A and B shows that the error in the up-going wave field is increased by about 5 dB from just perturbing only pressure wave field to both perturbing pressure and particle velocity wave field which indicates that error in up-going wave field is dominated by the error in the pressure wave field.

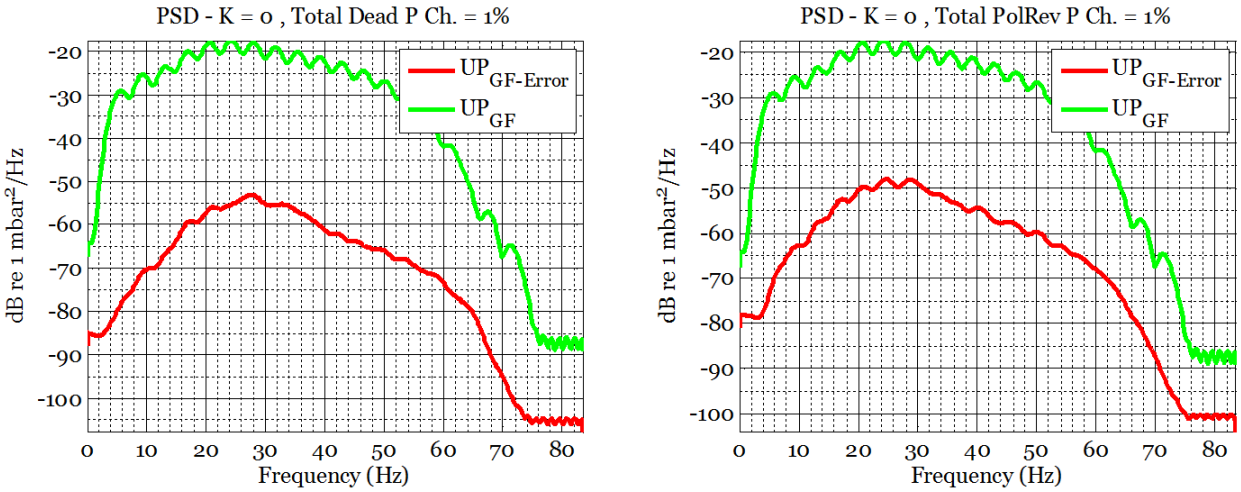

Figure 70 : Power spectral density of the up-going wave field and the error resulted by perturbing the pressure wave field with 1% dead channels (Left) and 1% polarity reversal (Right).

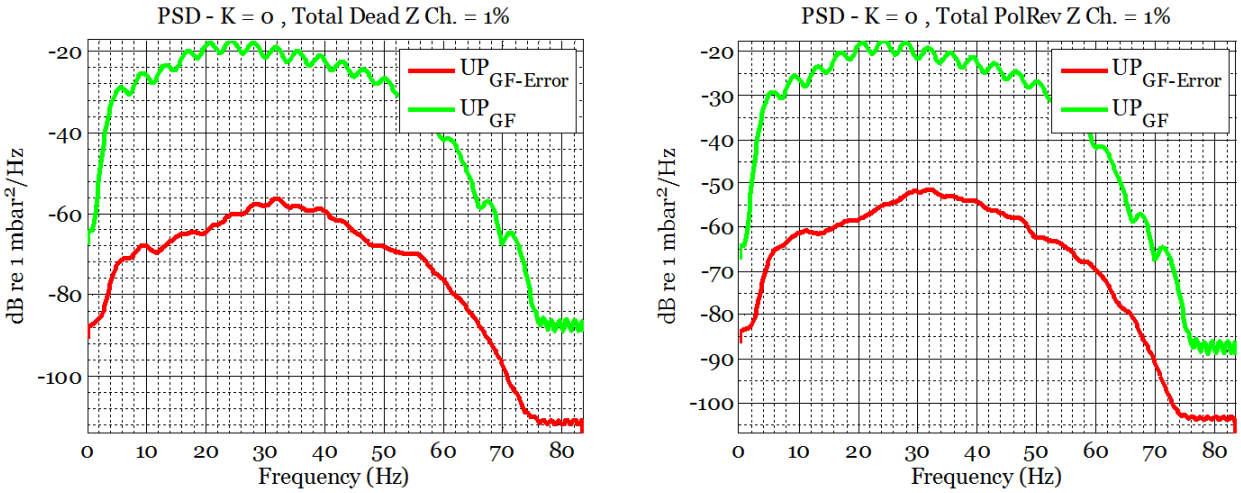

Figure 71: Power spectral density of the up-going wave field and the error resulted by perturbing the particle velocity wave field with 1% dead channels (Left) and 1% polarity reversal (Right).

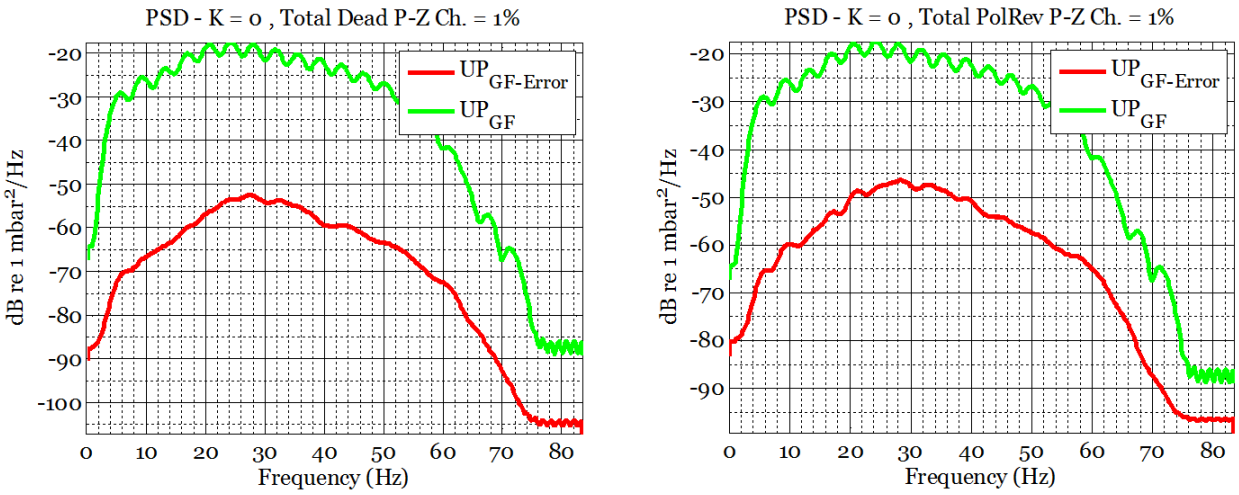

Figure 72: Power spectral density of the up-going wave field and the error resulted by perturbing both pressure and particle velocity wave field with 1% dead channels (Left) and 1% polarity reversal (Right).

Figure 73 and Figure 74 shows the averaged normalized RMS of the up-going wave field error due to dead channels and polarity reversal respectively in a 2D plot. Pressure and particle wave field are perturbed along the vertical and horizontal axis with dead channels and polarity reversals at different levels. We can see from the plot that the error increases by increasing perturbation level along each axis, but the error resulted by perturbation in pressure wave field is slightly higher than the particle velocity wave field error for the same perturbation level. It indicates that the error is dominated by the error in pressure wave field for both dead channels and polarity reversals perturbations.

Comparing the error in up-going wave field resulted by dead channels and polarity reversals perturbation also shows that polarity reversal has higher negative impact on data than dead channels perturbation. The same level of perturbation results with 5 dB higher error on polarity reversals case than dead channels.

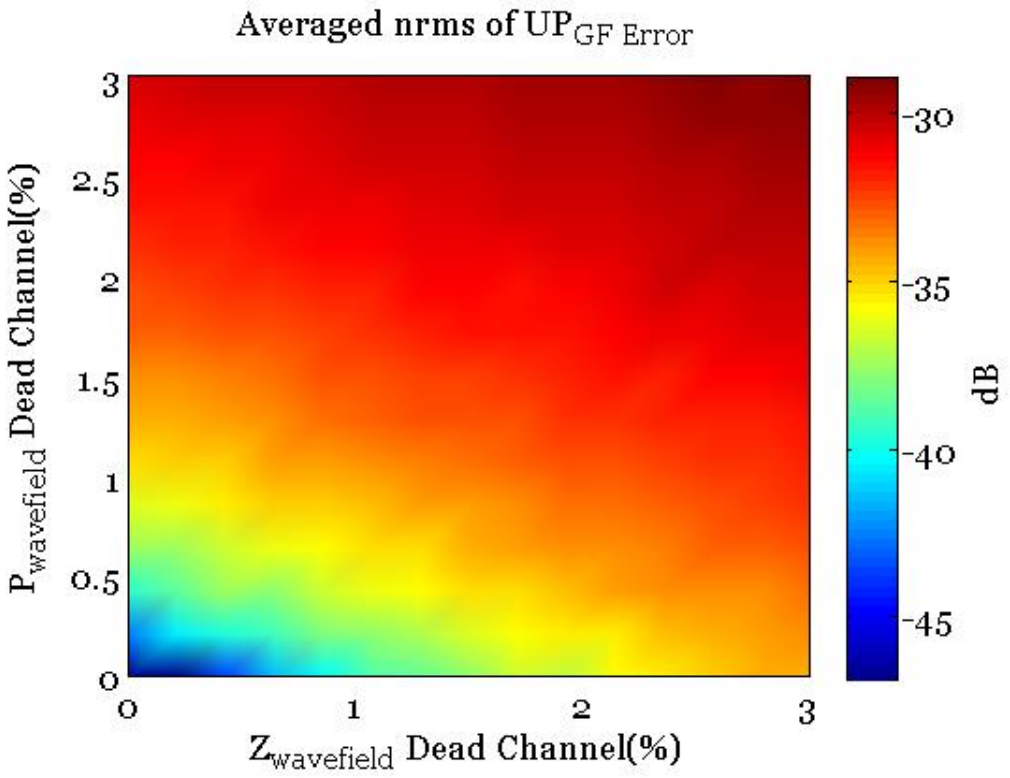

Figure 73: 2D plot of the averaged normalized RMS of the error in the up-going wave field after group forming. The pressure and particle velocity wave fields are perturbed by 0-2% dead channels along vertical and horizontal axis.

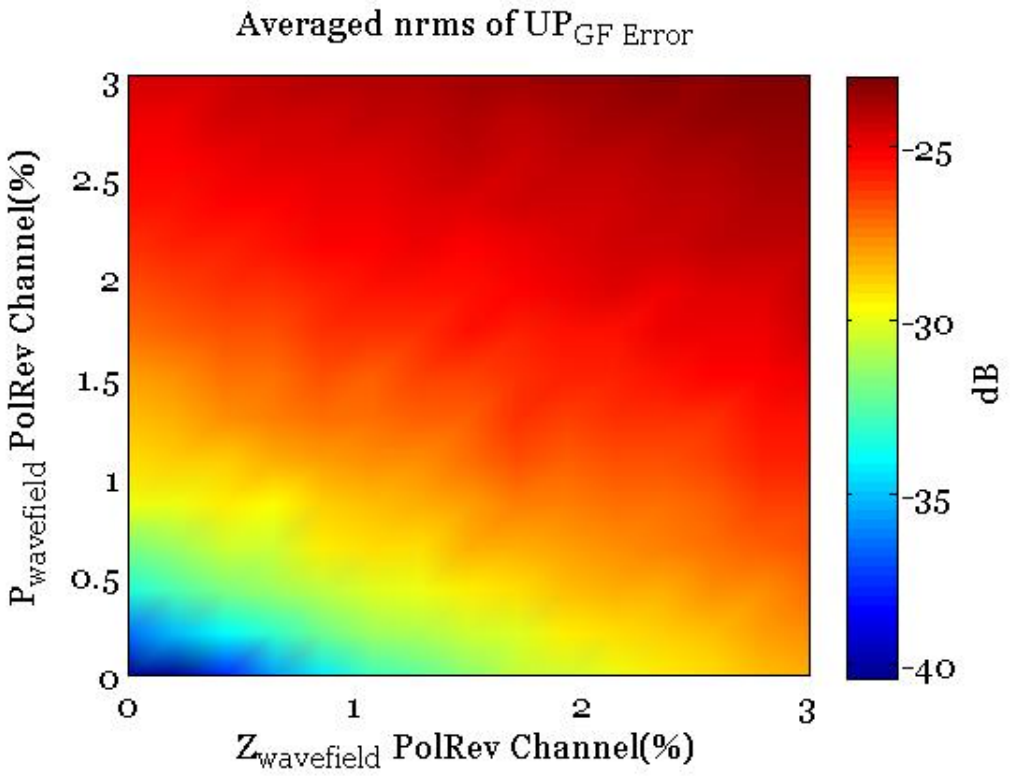

Figure 74: 2D plot of the averaged normalized RMS of the error in the up-going wave field after group forming. The pressure and particle velocity wave fields are perturbed by 0-3% polarity reversals along vertical and horizontal axis.

6.5 Sensitivity perturbation

In this section we will study the effect of the sensitivity perturbation on the synthetic seismic data. Each individual sensor has a sensitivity factor specified in the sensor specification chart, indicating the amount of change in the sensor's output when changing the measured quantity. If the sensors sensitivity is not constant over the output range of the sensor, it is noted as a percentage of the full range defining the amount that sensor's output differs from ideal behavior (Sensor. (2014, February 2), http://en.wikipedia.org/wiki/Sensor).

Both hydrophone and geophone sensors have a sensitivity factor which is different depending on their type and spec. We have decided to apply sensitivity perturbation on both the pressure and particle velocity wave field and quantify its impact on each wave field before and after deghosting (PZSUM). The overall error resulted by sensitivity perturbation is dominated by the signal amplitude error.

We applied sensitivity perturbation by adding normally distributed pseudorandom error with standard deviation varying from 1% to 5% to the synthetic data. All the analysis has been performed on the groupformed data.

6.5.1 Sensitivity error and its impact on the pressure data

Here we will look at the impact of the sensitivity perturbation on the pressure wave field. Additive random error with standard deviation of 1 to 5 percent has been added to the data.

Figure 75 shows the FK plot of the pressure wave field error due to sensitivity perturbation at different sensitivity tolerance levels. The standard deviation of the additive error has been varied from 1 to 5 percent. We can see that the error increases with the sensitivity tolerance level increment. The error appears in an arch (curve) shape. This is due to group forming layout filter which has been applied on the data after perturbing our data. The error is not constant with frequency. It is highest at frequencies between 20-40 Hz.

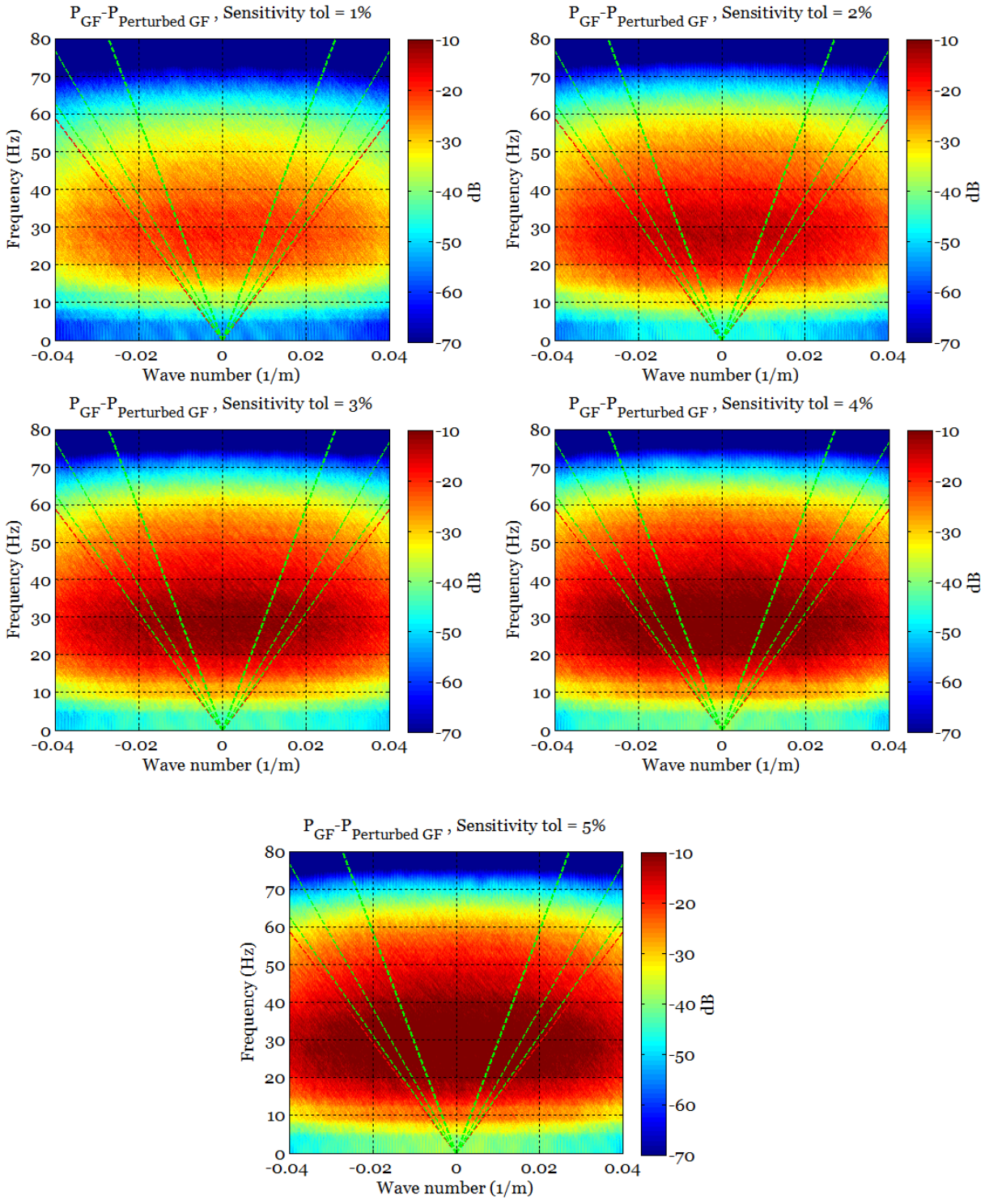

Figure 75: FK plot of the pressure wave field error after group forming resulted by applying sensitivity perturbation at different standard deviation levels.

Figure 76 shows the power spectral density of the pressure wave field and the error resulted by applying sensitivity perturbation with standard deviation of 5%. The error attains maximum of approximately -40 dB at frequencies between 20-30 Hz. We can see that error reach the signal level at about 37 Hz where the receiver ghost occurs.

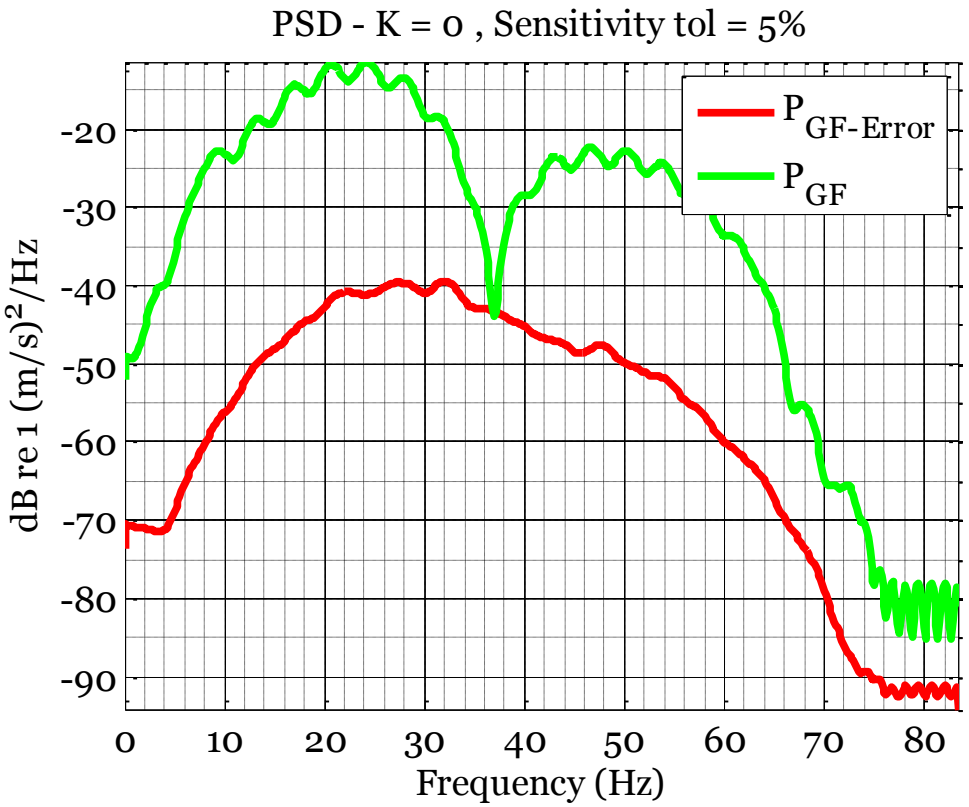

Figure 76: Power spectral density of the pressure wave field and the error resulted by applying sensitivity perturbation with standard deviation of 5%.

6.5.2 Sensitivity error and its impact on the particle velocity data

Here we will look at the impact of the sensitivity perturbation on the particle velocity data. Additive random error with standard deviation of 1 to 5 percent has been added to the data.

Figure 77 shows the FK plot of the particle velocity wave field error due to sensitivity perturbation at different sensitivity tolerance levels. The standard deviation of the additive error has been varied from 1 to 5 percent. The error is not constant with frequency as geophone transfer function's damping factor depends on sensitivity. This has been illustrated at chapter 6.1.1. We can see that the error increases with the sensitivity tolerance level increment. Comparing the particle velocity error due to sensitivity with the results at previous section, we can conclude that same level of sensitivity perturbation has higher impact on the pressure data.

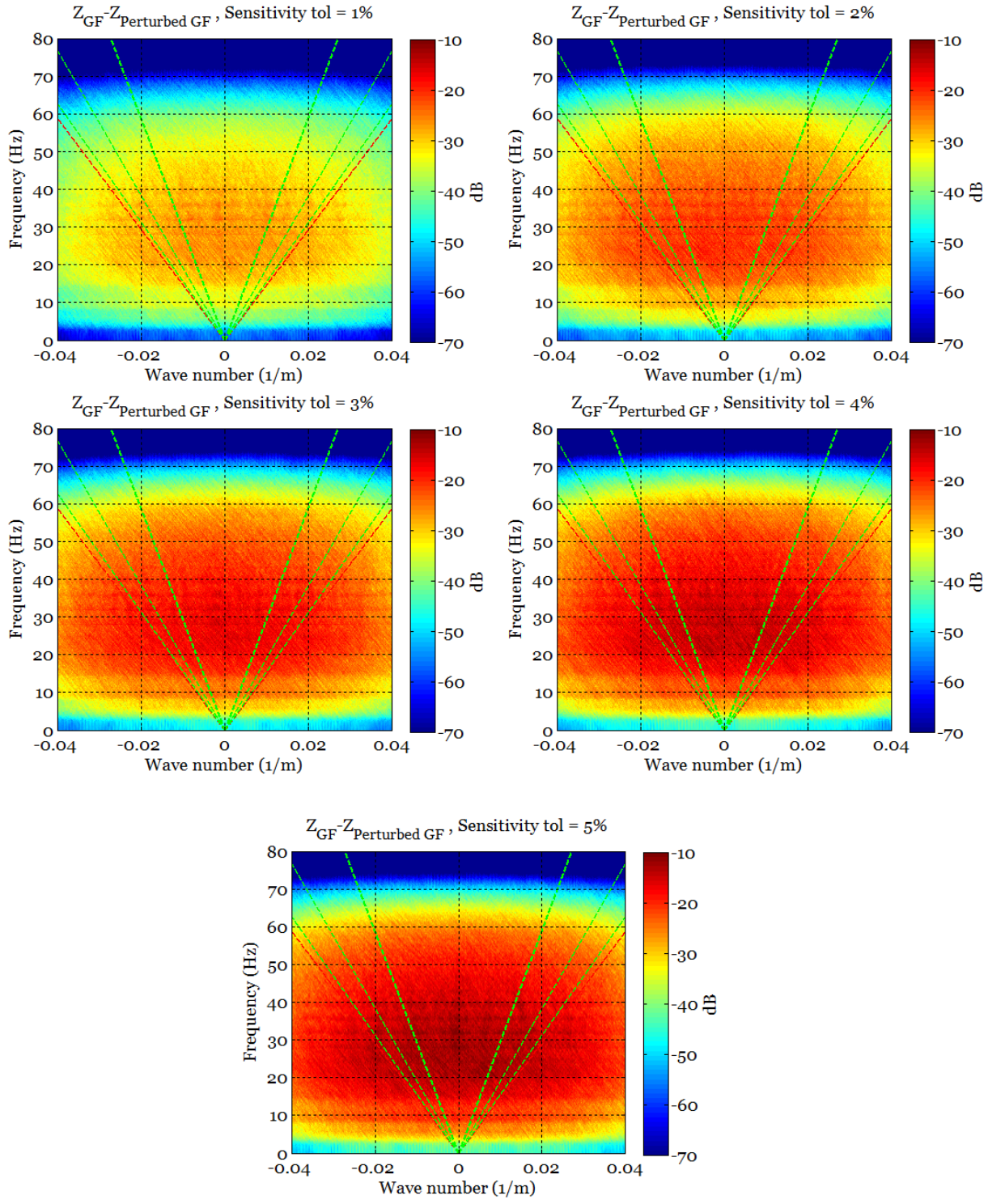

Figure 77: FK plot of the pressure wave field error after group forming resulted by applying sensitivity perturbation at different standard deviation levels.

Figure 78 shows the power spectral density of the particle velocity wave field and the error resulted by applying sensitivity perturbation with standard deviation of 5%. The error attains maximum of approximately -42 dB at frequencies between 30-40 Hz. We can see that error reach the signal level at about 55 Hz where the receiver ghost occurs.

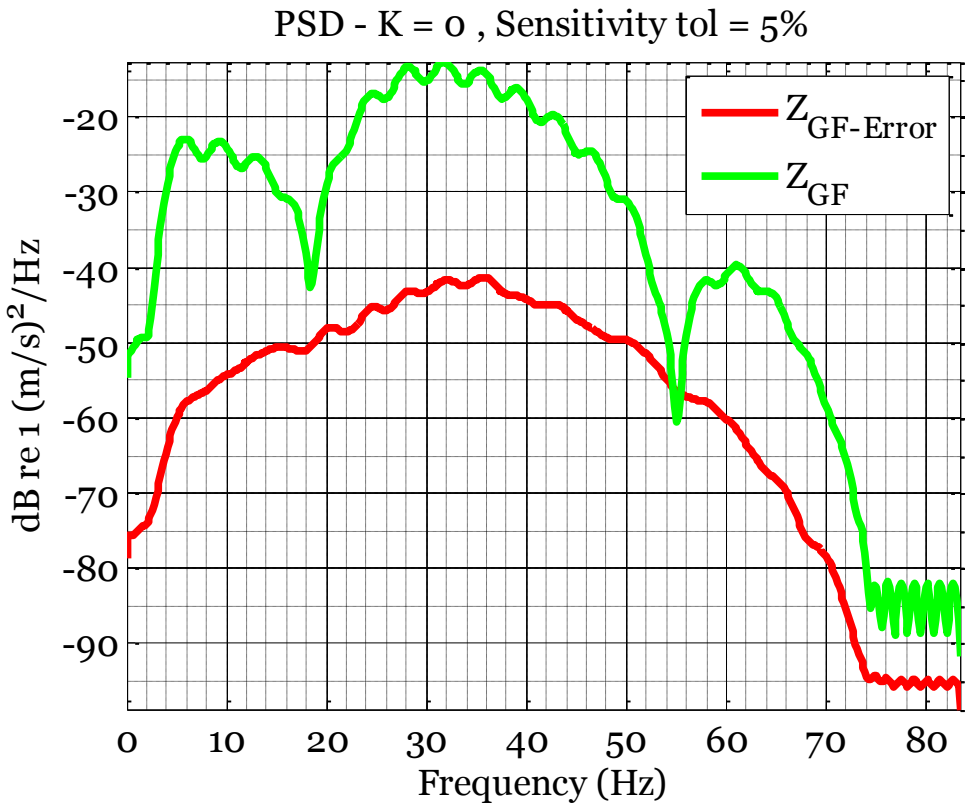

Figure 78: Power spectral density of the particle velocity wave field and the error resulted by applying sensitivity perturbation with standard deviation of 5%.

6.5.3 Sensitivity error and up-going wave field

In this section we will study the impact of sensitivity perturbation on the up-going wave field generated using PZSUM algorithm. Our analysis included the following three cases:

A. Perturbed up-going wave field resulted by just perturbing the pressure wave field.
B. Perturbed up-going wave field resulted by just perturbing the particle velocity wave field.
C. Perturbed up-going wave field resulted by both perturbing the pressure and particle velocity wave field.

All the analysis mentioned above are performed on the groupformed data. Additive random error with standard deviation of 1 to 5 percent has been added to each dataset and the impact of it on up-going wave field has been analyzed.

Figure 79 shows the FK plot of the up-going wave field error due to sensitivity perturbation applied on the pressure wave field (Case A).

Figure 80 shows the FK plot of the up-going wave field error due to sensitivity perturbation applied on the particle velocity wave field (Case B).

Figure 81 shows the FK plot of the up-going wave field error due to sensitivity perturbation applied on both pressure and particle velocity wave field (Case C).

The FK plots are shown for the least and most standard deviation level of error, also 1% and 5%. Comparing the results here, we can conclude that the error in the up-going wave field resulted by sensitivity perturbing our data is dominated by the error in pressure wave field.

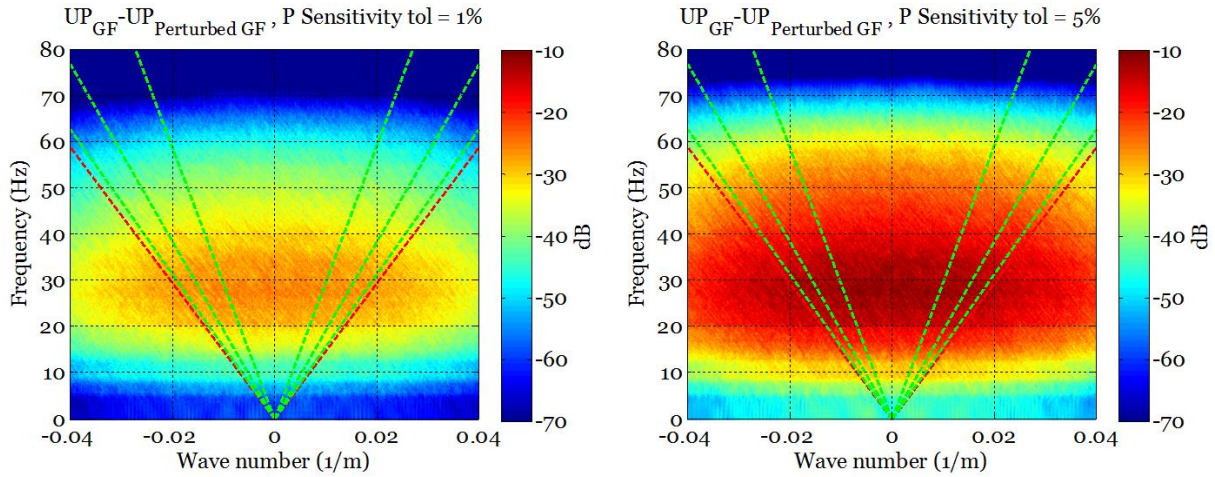

Figure 79: FK plot of the up-going wave field error resulted by applying sensitivity perturbation on pressure wave field at 1% (Left) and 5% (Right) tolerance level (Case A).

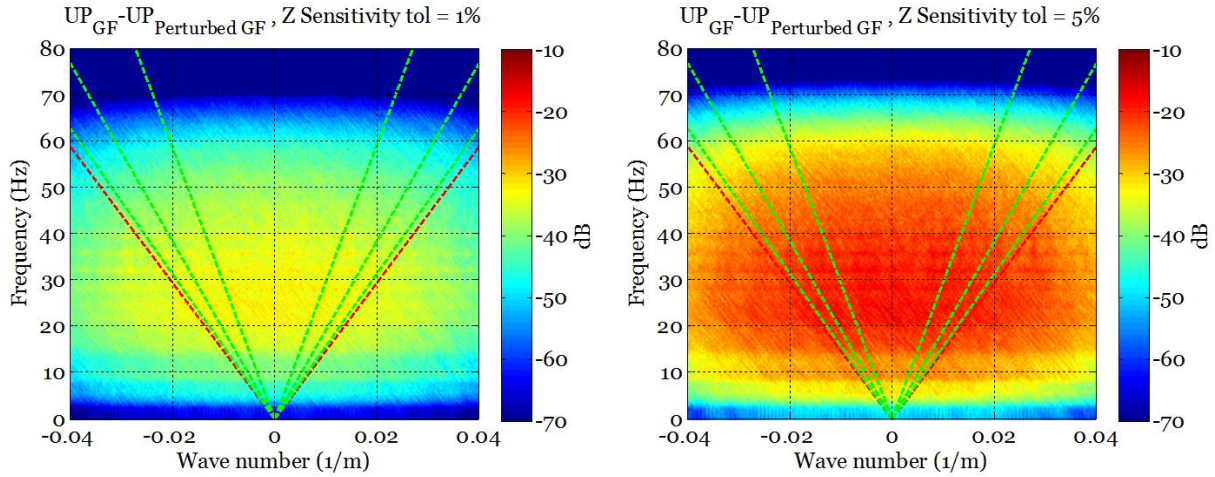

Figure 80: FK plot of the up-going wave field error resulted by applying sensitivity perturbation on particle velocity wave field at 1% (Left) and 5% (Right) tolerance level (Case B).

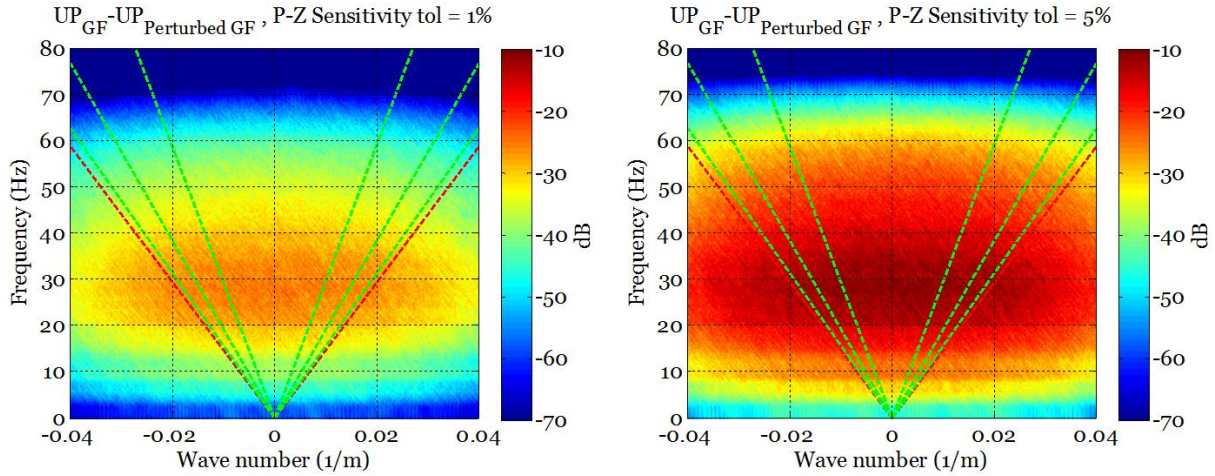

Figure 81: FK plot of the up-going wave field error resulted by applying sensitivity perturbation on both pressure and particle velocity wave field at 1% (Left) and 5% (Right) tolerance level (Case C).

Figure 82 shows the power spectral density of the up-going wave field and the error resulted by applying sensitivity perturbation with standard deviation of 5% on the following wave fields:

A. Pressure wave field (Top left).
B. Particle velocity wave field (Top right).
C. Both pressure and particle velocity wave fields (Bottom left).

We can see from the plots that the up-going wave field error has slightly increased from just perturbing the pressure wave field to perturbing both wave fields which indicates that the error is dominated by the error in the pressure wave field.

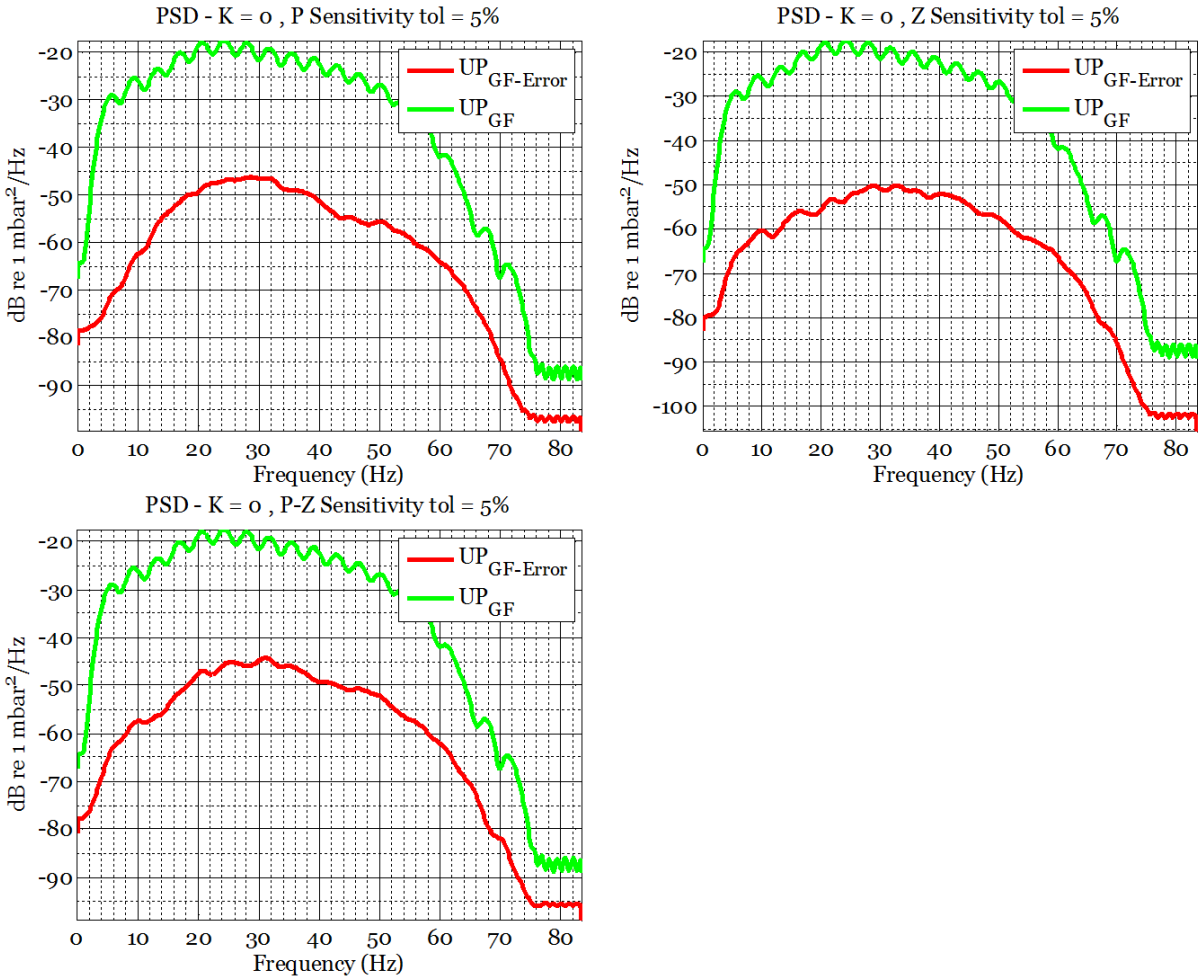

Figure 82: Power spectral density of the up-going wave field and the error resulted by applying sensitivity perturbation on the pressure wave field (top left), particle velocity wave field (top right) and both pressure and particle velocity wave field (bottom left) with sensitivity tolerance of 5%.

Figure 83: shows the averaged normalized RMS of the up-going wave field error due to sensitivity perturbation in a 2D plot. Pressure and particle velocity wave fields are perturbed along the vertical and horizontal axis. Sensitivity tolerance level varies from 0-5% along each axis. We can see from the plot that the error increases slightly faster along the vertical axis which indicates that same level of sensitivity perturbation results in higher level of error on pressure wave field than the particle velocity wave field.

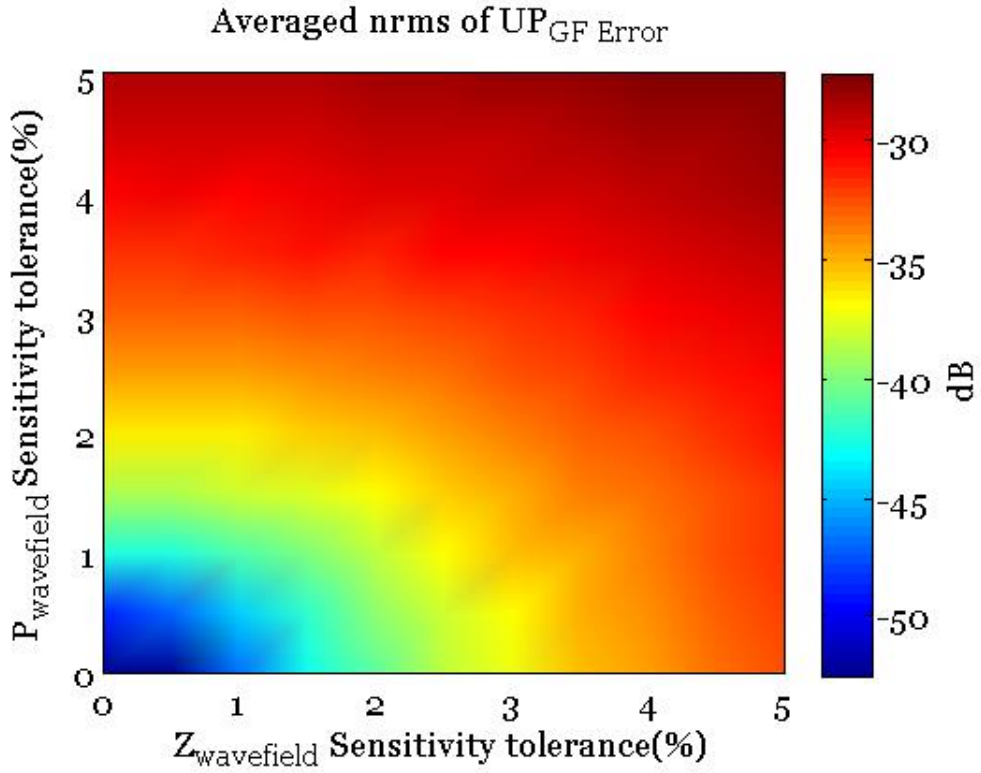

Figure 83: 2D plot of the averaged normalized RMS of the error in the up-going wave field after group forming. Sensitivity perturbation has been applied to the pressure and particle velocity wave fields along vertical and horizontal axis. Sensitivity tolerance level varies from 0-5% along each axis.

6.6 Vector fidelity

Tilt/Inclination and rotation affect the reflection data in a similar way. Unless special cases where a group of hydrophones are combined to focus and gather energy propagating at specific direction, they are not sensitive to small tilt or rotation since they are almost omnidirectional and have huge opening angle sampling the field. Hence we will study the effect of tilt or rotation on the particle velocity data which is recorded by geophones. Geophones are very sensitive to tilt or rotation.

Tilt/rotation changes the signal being recorded by the geophone in two ways:

1. It scales the vertical component being recorded with geophone by a factor $\cos(\theta)$. When there is no tilt $(\theta = 0)$, the recorded signal equals the original.
2. It results in leakage from the radial component by a factor $\sin(\theta)$.

Since we only have the vertical component of geophone data (V_z), we will only focus on the first effect of tilt/rotation in this thesis; also amplitude perturbation resulted by a factor $\cos(\theta)$. Signals recorded by tilted geophones experience an amplitude perturbation which is always smaller or equal 1.

In our case we have perturbed particle velocity data by tilting the geophone sensors along the streamer with random tilt angle. The standard deviation of angle θ is varied from 0° to 10°. We use normalized RMS, power spectral density, and frequency-wavenumber analysis to quantify the error.

Figure 84 shows the FK plot of the particle velocity wave field error due to tilting geophone sensors at different angles with standard deviation varying from 2° to 10°.

The error is not constant with frequency. It increases with tilt angle increment and is highest at multiples.

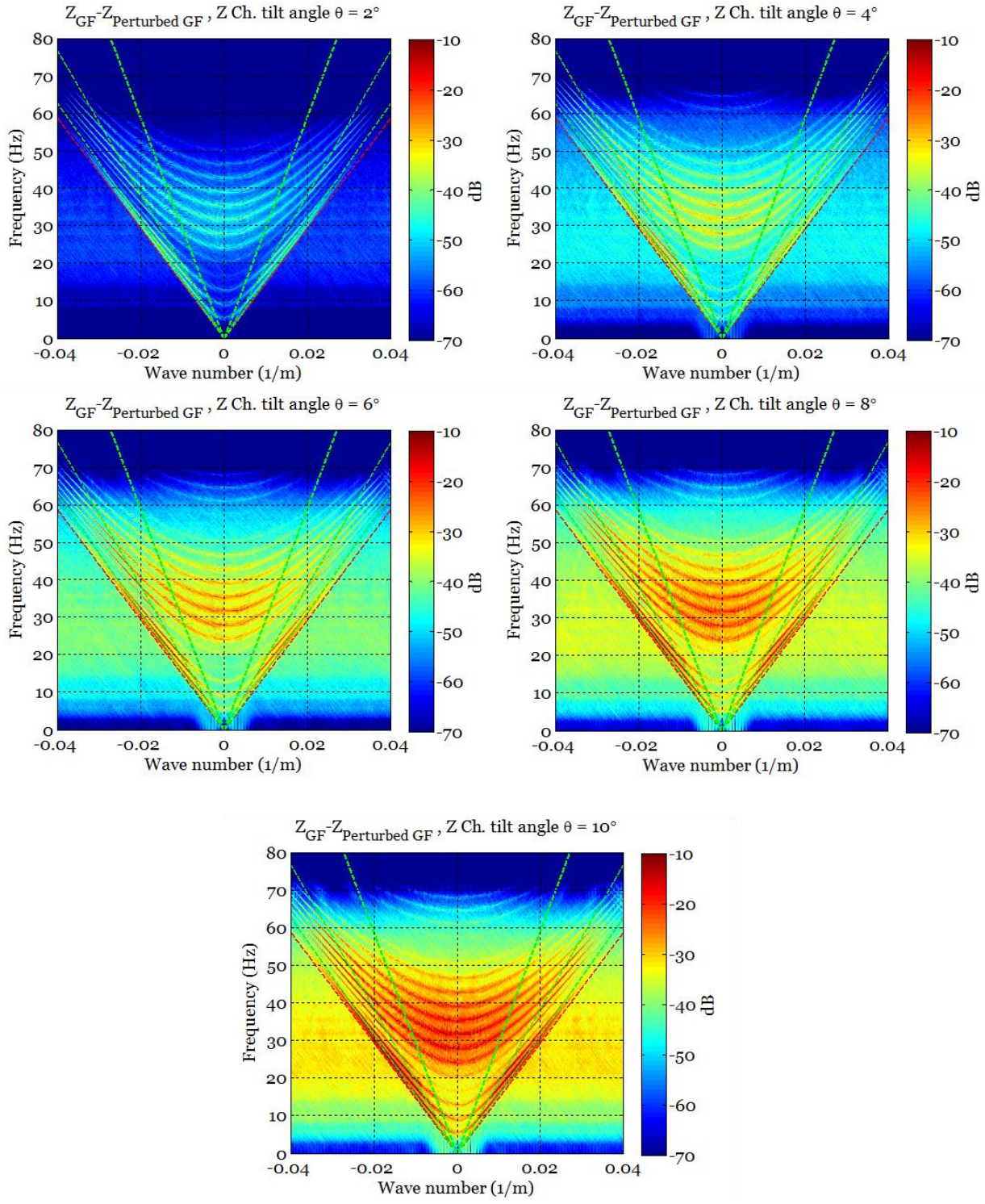

Figure 84: FK plot of the particle velocity wave field error after group forming resulted by tilting geophone sensors at different angles.

Figure 85 shows the power spectral density of the particle velocity wave field and the error due to tilting geophone sensors with random angles and standard deviation of 10°.

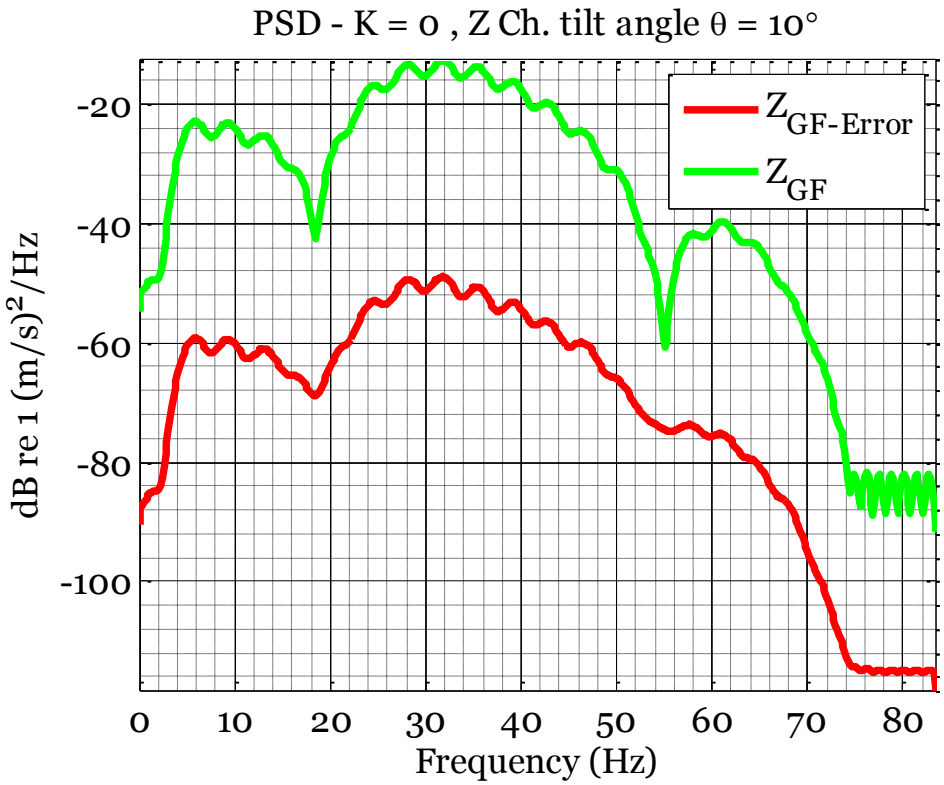

Figure 85: Power spectral density of the particle velocity wave field and the error resulted by tilting geophone sensors with an angle of 10°.

We have taken one step further and studied the effect of tilting on the up-going wave field. We have first perturbed particle velocity data by tilting the geophone sensors along the streamer with random tilt angle and standard deviation of angle θ varying from 2° to 10°, later perfomed deghosting on the perturbed data. Figure 86 shows the FK plot of the up-going wave field error resulted by tilting geophone sensors at different angles. The error increases with tilt angle increment. Comparing these plots with the FK plots before performing deghosting (Figure 84), we observe that error level decrease about 10 dB after deghosting.

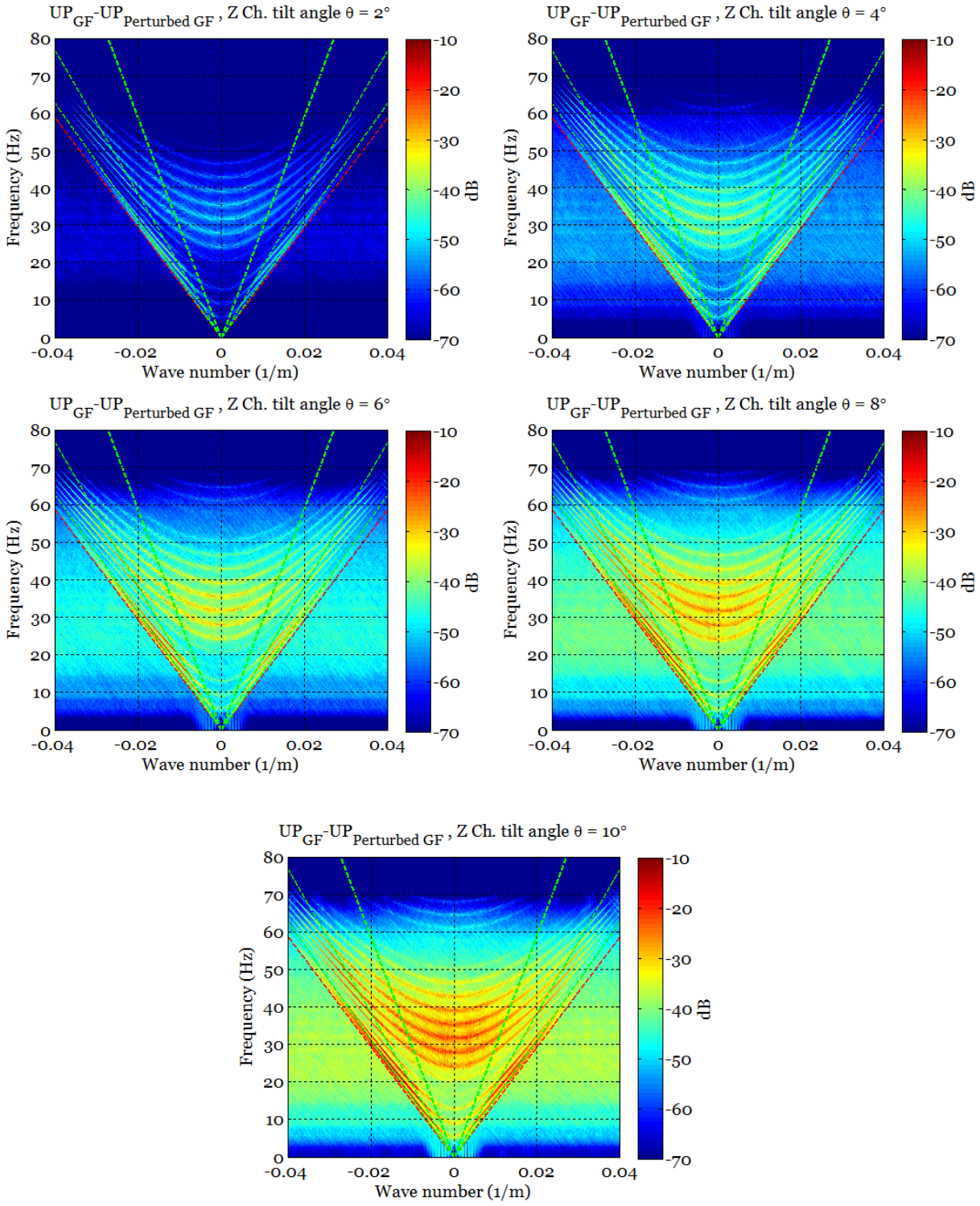

Figure 86: FK plot of the up-going wave field error resulted by tilting geophone sensors at different angles.

Figure 87 shows the averaged normalized RMS of the up-going wave field error due to due to tilting geophone angles at different angles along the horizontal axis. The standard deviation of angle θ varies from 0° to 10° along the horizontal axis. There hasn't been performed any tilt on the hydrophone sensors. As mentioned earlier in this section, hydrophone sensors are not sensitive to tilt/rotation. It is shown in the figure below that tilt on pressure data recorded by hydrophone sensors does not affect the error (vertical axis) which is only for visual purpose. We can see that error increases with tilt angle increment. The error reach -41dB at 10° tilt angle.

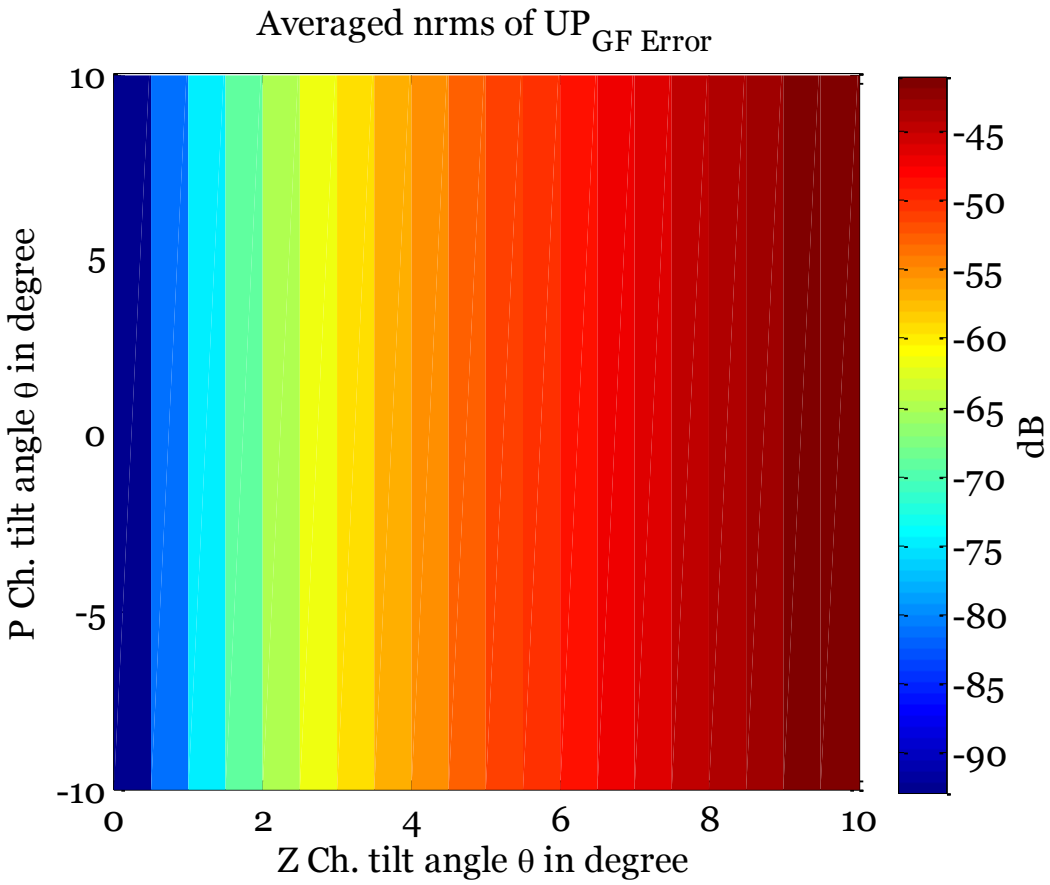

Figure 87: 2D plot of the averaged normalized RMS of the error in the up-going wave field after group forming. Geophone sensors have been tilted at random angles with standard deviation of angle θ varying from 0° to 10° along horizontal axis.

7 Discussion and Conclusion

In this thesis we have introduced some of the perturbations and noise associated with a marine seismic acquisition system and receivers (geophones and hydrophones). We analyzed and quantified the impact of the perturbations on a synthetic seismic dataset generated by simulation of acquisition with a two-component streamer. We have performed a typical acquisition processing flow on the synthetic data that included analog group forming, deghosting using PZSUM algorithm, and then analyzed the impact of these perturbations on the acquired perturbed data.

The oil and gas exploration industry is highly competitive and hence the leading companies in this field keep details of their developed technologies confidential. To our best ability, we have chosen to analyze some of the perturbation which we mean are important or easy to fix. However, without access to this information it is not possible to determine which of the individual perturbations covered in this report is the most important concern in marine seismic acquisition system.

The following perturbations are covered in this thesis:

- **Geophone transfer function**

  In Chapter 6.1 we have looked at the perturbations associated with the geophone transfer function. We used the SM-24 geophone element parameter values as the nominal values. Natural frequency and damping factor tolerance levels have been varied by 0 to $+2.5\%$ and by 0 to $+5\%$ respectively. Our simulation indicates that natural frequency tolerance has higher impact on the particle velocity wave field than damping factor. The averaged normalized RMS of error in the groupformed up-going wave field reaches -40.8 dB for $+2.5\%$ tolerance in natural frequency, while $+5\%$ tolerance in damping factor gives an error of -44.8 dB. The total error in the groupformed up-going wave field resulting from both $+2.5\%$ tolerance in natural frequency and $+5\%$ tolerance in damping factor reaches -39.6 dB.

  Muyzert and Vermeer (2004) described that typical geophone specifications lead to -50 dB error on land seismic data, and concluded that for geophone natural frequency and sensitivity, tolerances are adequate. Accordingly, we can conclude that if typical geophone specifications lead to -50 dB error on the particle velocity wave field, the impact of error will be less than -50 dB on the acquired up-going wave field after deghosting and hence the geophone specifications/tolerances should be adequate in marine seismic acquisition.

- **Self-noise: Brownian motion and Thermal noise**

  In Chapter 6.2 we have studied the impact of geophone self-noise, i.e. Brownian motion and thermal noise error on the synthetic seismic data. We have applied self-noise to the synthetic data after geophone output. The averaged normalized RMS of the error in the groupformed up-going wave field resulted by geophone self-noise reaches -149 dB. The error due to geophone self-noise is much lower in strength compared to the error resulted by the other perturbations discussed in this thesis and will be masked in case of their presence. Hence we conclude geophone self-noise is not a concern and adequate.

- **Sensor position error**

In Chapter 6.3 we have analyzed the impact of hydrophone and geophone position error on the groupformed pressure, particle velocity and up-going wave field. The sensor positions were perturbed with an RMS of $1cm$ to $20\,cm$. In two-component streamer, the hydrophone and geophone sensors are co-located at the same position along the streamer. Hence, the same position error level applied to both receivers. Assuming an RMS of $20\,cm$, the averaged normalized RMS of the error in the groupformed up-going wave field reaches -45 dB. We believe that there should put more effort when mounting the sensors along the streamer in order to minimize the position error. Position error is caused due to assembly technician's inaccuracy. Hence it should be very cost-effective to train the assembly technicians to perform mounting task more accurate if the impact of position error on the acquired data is a concern.

- **Dead channels and Polarity reversals**

Dead channels and polarity reversals were studied in Chapter 6.4. The errors introduced by them are very large compared to the other perturbations. The simulations indicated that these two perturbations have higher impact on the pressure wave field. In addition, polarity reversals result in higher error than dead channels. This is reasonable since polarity reversal results in reversed amplitude (-1) recorded by a channel which obviously has higher impact than dead channels resulting in zero amplitude. The total averaged normalized RMS of error in groupformed up-going wave field reaches -28.9 dB by 3% dead channels, while 3% polarity reversals give -23 dB.

We recommended single sensor acquisition (digital group forming) instead of analog group forming to reduce impact of these two perturbations. Polarity reversals can then easily be fixed once they become detected. Dead channels error can also be reduced by interpolating data at dead channel positions. However single sensor streamers could be significantly more expensive than analog groupformed streamers and hence it may be argued that if fit-for-purpose data are acquired with the current standard.

Another possible solution is to perform sanity check before every single acquisition in order to detect and change the sensors with poor response.

- **Sensor sensitivity**

We have looked at the impact of sensor sensitivity perturbation in Chapter 6.5. The total averaged normalized RMS of error in groupformed up-going wave field reaches -27.25 dB by 5% tolerance in geophone and hydrophone sensitivity. The sensor sensitivity error can be truncated with calibration before acquisition. However, there could be put more effort into reducing variation in production of the sensors to reduce the sensitivity variation. This would mean increased cost and should be argued whether the current sensors are adequately specified or not.

- **Vector fidelity**

  Geophone tilt has been analyzed in Chapter 6.6. Our simulations show that 10° tilt results in -40.8 dB error in the groupformed up-going wave field. (Muyzert and Vermeer, 2004) says that tilt measurement and recording of multicomponent particle velocity data can give complete correction. There are also developed depth controllers known as birds mounted on the streamers which enhance sensor stability.

Figure 88 on the next page shows the two-component streamer sensitivity chart with all the perturbations analyzed in this thesis. This chart is obtained by the application of individual perturbations on the synthetic seismic data. It demonstrates the relative significance of error resulting from these perturbations. With respect to the maximum perturbation level that we have simulated for each perturbation, our simulations indicate that the most significant errors are due to polarity reversals and sensor sensitivity. We found that 3% polarity reversals in both pressure and particle velocity wave fields result in -23 dB error in the groupformed up-going wave field.

Two-component streamer sensitivity chart

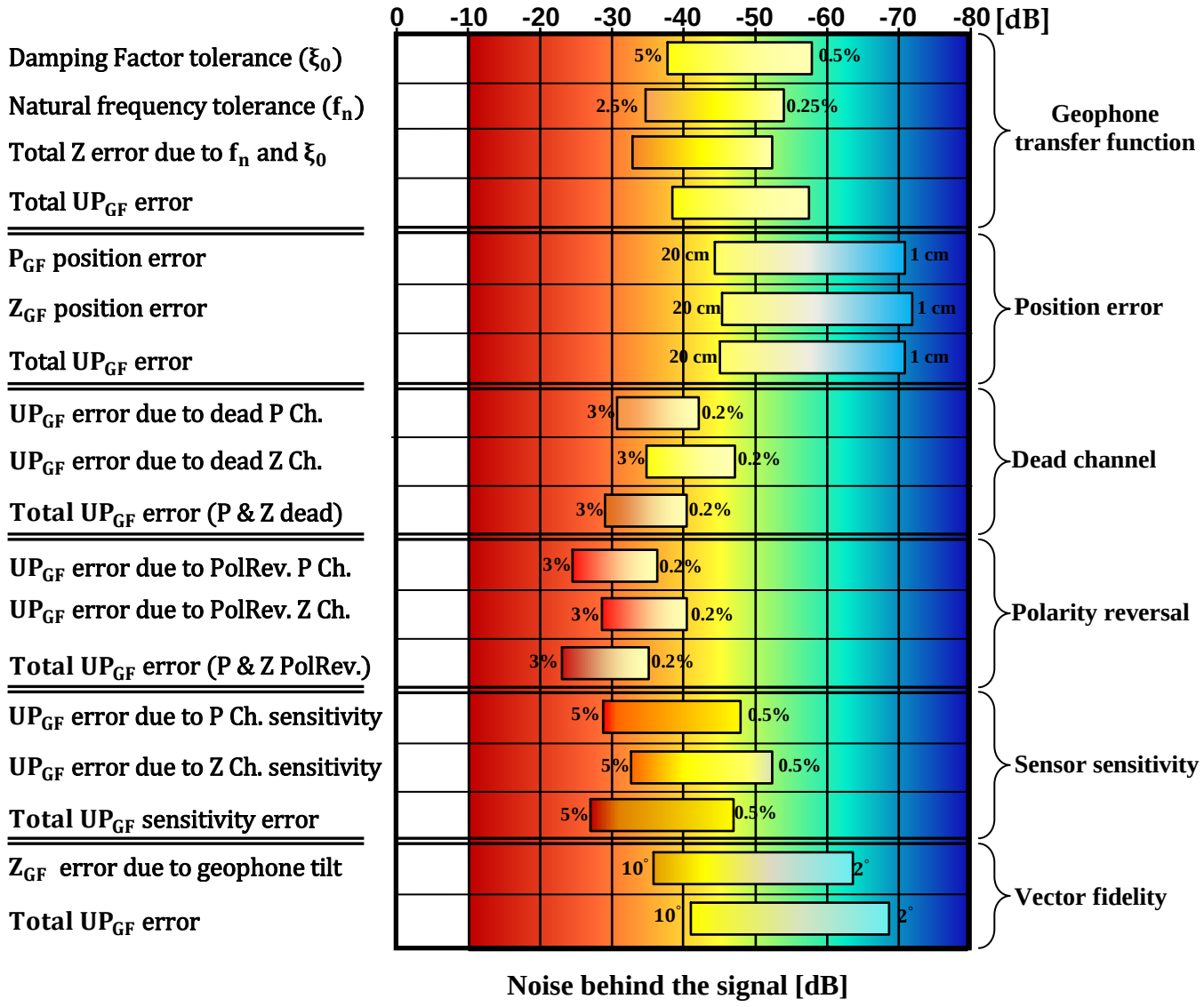

Figure 88: Two-component streamer sensitivity chart.

7.1 Future work

There are several other perturbations and noise associated with marine seismic acquisition system that should be studied. Some of them are listed below:

- **Hydrophone transfer function and self-noise**
- **Geophone distortion due to imperfect moving coil**
- **Ambient noise**
- **Receiver motion error**
- **Synchronization error**
- **Residual receiver statics**

Sensitivity analysis of the two-component streamer using other deghosting methods should also be performed to determine if the system is more or less sensitive to the perturbations studied in this thesis and may also be sensitive to other applicable perturbations. The sensitivity study could also be expanded to consider multicomponent particle motion sensors with inline, crossline, and vertical components.

Appendix

All the sensitivity analysis and simulations in this thesis have been implemented in Matlab software. There has been written nearly 20,000 lines code to simulate a typical acquisition processing flow that included analog group forming, deghosting using PZSUM algorithm, applying modeled perturbations to the synthetic data and then analyzing the impact of these perturbations on the acquired data. Most part of the code is developed while I had been sitting at WesternGeco. The code can be made available by joint agreement with WesternGeco and me.

Bibliography

[1]. Özdemir, A.K. and Caprioli, P., WesternGeco, Oslo, Norway. Özbek, A. and Kragh, ED., Schlumberger, Cambridge, U.K., and Robertsson, Johan O. A., WesternGeco, Gatwick, U.K. (2008). *Optimized Deghosting of Over / Under Towed-Streamer Data*. The Leading Edge (TLE).

[2]. Baldock S., T. G. S., US, Masoomzadeh, H. and Woodburn, N., and Hardwick, A. and Travis, T., T. G. S., UK (2013). *Increasing The Bandwidth of Marine Seismic Data*. PESA News Resources, May, 55–57.

[3]. Ikelle, L., and Amundsen, L. (2005). *Introduction to Petroleum Seismology, Volume 12*. SEG Books, 2005.

[4]. Kragh, J. E., and Muyzert, E. J. (2010). *Marine Seismic Acquisition Methods and System*. US, 2010/0074049 A1.

[5]. Mahoney, J. . T., and Newman, P. (1973*). Patterns - with a Pinch of Salt*. Geophysical Prospecting 21, 197–219.

[6]. IAGC. March, (2002). *Marine Seismic Operations, An Overview Produced by IAGC to provide a reference to other marine operations in general and the fishing industry*.

[7]. Martin, J., Özbek, A., Combee, L., Lunde, N., Bittleston, S., and Kragh, E. (2000). *Acquisition of Marine Point Receiver Seismic Data with a Towed Streamer*. SEG, Expanded Abstract.

[8]. Ozdemir, A. K., Kragh, E., Kjellesvig, B. A., Caprioli, P., Christie, P. A., and Drayton, F. (2011). *Deghosting Seismic Data*. US, 2011/0292762 A1.

[9]. POSTHUMUS, B. J. (1993). *Deghosting Using A Twin Streamer Configuration*. Geophysical Prospecting 41, 267–286.

[10]. Sheriff, R. E., and Geldart, L. P. (1995). *Exploration Seismology*. Cambridge University Press.

[12]. I/O Sensor, Nederland. (2006). *SM-24 Geophone Element*.

[13]. Guilin, L., Gao, C., and Junyi, Z. (2009). *Analysis of Geophone Properties Effects for Land Seismic Data*. Applied Geophysics, 6(1), 93–101. doi:10.1007/s11770-009-0003-4

[14]. Geophysical, ION. (2006). *MSX ^{TM} Solid Active Streamer Section.*

[15]. Hons, M. S., and Stewart, R. R. (2006). *Transfer Functions of Geophones and Accelerometers and Their Effects on Frequency Content and Wavelets*. CREWES Research Report, 18(1).

[16]. Stienstra, A., and Badger, A. S., and Maxwell, P. W., HGS Sensor Netherland and HGS Houston (1993). *Intrinsic Noise in Geophones*, (Vol. 2, pp. 2–3). Stavanger, Norway: EAEG, 55th Meeting and Technical Exhibition.

[17]. Muyzert, E., and Vermeer, P. (2004). *The Impact of Acquisition Perturbations on Land Seismic Data*. SEG Int ' l Exposition and 74th Annual Meeting, Denver, Colorado, 10-15 October 2004.

[18]. Ambardar, A. (2007). *Digital Signal Processing: A Modern Introduction*. Nelson/Thomson.

[19]. Hayes, M. H. (1996). *Statistical digital signal processing and modeling*. John Wiley & Sons.

[20]. Barry, J. R. and Lee, E. A., and Messerschmitt, D. G. (2004). *Digital Communications* (p. 69). Springer.

[21]. Kay, S. M. (1993). *Fundamentals of Statistical Signal Processing: Estimation Theory*. Prentice Hall International Editions.

[22]. Johnson, D.H. and Dudgeon, D. E. (1993). *Array Signal Processing: Concepts and Techniques*. Prentice Hall.

[23]. Ulrick, R. J. (1983). *Principles of Underwater Sound*. Mcgraw-Hill Book Company.

[24]. Robinson, E.A., and Durrani, T.S., and Peardon, L.G. (1986). *Geophysical Signal Processing.* Prentice/ Hall International.

[25]. Gelius, L. J. and Johansen, T. A. (2012). *Petroleum Geophysics VOL II*. UNIGEO.

[26]. Press, W. H., and Flannery, B. P., and Teukolsky, S. A., and Vetterling, W. T. (1992). *Numerical Recipes in C: The Art of Scientific Computing* (Second Edition). Cambridge University Press.

[27]. Wikipedia, The Free Encyclopedia, (2014, February 10). *Brownian motion*. From http://en.wikipedia.org/wiki/Brownian_motion.

[28]. Wikipedia, The Free Encyclopedia, (2014, February 2). *Sensor*. From http://en.wikipedia.org/wiki/Sensor.